1-1-1999

Millimeter-wave molecular mapping of comets Hyakutake and Hale-Bopp.

Amy J. Lovell
University of Massachusetts Amherst

Millimeter-wave Molecular Mapping of Comets Hyakutake and Hale-Bopp

A Dissertation Presented

by

Amy J. Lovell

Submitted to the Graduate School of the
University of Massachusetts Amherst in partial fulfillment
of the requirements for the degree of

Doctor of Philosophy

February 1999

Department of Physics and Astronomy

Millimeter-wave Molecular Mapping of Comets Hyakutake and Hale-Bopp

A Dissertation Presented

by

Amy J. Lovell

Approved as to style and content by:

F. Peter Schloerb, Chair

William M. Irvine, Member

Michael F. Skrutskie, Member

William A. Dent, Member

George E. McGill, Member

John Donoghue, Department Head
Department of Physics and Astronomy

Acknowledgements

This work has solidified my conviction that scientific understanding of astronomical objects requires us to span the electromagnetic spectrum. In so doing, we as scientists will grow to depend on one another increasingly. I'm sure I cannot adequately acknowledge everyone who has shared data, resources, and expertise, but I am grateful to all of them nonetheless. I would like to begin by acknowledging the simple but amazing discoveries of Yuji Hyakutake, Alan Hale and Tom Bopp.

The real star of this work is the QUARRY receiver, and all the people who dedicated years of their lives to make it work so well for so long. I wish to express my gratitude to all those who "volunteered" to help with observations during the Hyakutake 24-hour campaign, when remote observing was yet a dream: Chris Brunt, Mark Heyer, Bill Irvine, Mari-Paz Miralles, Preethi Pratap, and Jessica Rosenberg. I am grateful to Mike Brewer for his tireless efforts to set up remote observing for the Hale-Bopp campaign, sparing us from the perils of Prescott Road and undoubtedly saving several marriages. Even with remote observing, however, this work would not have been possible without the dedicated service of the comet team: Chris DeVries, Jimmy Dickens, Bill Irvine, Matt Senay, and Pete Schloerb. I am also deeply indebted to Ted Bergin for sharing generously his ion-molecule chemistry models, as well as many detailed explanations.

Naturally, I acknowledge my advisor Pete Schloerb for all his efforts, particularly his ability to take difficult problems and give them new direction. He is a man of cool ideas, and I am grateful to have been the recipient of some of those. If it had not been for Pete's vision for what an array receiver could do in the study of comets, this thesis certainly would not exist. I am also truly thankful for Pete's understanding and

unique ability to discuss scientific issues in the distracting presence of an exuberant, impatient, or all-too-infrequently sleeping baby and/or child.

I thank my other committee members for years of patience, advice, and flexibility when "targets of opportunity" totally redesigned my thesis topic. I thank my outside member, George McGill, for keeping me interested in geological aspects of solar system research, for improving my figure captions, and for still being willing to serve on my committee even after Venus and asteroids were gone. I thank Bill Dent for being willing to show up the morning of my defense with no prior notice, and still making helpful suggestions! I also thank Mike Skrutskie for helpful comments, and for attending my defense in spite of the potential imminent birth of his second child. I thank Bill Irvine for his endless stream of ideas, for his unique perspective on the study of comets, and for keeping my sentence structure in line.

I am grateful to Jimmy Dickens for co-existing with me in the Tennessee corner, for answering all those questions shouted around the wall, especially regarding partition functions, for doing a truly generous share of the comet observing, and for sharing his books. I thank Chris DeVries also for making the 6th floor a good place to work, for being a very good sport about observing under duress, and for his God-like knowledge of C.

Any acknowledgement would be incomplete without mention of all the people who helped me, both logistically and emotionally, with my children. "Auntie" Meg Lysaght provided a fun office to visit, lots of warm knitted items, and "sitting on" one or both of my kids on occasions too frequent to count. Together with Jessica Rosenberg and other assorted residents of the Happy House, she provided bed & breakfast to save me long drives at odd hours. Jessica deserves further credit for being such a good sport and helping me with my child/ren on occasions too numerous to count (the most notable of these being the trip to Tenerife!), allowing me to stay in her house, and for sharing her library most generously.

I am deeply grateful to the whole FCRAO office staff for who they are AND what they do, for their infinite patience with last-minute Fed Ex envelopes, jammed copiers, transparency requests, delinquent travel forms, not to mention making sure the students get paid on time! Eron, Allen, and I thank Barb Keyworth for her open lap policy and willingness to share her snacks; Denise Sallee and Pam Poissant for cool screen savers, highlighter pens, and countless cheerful greetings in the hallway; and Sally Rule keeping those little cans of "food for thought" on her desk, and for her love of animals, including humans.

My extended family has been amazingly supportive of this unusual pursuit, which will make me the first of my direct relatives to earn a PhD. I appreciate all the prayers of support and inquiries regarding my progress, particularly those of Grandmother Lovell and Grandmother Smith, both of whom passed away during this endeavor. I have deep gratitude to my parents for their support, both silent and spoken. When times were tough, I could always look to my father-in-law Allen Smith for inspiration and empathy in the toils of grad school. Finally, I am grateful to my husband, David Smith, for his support and encouragement, as well as patience with the delays associated with "targets of opportunity." Without his encouragement and insistence, I probably would not have completed my degree. While I know our discussions around the dinner table are rather atypical, I appreciate his interest in my course of study, and tireless assistance with computer and computing difficulties.

Abstract

Millimeter-wave Molecular Mapping of Comets Hyakutake and Hale-Bopp

February 1999

Amy J. Lovell, B.A., Agnes Scott College

Ph.D., University of Massachusetts Amherst

Directed by: Professor F. Peter Schloerb

The inner solar system passes of the bright comets C/1995 O1 Hale-Bopp and C/1996 B2 Hyakutake, coupled with modern, sensitive millimeter-wave instrumentation provided an opportunity to make unprecedented maps of molecular emission from cometary comae. We present the results of the 3-mm observing campaign to study these comets at the Five College Radio Astronomy Observatory (FCRAO). Observations of both comets in the HCN J=1-0 rotational transition provide a good record of the emission over a long period of time. The HCN production rates of comet Hyakutake are consistent with the observed pre-perigee visual brightening, concurrent with obvious spatial asymmetries in the maps. Monte Carlo simulations of the quiescent comet achieve best results with collision-dominated excitation over the observed coma, and a variation in outflow velocity with cometocentric distance. Simulations during the time of the outburst reveal that local enhancements in the emission, up to a factor of 5 over the isotropic outgassing, can account for the observed features. Searches for 3-mm molecular lines of CN, HC_3N, and CH_3OH were conducted, and upper limits are presented. Similar observations and modeling of comet Hale-Bopp confirm the need for modeling a gradient in the coma outflow velocity, and shed further light on how spectral line maps are affected by the presence of spatially asymmetric emission.

Comet Hale-Bopp was also mapped in the 3-mm emission of the ion HCO^+. HCO^+ is detectable over an extended region at the comet, with the peak emission commonly located 50,000–100,000 km in the antisolar direction. Maps made throughout the apparition show significant time-variability in the structure of the HCO^+ coma; however, the bulk properties of the emission remain constant. The HCO^+ brightness is usually depressed at the nucleus position, and on some occasions, the emission is spread into a ring or horseshoe. Individual spectra within the maps display broad lines redshifted from the nominal velocity of the nucleus, with the redshift typically increasing in the antisolar direction. The spectra and maps may be generally explained by models in which the ions are accelerated tailward at a rate $\sim$ 10 cm s^{-2}, provided that HCO^+ is destroyed near the nucleus. This destruction is presumably achieved via ion-molecule chemical reactions.

Table of Contents

List of Tables

List of Figures

Chapter 1

Introduction

1.1 General introduction

Since antiquity, the apparition of a comet has been an awe-inspiring sight. Although the modern era is not free from superstitions regarding these objects, much has been achieved in terms of scientific understanding. The predicted return of comet Halley in 1758–1759 enhanced understanding of comets as celestial bodies in orbit about the Sun. In the middle part of this century, it became understood through the theory of Oort (1950) and others that these orbits placed most comets well beyond the planets, from 50,000 to 150,000 AU heliocentric distance at aphelion. Around the same time, Whipple (1950) put forth the now widely accepted "dirty snowball" model for a cometary nucleus, wherein ices containing C, H, O, and N are combined with dust to form a fragile conglomerate structure. When a comet approaches the Sun, these volatile species are liberated from the nucleus along with grains of dust, to form an expanding atmosphere or *coma*. Interactions with the solar wind (Biermann 1951) and radiation field affect the motions of the neutral, ionized, and dusty components of the coma, forming tail structures.

Comets are believed to be the most primitive remaining bodies in the solar system, in that they have suffered minimal heating and radiation since the time of their formation and ejection to the Oort cloud. As such, these distant icy bodies offer a window into past epochs, and perhaps they have even preserved material from the interstellar cloud out of which the solar nebula formed (Greenberg 1993). The nucleus of a "new" comet — one which has not ventured into the inner solar

system since its formation — may be representative of early chemical and isotopic abundances and may contain clues about physical conditions that were present in the primitive solar nebula (Greenberg & Shalabiea 1994; Crovisier 1994a; Mumma, Weissman, & A. 1993). Thus, each comet that wanders near the Earth in a pass through the inner solar system may provide insight into the time of solar system formation.

1.2 Cometary observations at millimeter wavelengths

The study of comets can potentially provide insight into the physical conditions and chemical composition present during the early stages of solar system formation. Numerous types of observations can be, and have been, made of comets as they approach and recede from the Sun. Due to the wide range of structures and constituents which can be observed in the cometary environment, scientific understanding is greatly facilitated by observations at multiple wavelengths. In the latter part of this century, comets have been probed by both ground- and space-based instrumentation, spanning the spectrum from radio to X-Ray. Each wavelength provides a unique perspective, with the goal of determining properties of the cometary nucleus, and advances in instrumentation have allowed for the detection of numerous cometary constituents, including molecules, atoms, ions, and dust grains.

The close approach of a comet to the Sun affords both a challenge and an opportunity. Since cometary nuclei are small, dark objects which largely remain at great distances, they are nearly impossible to observe until an orbital perturbation sends one closer to the Sun. At that point, however, the sublimation of volatiles and the release of dust obscures the view of the nucleus. Thus, the scientific pursuit of comets necessitates some means of employing observable phenomena to infer properties of the nucleus. One tactic is to observe the material which is directly sublimated from the nucleus, and to assume that it is indicative of the

nuclear composition. Molecular species which are believed to be such sublimation products are known as "parent" molecules, and can be observed through rotational and vibrational spectral lines in the millimeter-wave and infrared portions of the spectrum.

The millimeter wavelength regime contains a wealth of spectral lines from the rotational transitions of many molecules. For cometary observations at large distances from the Sun, where kinetic temperatures are low, thermal excitation tends to populate only the low-energy transitions in this wavelength range. Furthermore, modern spectrometers provide excellent spectral resolution, enough to allow assessment of the kinematics in the coma (Crovisier & Schloerb 1991). Millimeter-wave observations have yielded the first detections of many cometary species (*cf.* Mumma, Weissman, & A. 1993, Crovisier 1994a, Crovisier 1998, Despois 1998, Lis *et al.* 1998), including some isotopic species and ions. Observations of several transitions of a molecule can be used to determine the rotational temperature in the coma (Bockelée-Morvan *et al.* 1994), and hyperfine structure in the lines is used to constrain the optical depth (Irvine *et al.* 1998). The width and shapes of these well-resolved spectral lines have been used to determine the outflow velocity in the coma (*cf.* Bockelée-Morvan, Crovisier, & Gérard 1990, Biver *et al.* 1997).

1.3 The millimeter-wave array receiver

For a dynamic object such as a comet, it is highly desirable to be able to make reliable observations quickly, preserving a "snapshot" of the object. Furthermore, it is desirable to repeat observations over long periods of time, in order to track changes in the object as it approaches and recedes from the Sun. At optical and infrared wavelengths, multi-pixel CCD imaging has become an invaluable tool for the study of comets. However, longer wavelength observations (sub-millimeter through centimeter) have traditionally been carried out with a single beam, and

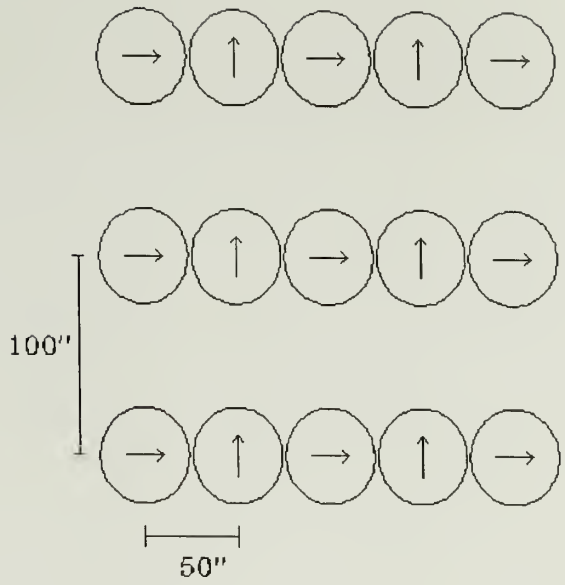

Figure 1.1. Diagram of 15-element QUARRY receiver positions, as they appear on the sky. Beams are separated by 50″ along the rows, with rows separated by 100″. Arrows indicate the direction of linear polarization for each pixel.

spatial coverage of an astronomical object was achieved only through repeated pointings of the telescope. Such procedures often require a great deal of observation time, which is problematic for moving, changing objects such as comets.

The millimeter-wave array receiver QUARRY (Erickson *et al.* 1992), first implemented on the Five-College Radio Astronomy Observatory (hereafter FCRAO) 14-m telescope in 1991, provided a view of 15 sky positions simultaneously. QUARRY is an array of millimeter-wave receivers, operating in the range 86–115 GHz, arranged as 3 rows of 5 beams, as seen in Figure 1.1. This instrument is advantageous, particularly for time-critical investigations, as it provides simultaneous coverage over a 4–5 arcminute region of the sky. Such simultaneous observations reduce errors which can arise due to atmospheric disturbances and pointing uncertainties, and the nominal "footprint" of the array

on a comet at 1 AU encompasses a large fraction of the gas coma for most molecules observed in this frequency range.

The efficiency of this instrumentation makes it possible to assemble an acceptable image of a bright comet over time scales as short as a few hours. In addition, the 1024-channel autocorrelating spectrometer FAAS (Predmore 1995) provides excellent spectral resolution, approximately 70 m s^{-1} for observations near 100 GHz. This combination of spatial and spectral resolution is ideally suited for cometary observations, as it provides numerous constraints for coma models. In contrast, single pixel observations yield a single spectrum, generally observed at the position of the nucleus. As such, the distribution of emission over the rest of the coma must be assumed in order to interpret the data. Mapping observations provide multiple spectra, covering a significant portion of the coma, and placing additional constraints on the distribution of emission. Furthermore, the variations (if any) in line shape among the observed spectra have implications for the kinematics of gas in the coma, even at spatial scales below the beam resolution. Finally, repetition of such mapping observations over an extended period of time (such as the apparition of a comet) provides the opportunity to monitor these structures and their evolution.

1.4 This work

The apparitions of comets C/1996 B2 Hyakutake and C/1995 O1 Hale-Bopp in 1996 and 1997 provided unprecedented opportunities to investigate comets in the inner solar system. In particular, these were the first bright comets to pass through the inner solar system after the widespread establishment of modern, sensitive millimeter-wave instrumentation. This thesis presents the results of investigations of comets Hyakutake and Hale-Bopp, employing the QUARRY millimeter-wave array receiver and FAAS 1024-channel autocorrelating spectrometer at FCRAO. The linear molecule HCN was detected in its J=1-0

rotational transition, and mapped in both comets for at least some portion of the apparition. This molecule, comprised of three of the four elemental (CHON) components proposed by Whipple (1950), is of interest as a possible parent molecule for the CN radical, one of the earliest known coma constituents. Due to its suitability for longer-wavelength observations, through several transitions in the millimeter-wave and sub-millimeter windows, HCN has become a secondary benchmark species for radio observations of cometary molecules (Lis *et al.* 1998). Furthermore, the nitrogen component creates hyperfine structure in the spectral lines which allows constraints on the optical depth in the coma.

For comet Hyakutake, the linear molecule HCN was mapped in its J=1-0 transition, in an observing campaign which spanned approximately 3 months. While all observations with the array receiver provide spatial coverage in the coma, the extent of emission and signal-to-noise ratio permitted useful images to be assembled only for the time immediately surrounding the perigee of the comet March 25, 1996. Maps over this 10-day period provide an excellent record of coma structures and kinematics over that time. Due to the close approach of the comet, just slightly more than 0.1 AU from the Earth at perigee, our observations probed the inner portions of the coma, within 10,000 km of the nucleus. The observations revealed strikingly different map morphologies and line shapes over the course of the apparition. Observations were attempted up to perihelion, which occurred approximately 0.25 AU from the Sun, but HCN J=1-0 was beyond our detection limits at that time.

For comet Hale-Bopp, which was discovered well in advance of its perihelion, HCN observations spanned 10 months time. In addition, spectral line maps of the CS radical and the HCO^+ ion were made over 4 months. The comet was observed in all 3 detected molecules both pre- and post-perihelion, with the HCN observations spanning heliocentric distances up to 3 AU pre-perihelion. In

comparison with comet Hyakutake, comet Hale-Bopp remained fairly distant from the Earth as well as from the Sun: perigee and perihelion occurred within one week, at 1.3 and 0.9 AU, respectively. At this distance, the observations of HCN encompassed a much larger region of the coma, over 100,000 km. Fortunately, the large production rate of the comet permitted the comet to be detected at large heliocentric and geocentric distances.

Mapping observations of comet Hale-Bopp yielded a good record of the gas production, coma structures, and kinematics in the neutral coma over a significant portion of the apparition. Few asymmetries in the distribution or line shape of HCN were detected, which is not surprising given the large observed scale. Mapping observations of HCO^+, on the other hand, revealed striking asymmetries in both the distribution of emission and in the line shapes (Lovell *et al.* 1997). HCO^+ was detected over extended area, so much so that a full map required four footprints of the array. The peak in the HCO^+ emission typically appeared offset from the nucleus in an anti-Sunward sense, and on some occasions a local minimum in emission appeared near the nucleus position. The observed spectral lines were very broad, and redshifted considerably with respect to the cometocentric velocity. Furthermore, this redshift increased with distance from the comet on in the anti-Sunward (tail) side of the maps. All of these features were common to the entire set of HCO^+ observations; however, considerable variations in map morphology and strength of emission likely occurred on timescales shorter than the mapping time.

The initial study of HCO^+ mapping observations in comet Hale-Bopp have been published along with a simple interpretation of the observational results (Lovell *et al.* 1998b). The large extent of the emission and the redshift in the observed spectral lines can be understood in terms of the anti-Sunward acceleration of ions due to interactions with the solar wind and magnetic field.

The anti-Sunward shift in the peak emission and the appearance of a local minimum near the nucleus add an additional constraint to the interpretation, and appear to require suppression of HCO^+ in the inner coma. We have proposed that HCO^+ is formed via ion-molecule reactions, but is rapidly destroyed within a critical distance from the nucleus. These mechanisms have been discussed briefly by Lovell *et al.* (1998a). This study of HCO^+ represents the first millimeter-wave mapping of a cometary ion.

Comets Hyakutake and Hale-Bopp were strikingly different in size, gas production, and observation distance; thus, the two sets of observations reveal different properties of the comets. Comet Hyakutake provided a glimpse of the inner coma, along with the associated challenges of modeling both excitation and velocity structures. Comet Hale-Bopp provided a "big-picture" look at a very productive comet, and a first chance to map an ion in the millimeter regime. In the chapters that follow, we present the results of the mapping campaign to observe these comets, beginning with Hyakutake in Chapter 2, moving to the neutral-species observations of Hale-Bopp in Chapter 3, and ending with the spectacular results of mapping the ion HCO^+ in Hale-Bopp in Chapter 4. All these observations nicely demonstrate the power of array receiver observations in the study of comets, and provide a basis for comparison of Hyakutake with Hale-Bopp. In addition, these Hale-Bopp observations allow comparison between the distributions of neutral and ionized species. These comparisons are drawn with a summary of the results in Chapter 5.

Chapter 2

Molecular Observations and Mapping of Comet Hyakutake

2.1 Introduction

Comet C/1996 B2 was discovered by Yuji Hyakutake on January 30, 1996 (Nakamura *et al.* 1996), less than 2 months prior to its close pass by the Earth. In spite of the short notice, many observations over a wide range of wavelengths were planned and carried out worldwide to study this object. The comet passed 0.102 AU from the Earth on March 25, 1996, and then proceeded to a perihelion passage at 0.25 AU from the Sun on May 1, 1996. In size, the nucleus is thought to be fairly small, with a diameter of approximately 2 km (Sarmecanic *et al.* 1997; Fernández *et al.* 1997; Harmon *et al.* 1997), rotating with a period of 6.2 hours (Schleicher *et al.* 1998;Jorda, Lecacheux, & Colas 1996). The gas production rate was approximately 2×10^{29} mol s^{-1} at the time of closest approach to the Earth (Gérard *et al.* 1997).

This apparition of comet Hyakutake provided the first opportunity to study an Earth-approaching comet since the 1983 apparition of C/1983 H1 (IRAS-Araki-Alcock). Since that time, many advances have been made in astronomical instrumentation which are beneficial for the study of comets. In particular, millimeter-wave receivers have become extremely sensitive, dramatically lowering detection thresholds for observations of cometary parent molecules. In addition, the millimeter-wave array receiver provides the ability to image molecular emission from the coma, over timescales appropriate to the observation of such a dynamic target. The combination of spatial and spectral

resolution permits detailed assessment of the composition, structure, and kinematics of the cometary coma. Furthermore, repeated mapping observations record the time evolution of these phenomena.

This chapter presents the results of the campaign to observe comet Hyakutake at the FCRAO. We accumulated a good record of the HCN emission over a long period of time, in addition to arcminute-scale (5000–10000 km at the comet) maps of the emission during the 10 days surrounding perigee. During this time, HCN production gradually decreases, contrary to the expected increase in inverse proportion to heliocentric distance. This observation is likely associated with the observed visual brightening in the comet, perhaps due to a small nuclear splitting event a few days prior to perigee (Lecacheux *et al.* 1996; Lis *et al.* 1997). Asymmetries are apparent in both the spectra and the maps, possibly corresponding to jets observed at other wavelengths. Searches for other molecular lines were also conducted, including 3-mm transitions of CN, HC_3N, and CH_3OH, and upper limits for these species are presented.

2.2 Observations

The apparition of comet C/1996 B2 Hyakutake presented the first opportunity to employ the FCRAO 15-element QUARRY focal plane array (Erickson *et al.* 1992) along with the 1024-channel autocorrelating spectrometer to observe a comet[1]. The spectrometer provided excellent resolution in the spectral lines, with channel spacing of 19.5 kHz, corresponding to a velocity resolution around 70 m s^{-1}.

2.2.1 Spectral line data

Observations of comet Hyakutake at the FCRAO 14-m telescope began in late February, 1996, and continued until just past perihelion in early May. For at least

[1]observations of periodic comet Swift-Tuttle were made in 1993 using the array receiver and lower-resolution filterbanks

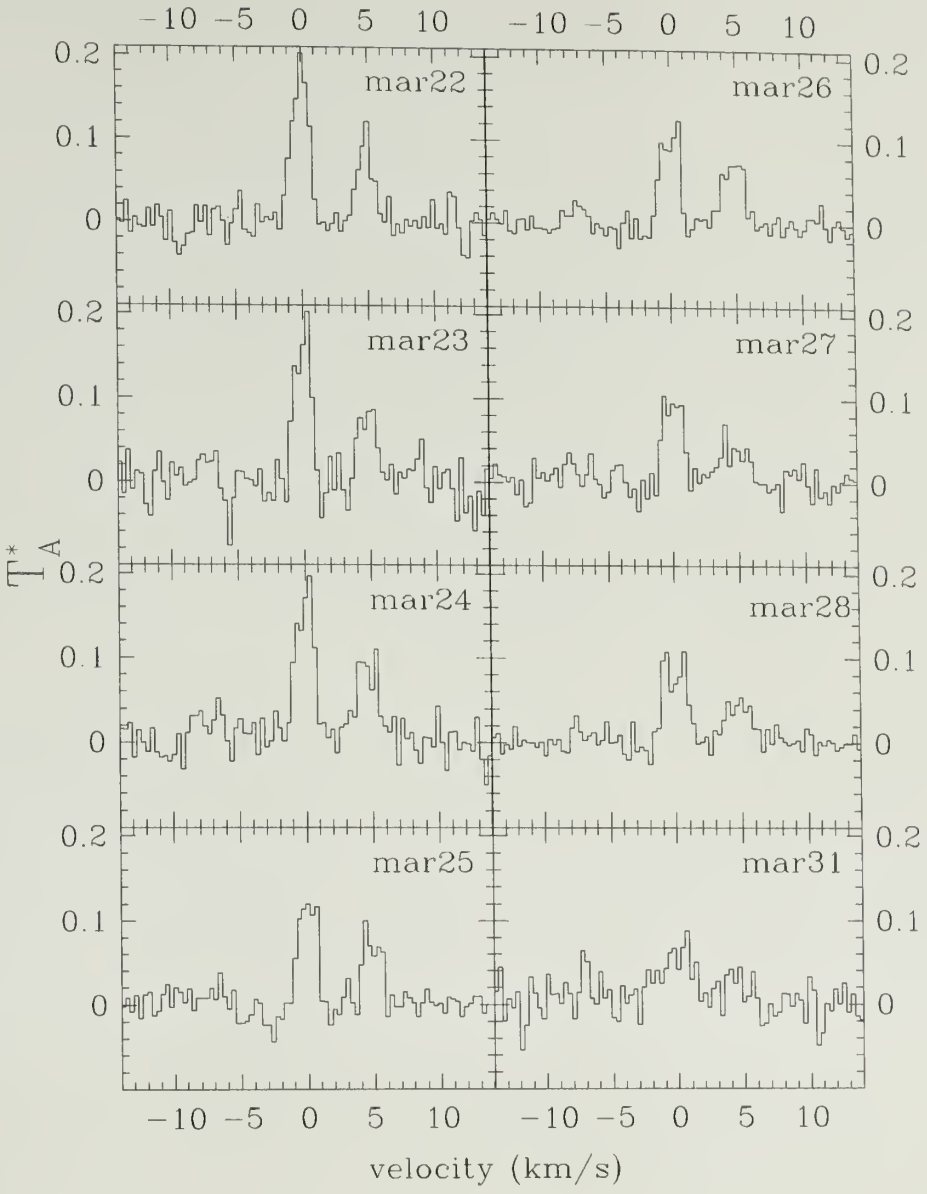

Figure 2.1. Spectra of HCN J=1-0 in comet Hyakutake for March 22–31, 1996. On these dates, the post-convolution beam resolution is 7,000–9,000 km in the coma, except for March 31, when a larger convolution was used, yielding an effective resolution of $\sim$ 13,000 km. Spectra have been smoothed over 5 original channels. In most spectra, the F=2-1 and F=1-1 hyperfine components can be seen, at cometocentric velocities of 0.00 km s^{-1} and 4.84 km s^{-1}, respectively. The third component, F=0-1, at a cometocentric velocity of -7.06 km s^{-1}, generally lies within the noise level. Note the progression in the shape of the principal line from a single, asymmetrical peak on March 22, to a symmetrical double peak on March 28.

some portion of each observing day, the HCN J=1-0 rotational transition at 88.631847 GHz was observed in order to track the activity level in the comet and to ensure that the ephemeris was appropriate. At this frequency, the half-power beam width is approximately 60″ with a beam efficiency of $\eta_b = 0.5$. The result of these HCN observations is a good record of the emission over a long period of time, as shown in Table 2.1. A sampling of the HCN lines at the ephemeris position of the nucleus are shown in Figure 2.1. In addition, 3 mm transitions of CN (113.5 GHz), HC_3N (100.1 GHz), and CH_3OH (96.7 GHz) were sought but not detected. These observations are summarized in Table 2.2.

HCN and HC_3N transitions were observed using 20 MHz bandwidth with a spectral resolution of 19.5 kHz (0.066 and 0.059 km s^{-1}, respectively). CN and CH_3OH transitions were observed using 40 MHz bandwidth with a spectral resolution of 78.1 kHz (0.21 and 0.24 km s^{-1}, respectively). Early data for HCN, from 26 February to 12 March, and the CH_3OH data on 27 March were position-switched with a reference position 0.5° in azimuth away from the comet nucleus. All other spectra, beginning on 13 March, were frequency-switched as noted in Tables 2.1 and 2.2. The comet ephemeris was calculated in real time at the telescope, using orbital elements given by D. Yeomans of JPL, at epochs updated throughout the observing period (solution numbers noted in Tables 2.1 and 2.2). Errors between the ephemeris prediction and the actual position of the comet are expected to be less than a few arcseconds during this time (D. Yeomans, personal communication 1998).

2.2.2 Mapping and Data Processing

All observations were made with the 15-pixel array receiver. Thus, every observation contains information on the spatial distribution of the observed species. Mapping with the 5-by-3 array provided good spatial coverage of the comet, spanning approximately 4′ of sky with individual beam resolutions near one

Table 2.1. Log of FCRAO observations of HCN in comet Hyakutake

UT Date (1996)	Δ (AU)	r_h (AU)	time (hours)	obs. mode	Yeomans Ephemeris
26.39 Feb	0.940	1.581	3.90	PS 0.5°	Solution 06/1996 Mar. 01
27.39 Feb	0.906	1.563	3.70	PS 0.5°	Solution 08/1996 Feb. 25
29.39 Feb	0.839	1.526	3.82	PS 0.5°	
01.39 Mar	0.805	1.508	3.58	PS 0.5°	
02.36 Mar	0.772	1.490	2.62	PS 0.5°	
04.35 Mar	0.705	1.453	2.98	PS 0.5°	Solution 09/1996 Mar. 10
05.34 Mar	0.672	1.435	3.10	PS 0.5°	
09.44 Mar	0.538	1.359	1.02	PS 0.5°	
10.36 Mar	0.506	1.340	4.60	PS 0.5°	Solution 10/1996 Mar. 10
11.34 Mar	0.477	1.323	3.94	PS 0.5°	
12.34 Mar	0.444	1.304	4.02	PS 0.5°	
13.33 Mar	0.412	1.284	4.85	FS 6.0	
14.32 Mar	0.379	1.265	4.36	FS 6.0	
21.32 Mar	0.167	1.125	2.40	FS 6.0	Solution 16/1996 Mar. 20
22.28 Mar	0.143	1.105	8.57	FS 6.0	
23.17 Mar	0.123	1.086	3.00	FS 6.0	
24.17 Mar	0.108	1.065	3.34	FS 6.0	Solution 16/1996 Mar. 23
25.19 Mar	0.102	1.044	4.80	FS 6.0	Solution 16/1996 Mar. 25
26.77 Mar	0.113	1.011	1.73	FS 6.0	Solution 16/1996 Mar. 27
27.00 Mar	0.116	1.006	8.81	FS 6.0	
27.87 Mar	0.131	0.989	4.10	FS 6.0	
28.83 Mar	0.154	0.967	12.56	FS 6.0	
29.68 Mar	0.179	0.947	3.20	FS 6.0	Solution 16/1996 Mar. 30
30.44 Mar	0.197	0.933	8.17	FS 6.0	
31.01 Mar	0.214	0.919	9.23	FS 6.0	
06.91 Apr	0.427	0.764	9.50	FS 6.0	Solution 28/1996 Mar. 30
15.78 Apr	0.715	0.548	12.45	FS 6.0	Solution 34/1996 Apr. 13
22.70 Apr	0.943	0.375	7.12	FS 6.0	Solution 34/1996 Apr. 20
23.76 Apr	0.978	0.349	10.53	FS 6.0	
05.75 May	1.242	0.277	7.95	FS 6.0	IAUC 6391, 1996 Apr. 27

time given is the elapsed time of the observation on the given date

Orbital elements from JPL WWW Site, at given Epoch.

PS denotes position-switching by indicated amount

FS denotes frequency-switching in MHz.

Table 2.2. Log of observations of other molecules in comet Hyakutake

UT Date (1996)	Δ (AU)	r_h (AU)	time (hours)	obs. mode	Yeomans Ephemeris
CH_3OH 2-1 96.747 GHz at 40 MHz bandwidth					
27.36 Mar	0.123	0.997	6.78	PS 0.5°	Solution 16/1996 Mar. 27
27.67 Mar	0.129	0.991	4.74	PS 0.5°	
HC_3N J=11-10 100.0764 GHz at 20 MHz bandwidth					
28.26 Mar	0.141	0.979	13.58	FS 2.0	Solution 16/1996 Mar. 27
29.96 Mar	0.185	0.941	14.03	FS 2.0	
CN 1-0 J=3/2-1/2 113.499 at 40 MHz bandwidth					
23.38 Mar	0.119	1.082	2.55	FS 5.5	Solution 16/1996 Mar. 23
24.33 Mar	0.106	1.061	4.93	FS 1.35	
25.38 Mar	0.102	1.040	3.18	FS 1.35	Solution 16/1996 Mar. 25
29.34 Mar	0.169	0.954	12.29	FS 1.35	Solution 16/1996 Mar. 30

time given is the elapsed time of the observation on the given date
Orbital elements from JPL WWW Site, at given Epoch.
PS denotes position-switching by indicated amount
FS denotes frequency-switching in MHz.

arcminute. In many cases, however, a detection was made only in the central pixel of the array, if at all. Only during close passage by the Earth were the lines strong enough to be detected over a larger portion of the array. Between 13–23 March, 1996, full-beam sampling (5,000–14,000 km) was achieved with two pointings of the array per map. Thereafter, half-beam (Nyquist) sampling (2,000–4,000 km when detections were made), requiring 8 pointings of the array, was employed.

In order to maintain a fixed reference in comet coordinates, the array receiver was rotated to follow the position angle of the Sun-comet axis on the sky, illustrated in Figure 2.2. A rotation angle was entered manually by the observer in order to align the 5-pixel rows of the array (refer again to Figure 1.1) with the projected tail vector of the comet on the sky (according to the ephemeris in use, see Table 2.1). In order to create a map, all of the pointings of the array must be performed in the rotated reference frame. Unfortunately, these positions were improperly computed during the majority of this observing campaign, due to an

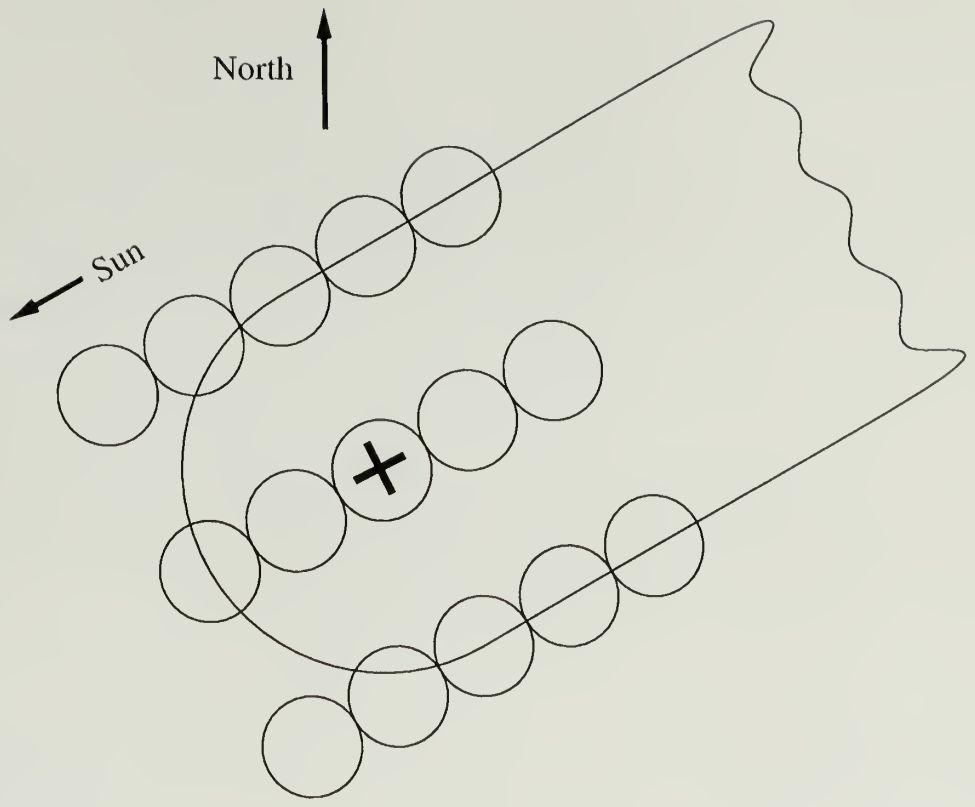

Figure 2.2. Illustration of the array position to follow the comet. The orientation of the array is chosen to align the center 5-pixel row with the Sun-comet axis.

error in the tracking software which failed to compensate for the changing declination of the comet. Near the celestial equator, the errors are minimal; however, near the celestial pole the map sampling is strikingly non-uniform. In order to create regular maps, as well as to interpret the maps on the physical scale of the comet, the raw spectra were convolved with a Gaussian convolution function and re-sampled onto a uniformly-spaced regular grid.

All maps were sampled at one-fourth of the convolution scale, which is tabulated, along with the observation circumstances for each map and the resulting effective resolution, in Table 2.3. For consistency among the maps during the period surrounding perigee, we employed a single convolution scale for all maps taken at $\Delta < 0.16$ AU. The value of 6,000 km (see Table 2.3) was adopted

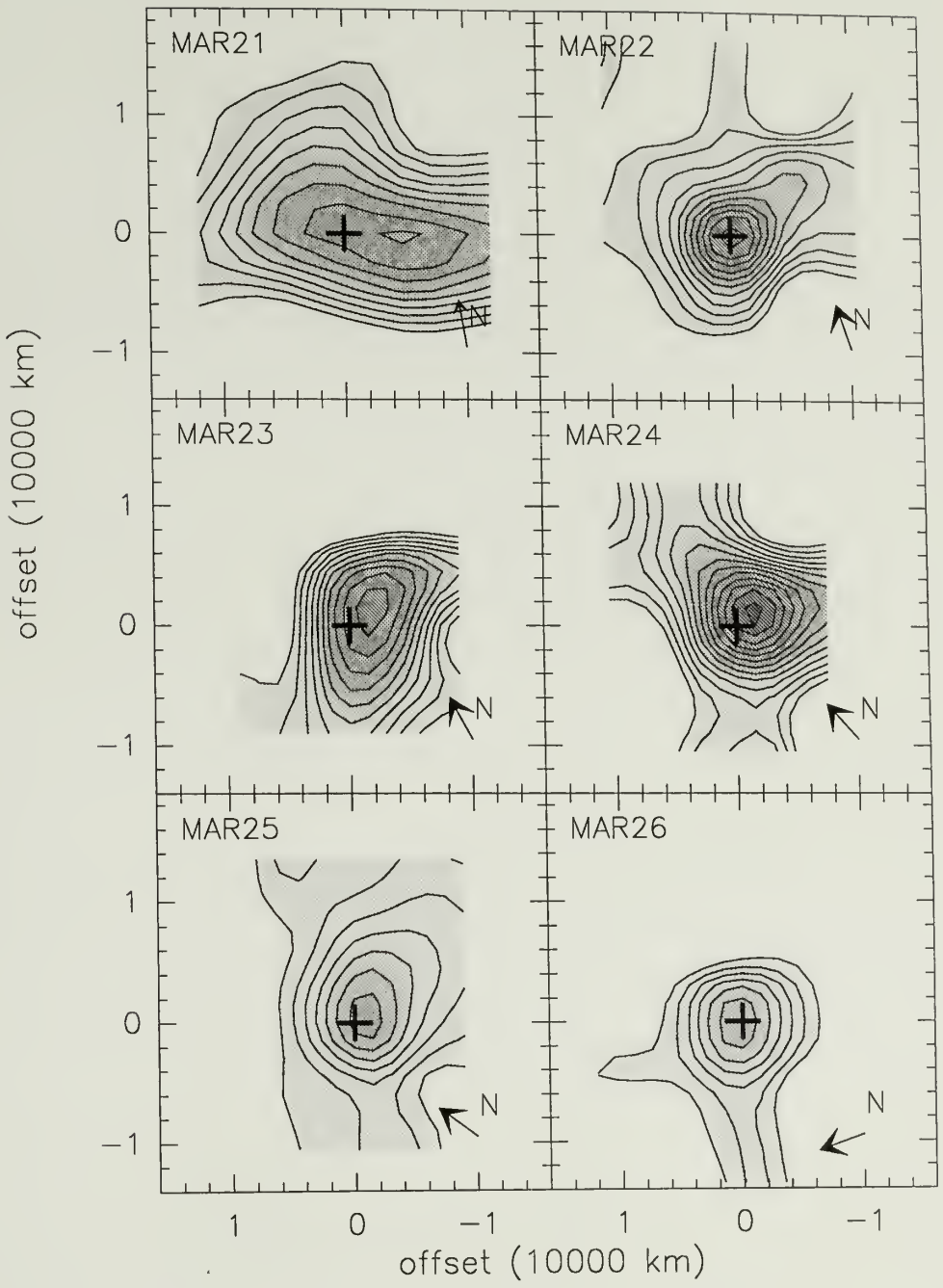

Figure 2.3. Maps of integrated intensity in the HCN J=1-0 F=2-1 line for comet Hyakutake between March 21–26, 1996. The cross indicates the assumed position of the nucleus, with the Sun to the left, and the direction of North as indicated. Contour levels begin at 80 mK km s^{-1} in intervals of 20 mK km s^{-1}, with progressively darker shading. The spatial axes of the map are in units of 10,000 km of the coma. For March 21, the effective post-convolution resolution in the coma is 12,000 km; for March 22–26, approximately 8,000 km.

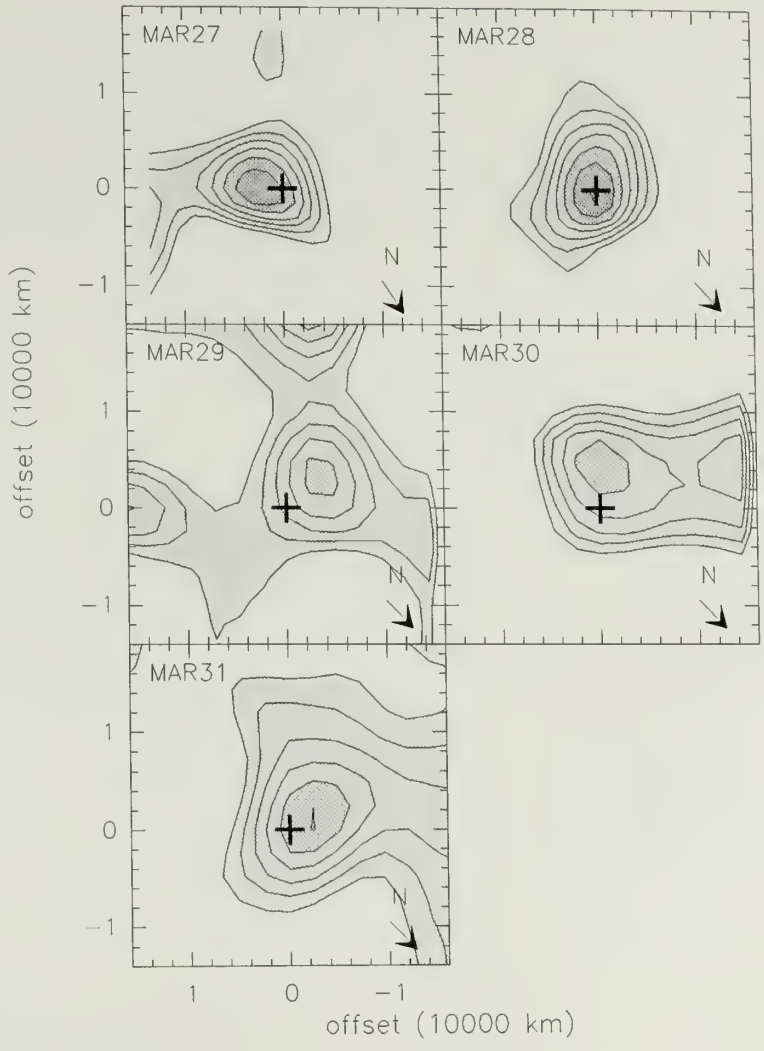

Figure 2.4. Maps of integrated intensity in the HCN J=1-0 F=2-1 line for comet Hyakutake between March 27–31, 1996. Symbols and contouring are as in Figure 2.3. On these dates, the effective post-convolution beam resolution is 7,000–9,000 km in the coma.

because it represents the average size of the telescope beam during the period March 22–28. For other observations with $0.16 < \Delta < 0.3$ AU, the signal-to-noise ratio was lower, though detections were still made over a number of pixels of the array. Thus, we employed a slightly larger convolution of 9600 km, which averaged more raw spectra into each convolved spectrum, lowering the effective resolution. For $\Delta > 0.3$ AU, the signal was quite weak, prohibiting effective mapping, so the value of 40,000 km was chosen to gather the majority of the emission into a single spectrum. Integrated intensity maps for the former two cases are displayed in Figure 2.3 and 2.4. The integrated intensities are computed over the interval from -1.5 km s^{-1} to 1.5 km s^{-1}, after the removal of a constant baseline from the spectra.

In order to assess the reality of observed features, and to highlight asymmetries in the observed emission, we also computed azimuthal averages of the raw spectra. Using the same convolution scales and sampling size as for the grid maps (Table 2.3), individual spectra were averaged in annuli the width of the grid sample spacing. The integrated intensities of these azimuthally averaged spectra were then subtracted from the grid maps to create residual images. For the period from March 22–28, 1996, figures 2.5 — 2.11 display four products of the data: the upper left is the convolved integrated intensity map, with the grid of corresponding spectra (at half-beam intervals) on the upper right; the lower left is the residual image, with the corresponding azimuthally averaged profile on the lower right. The contour interval for all the intensity maps is 20 mK km s^{-1}, a typical value for the uncertainty over the entire time interval. In the residual maps, the contours lie at intervals of σ, the mean rms level for each date, beginning at 3 σ for both positive levels, indicating an excess of HCN with respect to the average, and negative levels, indicating a deficiency.

Table 2.3. Convolution Scales and dates for maps of comet Hyakutake

Avg. Date UT	Δ AU	r_h AU	ϕ_{ph} deg	map time hours	Convolution km	(effective beam) km	arcsec
1.10 Mar	0.815	1.513	36.9	23.70	40,000	53,000	89
11.16 Mar	0.482	1.326	38.3	13.58	40,000	45,000	128
13.80 Mar	0.396	1.275	38.2	9.21	40,000	43,000	151
21.32 Mar	0.167	1.125	36.8	2.40	9,600	12,000	98
22.28 Mar	0.143	1.105	38.1	8.57	6,000	8,500	82
22.20 Mar	0.144	1.106	38.0	4.66	6,000	8,500	82
22.38 Mar	0.140	1.103	38.4	3.91	6,000	8,400	83
23.17 Mar	0.123	1.086	41.3	3.00	6,000	7,900	89
24.17 Mar	0.108	1.065	48.5	3.34	6,000	7,500	96
25.19 Mar	0.102	1.044	60.1	4.80	6,000	7,400	100
26.96 Mar	0.116	1.007	82.3	10.54	6,000	7,700	92
27.87 Mar	0.131	0.989	90.9	4.10	6,000	8,100	86
28.83 Mar	0.154	0.967	97.4	12.56	6,000	8,800	79
28.70 Mar	0.154	0.967	97.4	6.41	6,000	8,800	79
28.96 Mar	0.154	0.967	97.4	6.15	6,000	8,800	79
29.68 Mar	0.179	0.947	101.5	3.20	9,600	12,000	94
30.44 Mar	0.197	0.933	104.2	8.17	9,600	13,000	89
31.01 Mar	0.214	0.919	105.8	9.23	9,600	13,000	85
06.91 Apr	0.427	0.764	111.3	9.50	40,000	44,000	142
15.78 Apr	0.715	0.548	104.4	12.45	40,000	50,000	97
23.33 Apr	0.964	0.359	86.1	17.65	40,000	57,000	81
05.75 May	1.242	0.277	29.0	7.95	40,000	66,000	73

Notes: Δ is the geocentric distance; r_h is the heliocentric distance; ϕ_{ph} is the phase angle. The effective beam is the post-convolution spatial resolution.

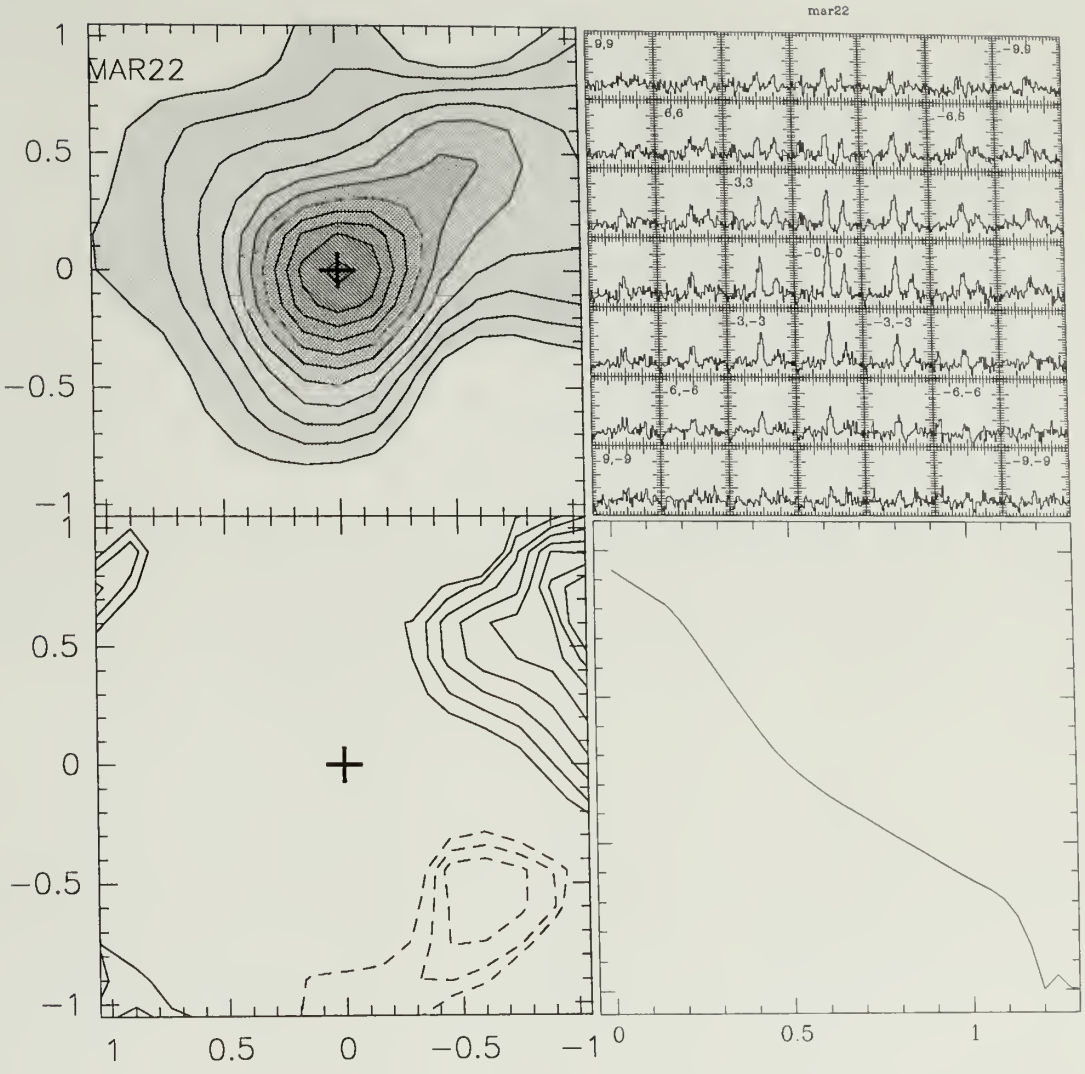

Figure 2.5. HCN mapping data for comet Hyakutake on March 22, 1996, in four representations. The upper left is the integrated intensity of the J=1-0 F=2-1 line, computed in the interval -1.5 km s^{-1} to 1.5 km s^{-1}, contoured at 20 mK km s^{-1}, beginning at 80 mK km s^{-1}. On the upper right is a grid of spectra at half-beam intervals, corresponding to the map on the left. All spectra are plotted with the same vertical scale as that of the (0,0) spectrum. The lower left is the residual image, contoured in intervals of σ = 10 mK km s^{-1}(the mean noise in the map), beginning at 3σ, in both positive levels (solid lines), and negative levels (dashed). In both images, the cross refers to the tracked position of the nucleus. On the lower right is the radial profile of integrated intensity which was subtracted from the map (at the upper left) to yield the residual. The peak integrated intensity is $\sim$ 300 mK km s^{-1}, plotted versus distance from the nucleus in units of 10,000 km.

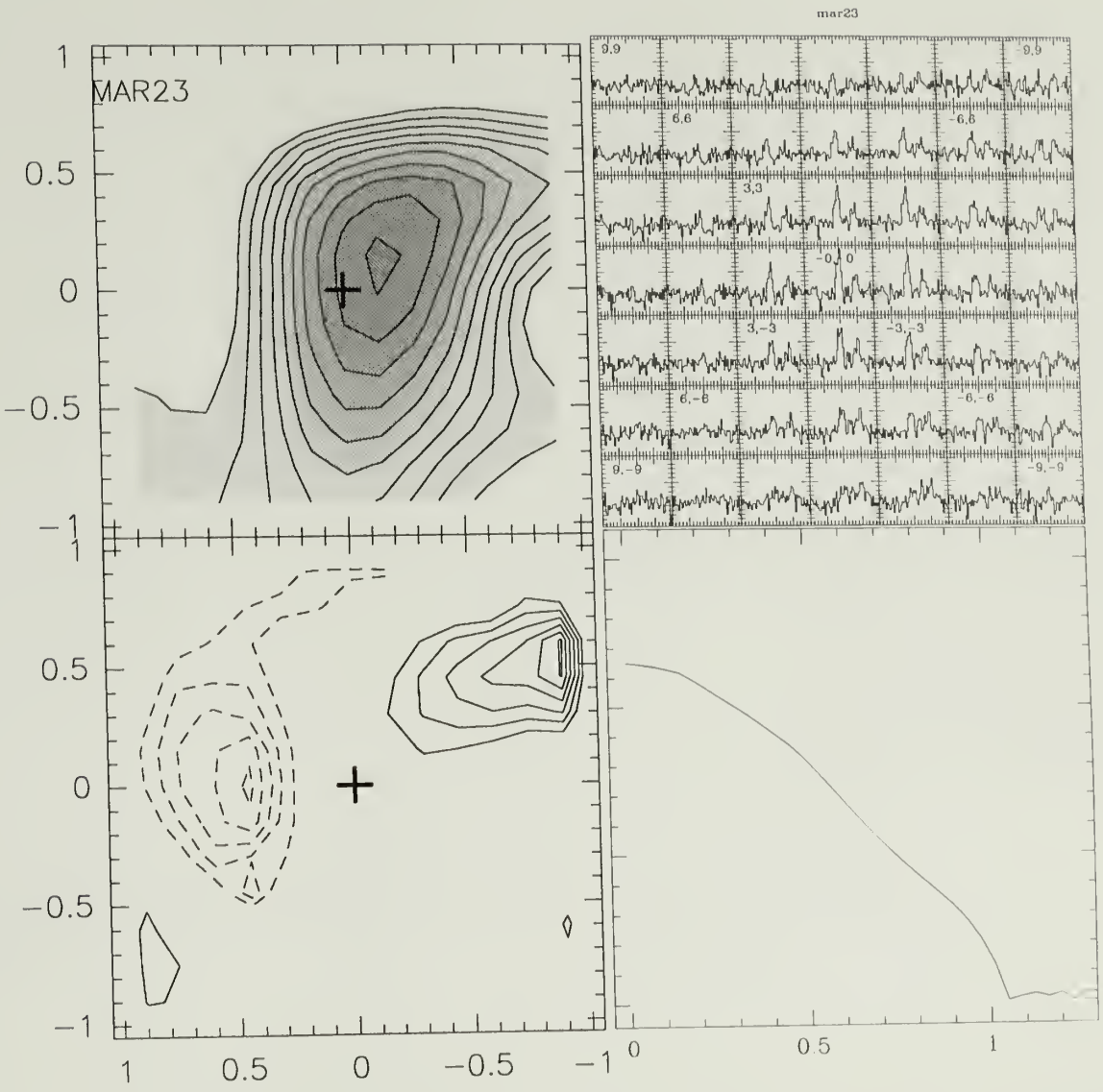

Figure 2.6. HCN mapping data for comet Hyakutake on March 23, 1996, in four representations, as in Figure 2.5. Contour levels in the integrated intensity map (upper left) and normalization of the radial profile (lower right) are consistent with those in Figure 2.5, as in the following figures. The vertical scale of the spectra and contouring of the residuals are according to this date only. The appearance of negative residuals in this case is most likely due to a discrepancy between the observed and the actual position of the nucleus.

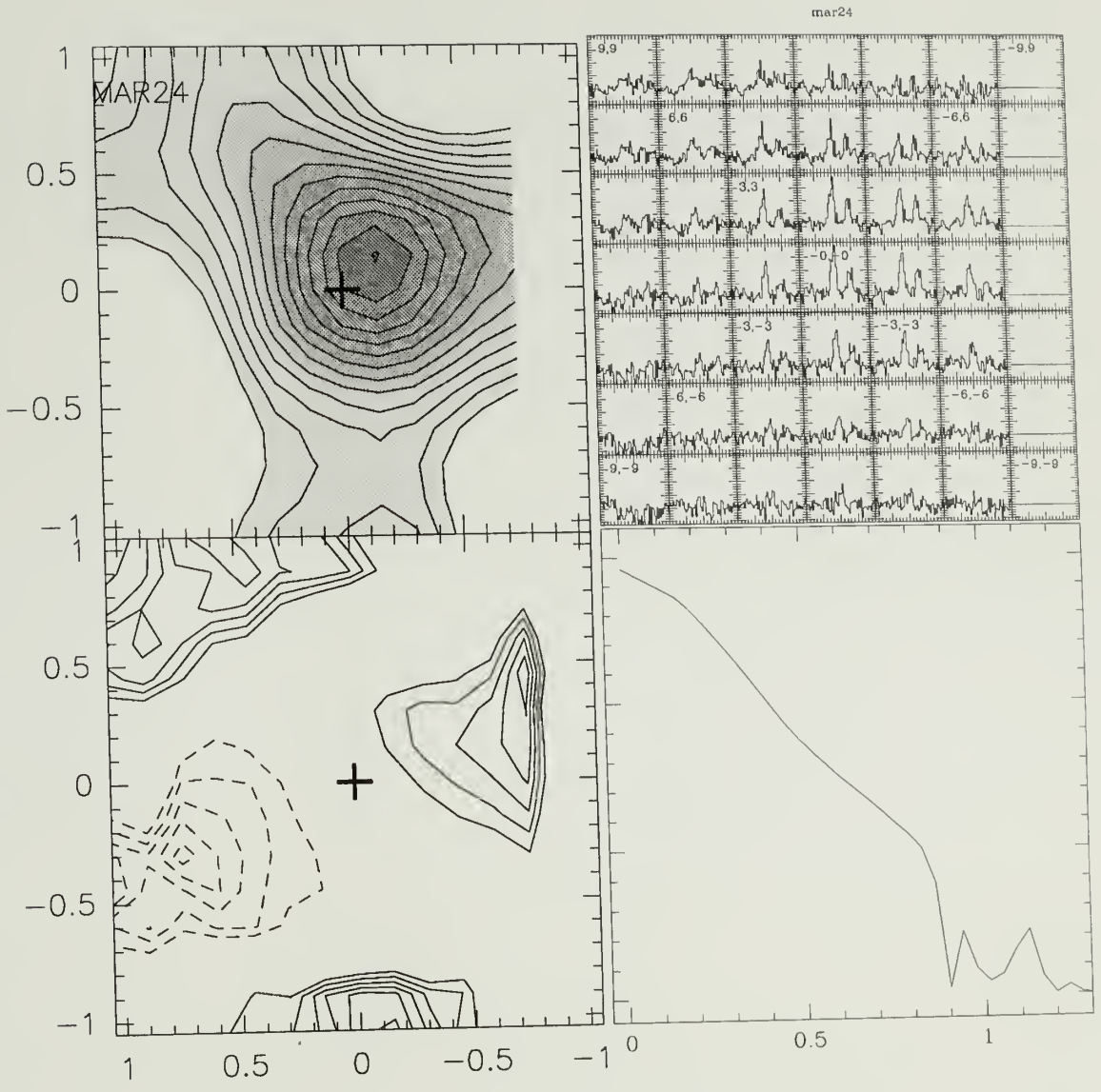

Figure 2.7. HCN mapping data for comet Hyakutake on March 24, 1996, in four representations, as in Figure 2.5. Again, the large negative residuals are attributed to a discrepancy in the observed versus actual position of the nucleus on the sky. The null spectra at the right fell outside the observed sky area of the array on this date.

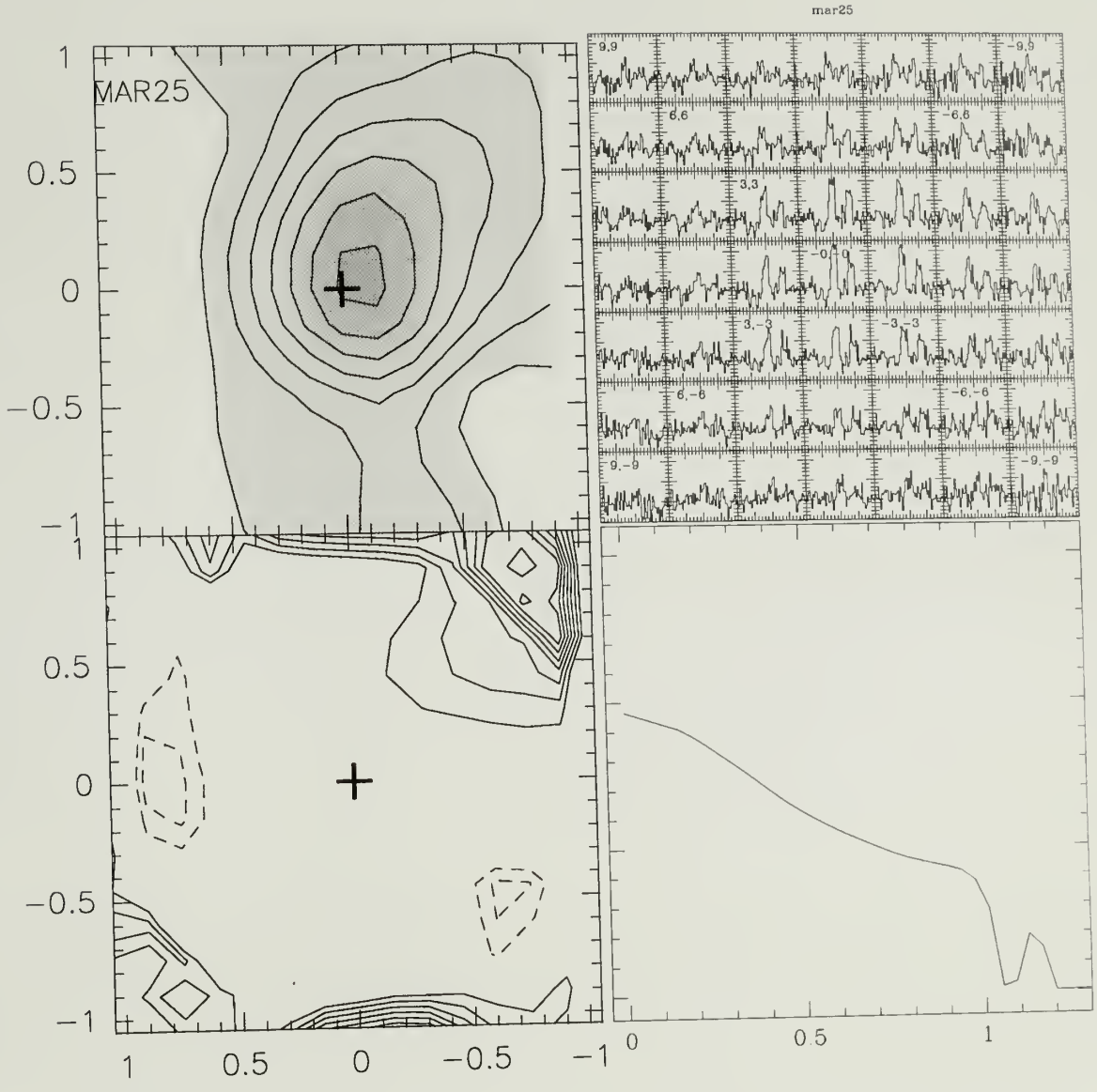

Figure 2.8. HCN mapping data for comet Hyakutake on March 25, 1996, in four representations, as in Figure 2.5.

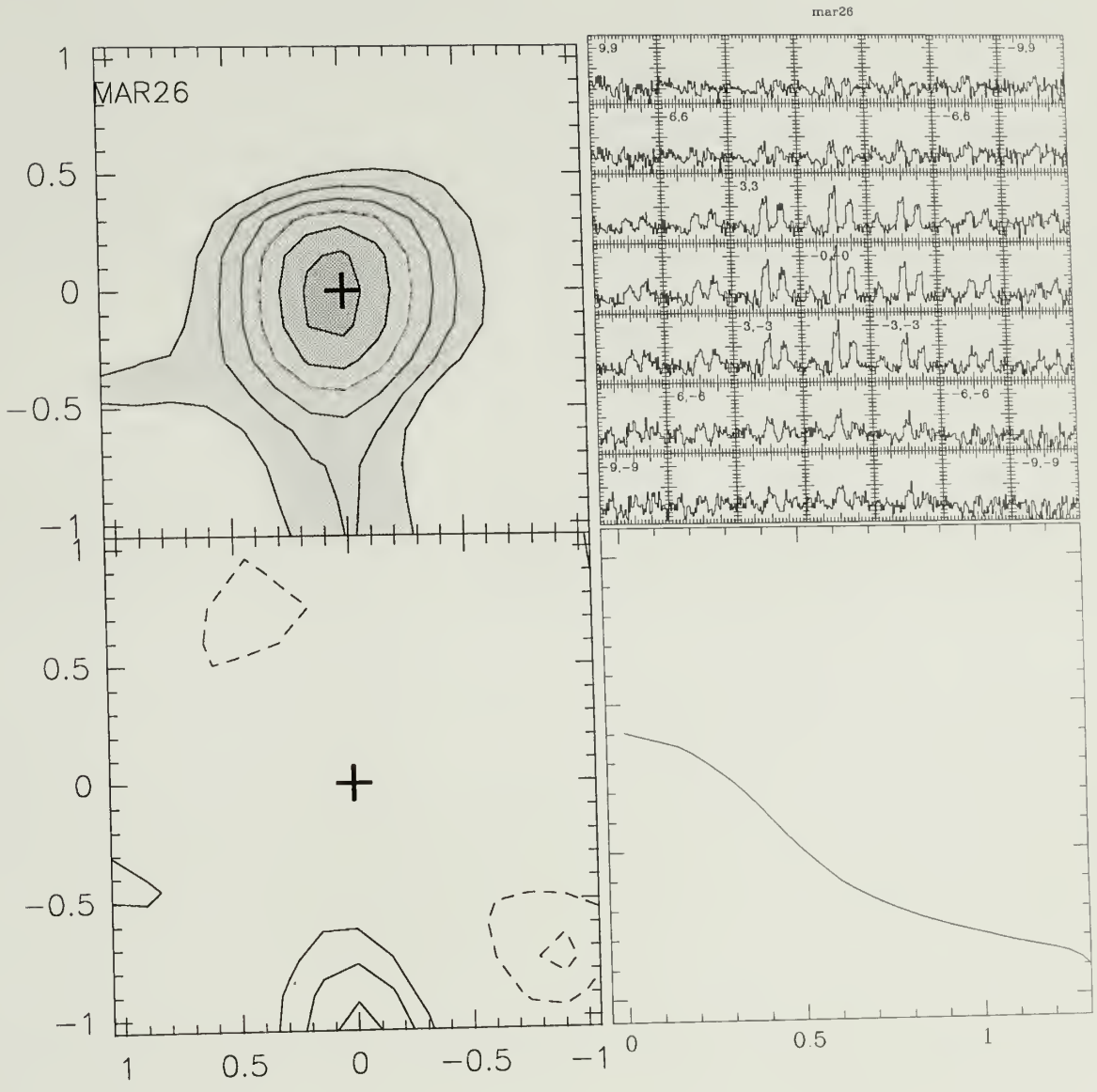

Figure 2.9. HCN mapping data for comet Hyakutake on March 26, 1996, in four representations, as in Figure 2.5.

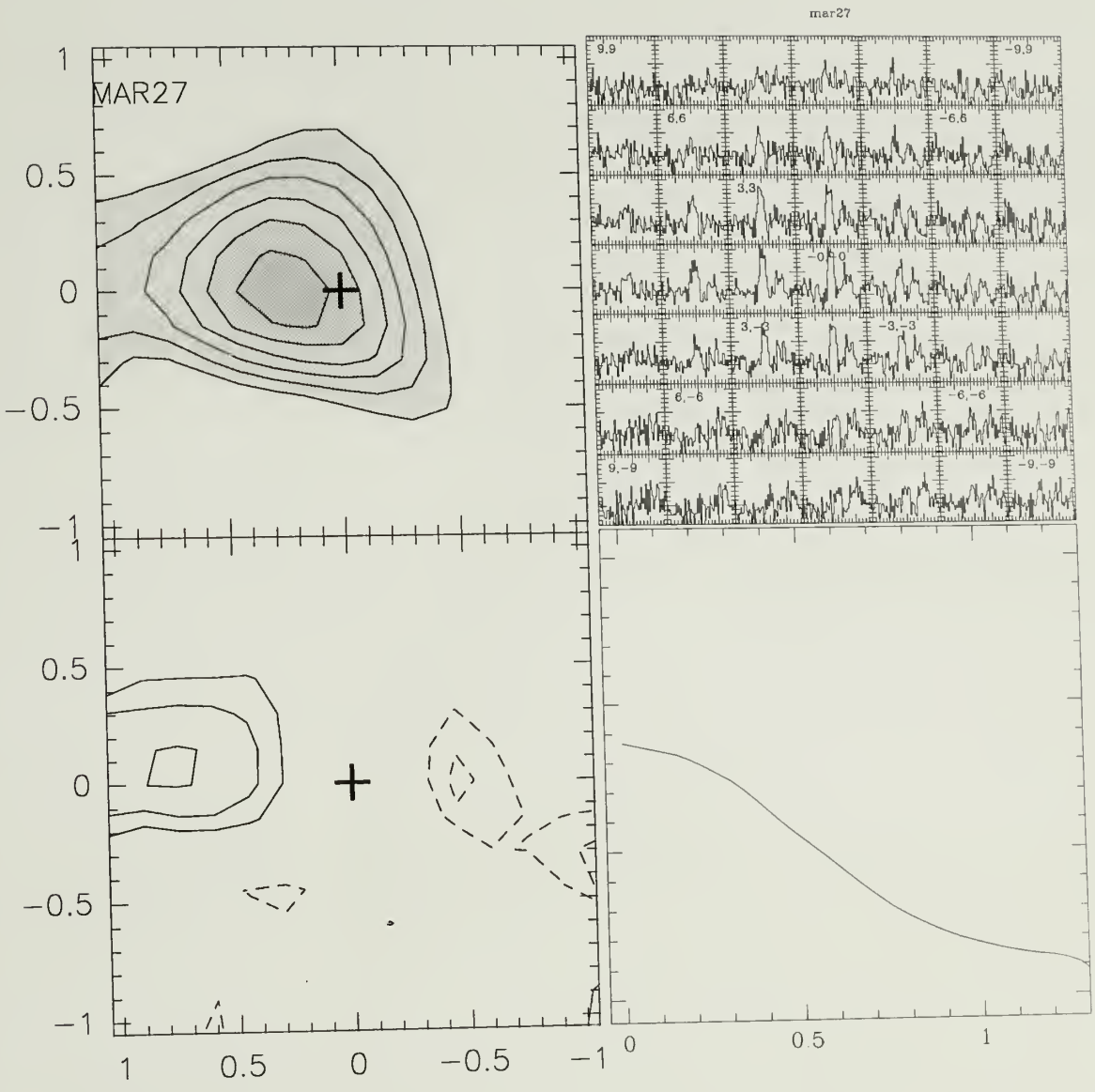

Figure 2.10. HCN mapping data for comet Hyakutake on March 27, 1996, in four representations, as in Figure 2.5.

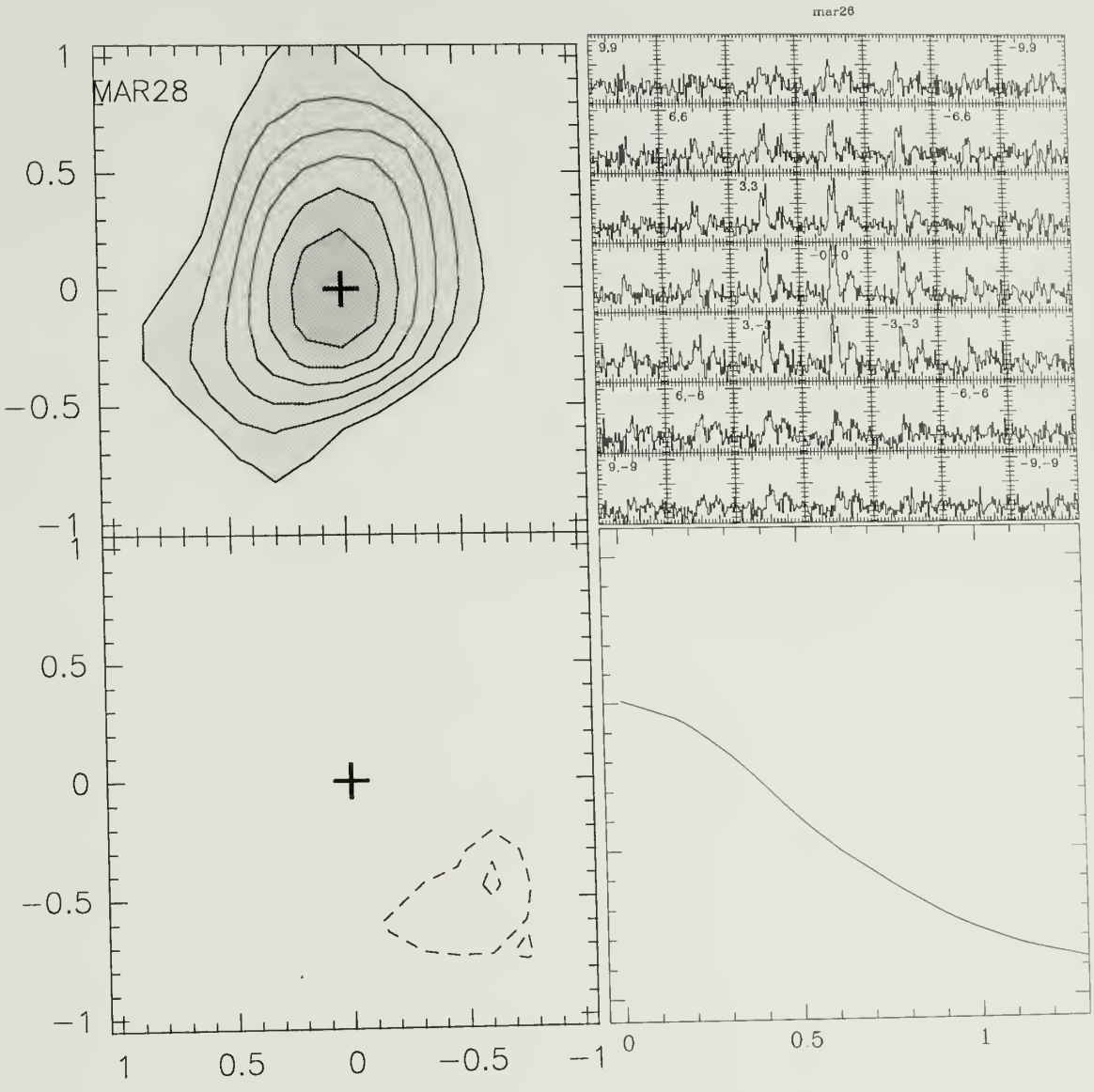

Figure 2.11. HCN mapping data for comet Hyakutake on March 28, 1996, in four representations, as in Figure 2.5.

2.3 Results

2.3.1 Spectral line shapes

HCN spectra for the nucleus position are shown for Figure 2.1 for several observed dates. The F=2-1 and F=1-1 hyperfine components appear, within the noise, in their expected statistical ratio of 5:3, with the F=0-1 component generally lying below the noise level. This consistency with the statistical ratio implies that the J=1-0 transition is optically thin. The spectra taken prior to perigee (March 25, 1996) are quite strong, and display a slight asymmetry in the peak towards the red side of the line. Thereafter, the lines become more symmetric and flat-topped, until March 28, where the line displays two distinctive peaks. These line shapes are present in most observed spectra, regardless of position with respect to the nucleus (as seen in the multiple spectra of Figure 2.5 – 2.11).

Some observed line parameters for the central position of the map are given in Table 2.4. The integrated intensities are computed over the interval from -1.5 km s^{-1} to 1.5 km s^{-1}, after the removal of a constant baseline from the spectra. The median velocity given is the velocity which divides the observed line area equally into two parts. The line width is estimated by dividing the area under the line by its peak value. Throughout this period, the median velocity of the line is slightly blue-shifted, from -0.2 to -0.1 km s^{-1}. The line velocities are plotted in the upper panel of Figure 2.12 versus pre-perihelion heliocentric distance r_h. Such a velocity shift can be understood in terms of enhanced emission on the sunlit side of the nucleus. For values of phase angle (refer to Table 2.3) $\phi_{\rm ph} < 90$, the majority of molecules moving sunward also have an Earth-ward component, so that a sunward enhancement creates a slight bias towards the blue side of the line. The line widths, plotted in the lower panel of Figure 2.12, increase as the comet approaches the Sun. Though the uncertainties in the line width are large, these line widths are consistent with a nominal outflow velocity of 1 km s^{-1} at 1 AU,

Table 2.4. Observed Line parameters for comet Hyakutake

Average Date	Δ AU	r_h AU	ϕ_{ph} deg.	peak mK	$\int$T dv mK $\frac{km}{s}$	$\sigma_{\int Tdv}$ mK $\frac{km}{s}$	Δv $\frac{km}{s}$	$\sigma_{\Delta v}$ $\frac{km}{s}$	$\overline{v}$ $\frac{km}{s}$
1.10 Mar	0.815	1.513	36.9	23	20	7	0.85	0.64	0.00
11.16 Mar	0.482	1.326	38.3	29	38	7	1.31	0.79	0.14
13.80 Mar	0.396	1.275	38.2	14	16	5	1.14	0.92	-0.66
21.32 Mar	0.167	1.125	36.8	154	228	25	1.48	0.58	-0.19
22.28 Mar	0.143	1.105	38.1	135	291	15	2.15	0.55	-0.13
23.17 Mar	0.123	1.086	41.3	169	247	18	1.46	0.37	-0.06
24.17 Mar	0.108	1.065	48.5	145	301	14	2.08	0.48	-0.13
25.19 Mar	0.102	1.044	60.1	85	206	11	2.43	0.75	-0.13
26.96 Mar	0.116	1.007	82.3	90	190	9	2.11	0.47	-0.06
27.87 Mar	0.131	0.989	90.9	77	176	14	2.29	0.99	-0.13
28.83 Mar	0.154	0.967	97.4	88	201	9	2.28	0.54	-0.13
29.68 Mar	0.179	0.947	101.5	55	81	15	1.48	0.95	-0.26
30.44 Mar	0.197	0.933	104.2	53	98	13	1.86	1.03	0.00
31.01 Mar	0.214	0.919	105.8	65	116	11	1.80	0.68	0.00
15.78 Apr	0.715	0.548	104.4	22	23	8	1.07	0.97	-0.26

Notes: Δ is the geocentric distance; r_h is the heliocentric distance; ϕ_{ph} is the phase angle. The peak and integrated intensity $\int$T dv are given for the center position in the map, with the error estimate $\sigma_{\int Tdv}$. Δv is the width of the line, estimated by dividing the integrated intensity by the peak value; $\overline{v}$ is an estimate of the median velocity of the line.

varying as $r_h^{-0.5}$. For comparison, the empirical outflow velocity law of Biver *et al.* (1998), multiplied by two to simulate line width, is also plotted in Figure 2.12.

For optically thin HCN emission, with no additional velocity structure in the coma aside from radial expansion, the expected line shape is double-peaked (*cf.* the line shapes observed in expanding circumstellar shells (Olofsson *et al.* 1982)). In order to account for the observed asymmetric spectral lines, as well as the observed median velocities, there must have been significant motions of HCN molecules in the coma which diverged from constant uniform expansion. Observation distance and phase angle effects alone cannot create the degrees of asymmetry in the observed lines. Gas structure which deviates from the nominal spherical expansion is also supported by the varying degrees of spatial asymmetry which are apparent in the maps (Figures 2.5 —2.11), as discussed below.

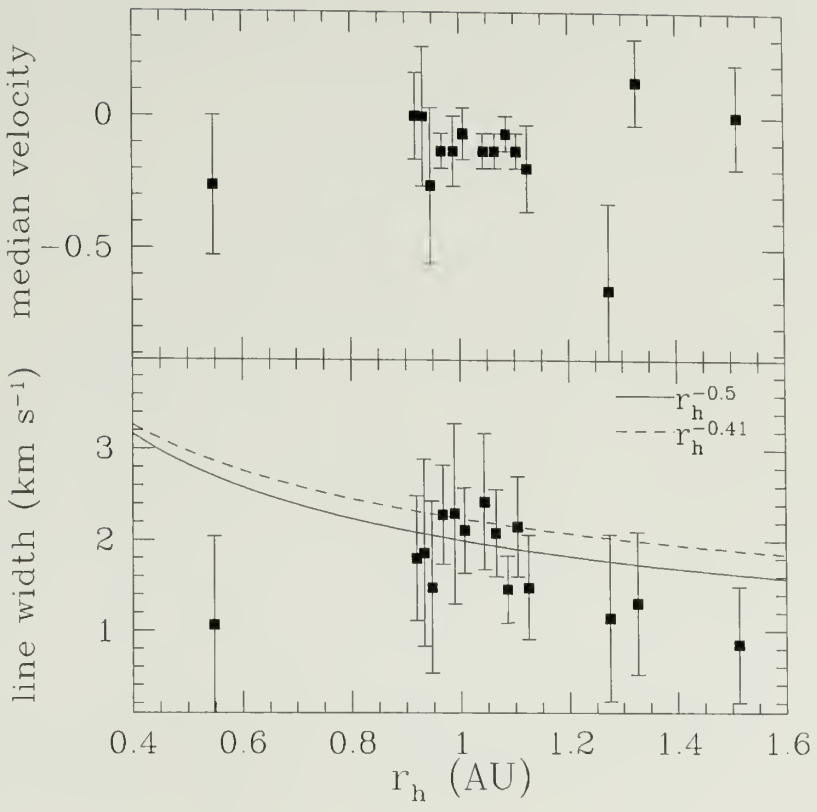

Figure 2.12. Estimates of the median velocity (upper) and line width (lower) versus r_h for comet Hyakutake. Note that most median velocities are blue-shifted by 0.1 – 0.2 km s^{-1}. The line widths are consistent with a nominal $r_h{}^{-0.5}$ power-law (solid curve). A power-law determined by Biver *et al.* (1998) for comet Hale-Bopp is shown for comparison (dashed curve).

2.3.2 Map morphologies

In the maps and spectra of Figures 2.5 – 2.11, it is readily apparent that the HCN emission is detected over an extended area during this time. In general, the line shapes and widths are consistent across the observed coma on a given date. In the intensity maps of Figures 2.5 —2.11, which are all contoured at a consistent interval, it is apparent that the HCN emission is stronger just prior to perigee. Furthermore, there appears to be a stronger degree of asymmetry in the maps for which the spectral lines are most asymmetric. Note the strong residual features (lower left panels) which appear on the pre-perigee dates March 22–24, particularly March 22, and the relatively smooth residual image for March 28, for which the spectra were most similar to those expected from spherically symmetric outflow. Other asymmetries are apparent, but are more difficult to assess on March 23–24, due to a possible discrepancy between the observed and actual position of the nucleus on the sky[2]

2.3.3 Temporal changes

The mapping time influences the detection of coma features in two ways. First, if the mapping time is comparable to or longer than the nuclear rotation period, then we would expect smearing of any features linked to the spin of the nucleus. Second, if the mapping time is longer than the time it takes a molecule to move out of the field of view, then we expect that the "lost" molecules are replenished one or more times during the observation. As outlined in Table 2.3, the number of hours of observation for single-day maps varied from 2.4–12.6 hours. The rotation period of the nucleus of comet Hyakutake is reported to be approximately 6 hours (Schleicher *et al.* 1998). Thus, we expect considerable

[2]Such a discrepancy might be attributed to an error in pointing the telescope, to an incorrect ephemeris epoch, or to a real asymmetry in the coma emission.

smearing of any rotation-induced features. Only if we were privileged with a special observation geometry (such as orthogonal to the rotational pole) could such features appear sharply in our maps. Although a favored observation geometry could occur for a small period of time, such a geometry is clearly impossible in the long-term for comet Hyakutake, given that the trajectory on which it passed the Earth resulted in a wide range of both geocentric distance and phase angle (refer again to Table 2.3). Furthermore, along the line of sight, an individual molecule will continue to be detected until it is destroyed, after about 21 hours (assuming a photodestruction rate of 1.3×10^{-5} s^{-1} for HCN at 1 AU). A molecule leaving the nucleus with a velocity of approximately 1 km s^{-1} (the nominal expansion velocity in the coma) perpendicular to the line of sight will travel outside the field of view in approximately 4–5 hours, comparable to the timescale of many of the maps (refer to hours of observation in Table 2.3). As such, we would expect to see fresh features appearing in the maps every 4–5 hours.

On March 22 and March 28, the observed signal-to-noise ratio was high enough to permit the data to be split and assembled into two independent maps. In addition, the first half of the data on March 26 was similarly excerpted. These dates are of interest because they represent the extremes of spatial symmetry in both the maps and the spectra. For March 22 (upper panels of Figure 2.13), the strong asymmetry which is apparent in the full-average map (upper right of Figure 2.3) appears most strongly in the second half (top right), revealing that this feature is stronger and more transient than it would have appeared from the average map. For March 28 (lower panels of Figure 2.13), the two halves display more asymmetry than does the full-average map (top right 2.4). Such additional asymmetry is not surprising; however, since the two halves likely represent two different populations of molecules. The shape of the lines, however, maintains a great degree of symmetry, though they are lower in signal-to-noise.

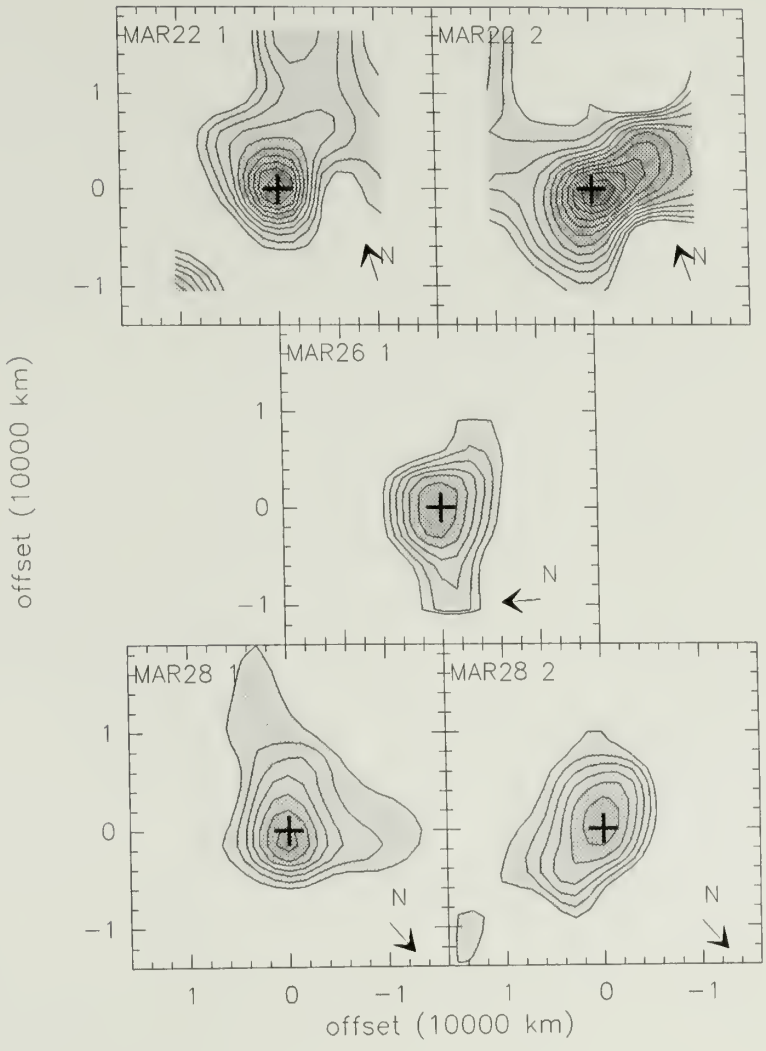

Figure 2.13. Maps of integrated intensity in the HCN J=1-0 line for comet Hyakutake for approximately half-portions of March 22, 26, and 28, 1996. Contour levels begin at 80 mK km s^{-1}, and increase to darker shades in steps of 20 mK km s^{-1}. Symbols and orientation are as in Figure 2.3.

Table 2.5. Upper limits on production rates for other molecules

Observed Molecule	1996 UT Date	Δ (AU)	r (AU)	[1] $3\sigma\sqrt{N}\delta v$ mK km s^{-1}	Q <	% relative to water
CH_3OH	27.49 Mar	0.125	0.995	0.0228	7.2×10^{26}	0.36
HC_3N	28.26 Mar	0.141	0.979	0.0064	9.1×10^{24}	0.00455
CN	25.61 Mar	0.102	1.038	0.0144	5.7×10^{26}	0.285

[1] 3-σ (rms) integrated intensity limit where δv is the velocity resolution, and N is the number of channels integrated into the line. All lines are assumed to span ±1.5 km s^{-1}, and production rates are calculated assuming 50 K LTE. UT Dates given represent the average of the listed times in Table 2.2

2.3.4 Upper limits on undetected species

Upper limits are placed on undetected species by averaging the spectra over a 1 arcminute diameter centered on the comet nucleus position, and calculating the 3-σ uncertainty on the integrated line intensity between ±1.5 km s^{-1} about the nuclear velocity. The computed intensity limits for these molecules are presented in Table 2.5. These abundance limits are generally consistent with those estimated in other comets (Lis *et al.* 1998; Bockelee-Morvan *et al.* 1991; Irvine *et al.* 1984) as well as with limits placed on comet Hyakutake by other observers (Lis *et al.* 1997; Womack, Stern, & Festou 1997).

2.4 Analysis

Spectral line mapping data provide excellent constraints for coma models. Spectra obtained simultaneously over a grid of points not only provide information on the spatial distribution of the emission, but also constrain the velocity structure over the entire observed coma. We have simulated the HCN distribution in the coma of comet Hyakutake using the Monte Carlo model described in Appendix A. The model spectra which result from the simulation provide a means to assess the accuracy of the model in terms of the line width and shape as well as the extent and distribution of emission in the map. Furthermore, the amplitude of the model spectra can be related to the data through the gas production rate of the comet.

We use this model to interpret the types of velocity structures present in the coma of comet Hyakutake, and to estimate the production rate of HCN.

2.4.1 Spherically symmetric model

To illustrate the principles of the model, we first simulate symmetric outgassing of HCN for the observation conditions which existed on 28 March, 1996 (*cf.* Table 2.1). The outflow velocity is assumed to be approximately 1 km s^{-1}at this heliocentric distance. The kinetic temperature in the coma is assumed to be close to the rotational temperature of 75 K, as computed by Lis (1997), from multi-transition observations of HCN, CO, and CH_3OH. The photodestruction rate of HCN at 1 AU is taken to be 1.3×10^{-5} s^{-1} (Crovisier 1994b).

In order to characterize the data, the model must approximate both the shape of the spectral lines and the radial extent of the emission in the map. The upper panel of Figure 2.14 shows the azimuthally averaged data (as discussed in section 2.2.2) along with the model integrated intensity, normalized to the map-center value. The lower panel compares the map-center spectra. As expected for symmetric outgassing, the model emission is azimuthally symmetric, shown by the fact that all the model points at a given cometocentric distance have the same integrated intensity (there is little scatter). The lines reveal a symmetric double-peaked morphology, characteristic of an optically thin expanding shell of gas (Olofsson *et al.* 1982), and the width of the lines is consistent with the observed line width. The model line shapes, however, are peaked too sharply, and the model emission is more extended than that actually observed.

In order to create a more faithful representation of the actual circumstances in the coma, we allow the outflow velocity V_{exp} to vary with cometocentric distance, instead of remaining constant throughout the coma. Such velocity variations were observed directly in comet Halley by the Giotto mass spectrometers (Lammerzahl *et al.* 1987), and have been modeled theoretically by Combi (1989, 1996) and

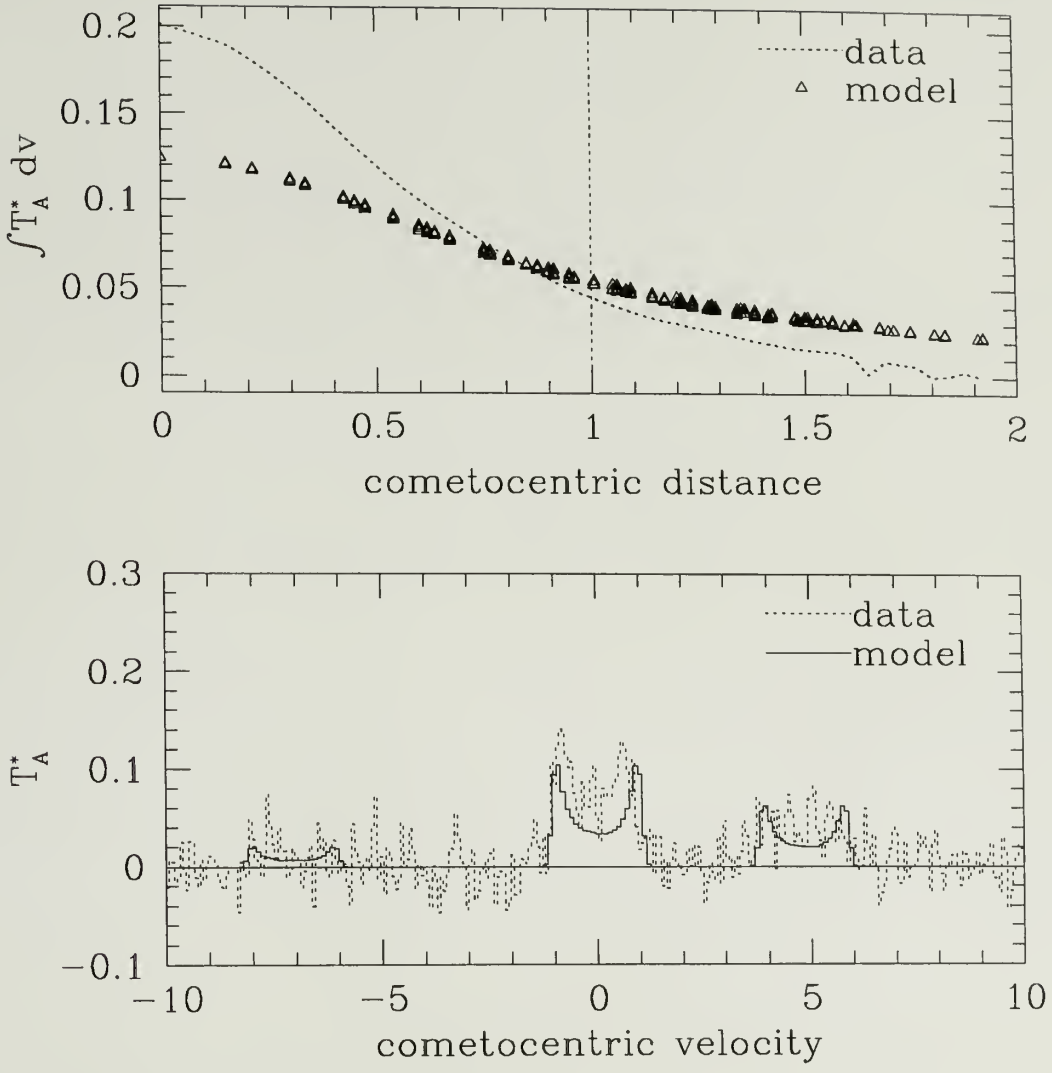

Figure 2.14. Radial profile (upper) and spectrum towards the nucleus (lower) for emission from HCN J=1-0 in comet Hyakutake on March 28, 1996. The cometocentric distance is given in units of 10,000 km, the antenna temperature T_A^* in mK, and the cometocentric velocity in km s^{-1}. Dotted lines are data and solid lines and triangles are model. Here the symmetric model is computed with an transition from collisional to radiative excitation (r_{tran}= 3,700 km) and a constant velocity of 1.0 km s^{-1} throughout the coma.

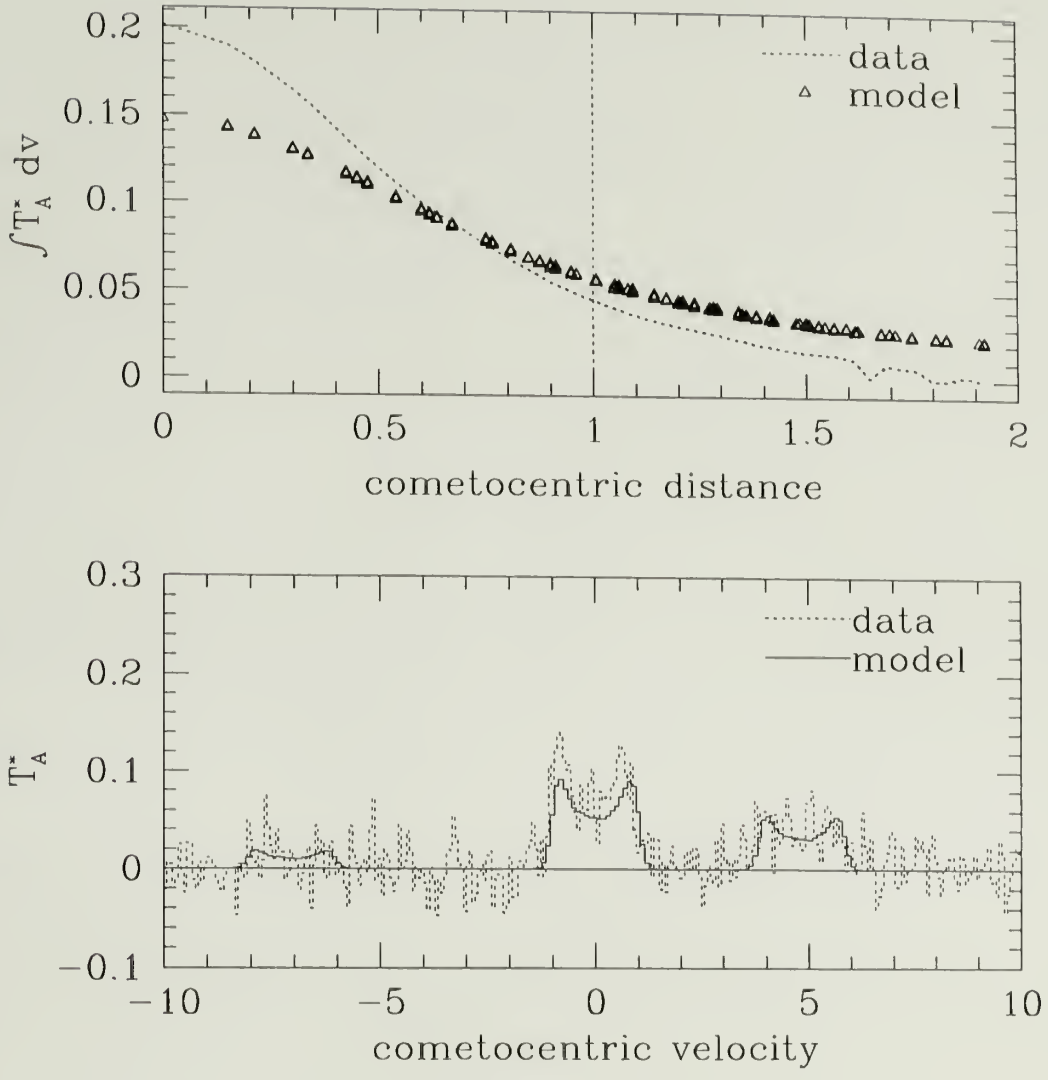

Figure 2.15. Radial profile (upper) and center spectrum (lower) for HCN in comet Hyakutake on March 28, 1996, with power-law outflow velocity. Symbols are as in Figure 2.14. Here the symmetric model is computed with $r_{\rm tran}$= 3,700 km (as described in Appendix B), and a velocity power-law of $V_{exp} = 0.4(r/r_{\rm nucleus})^{0.1}$.

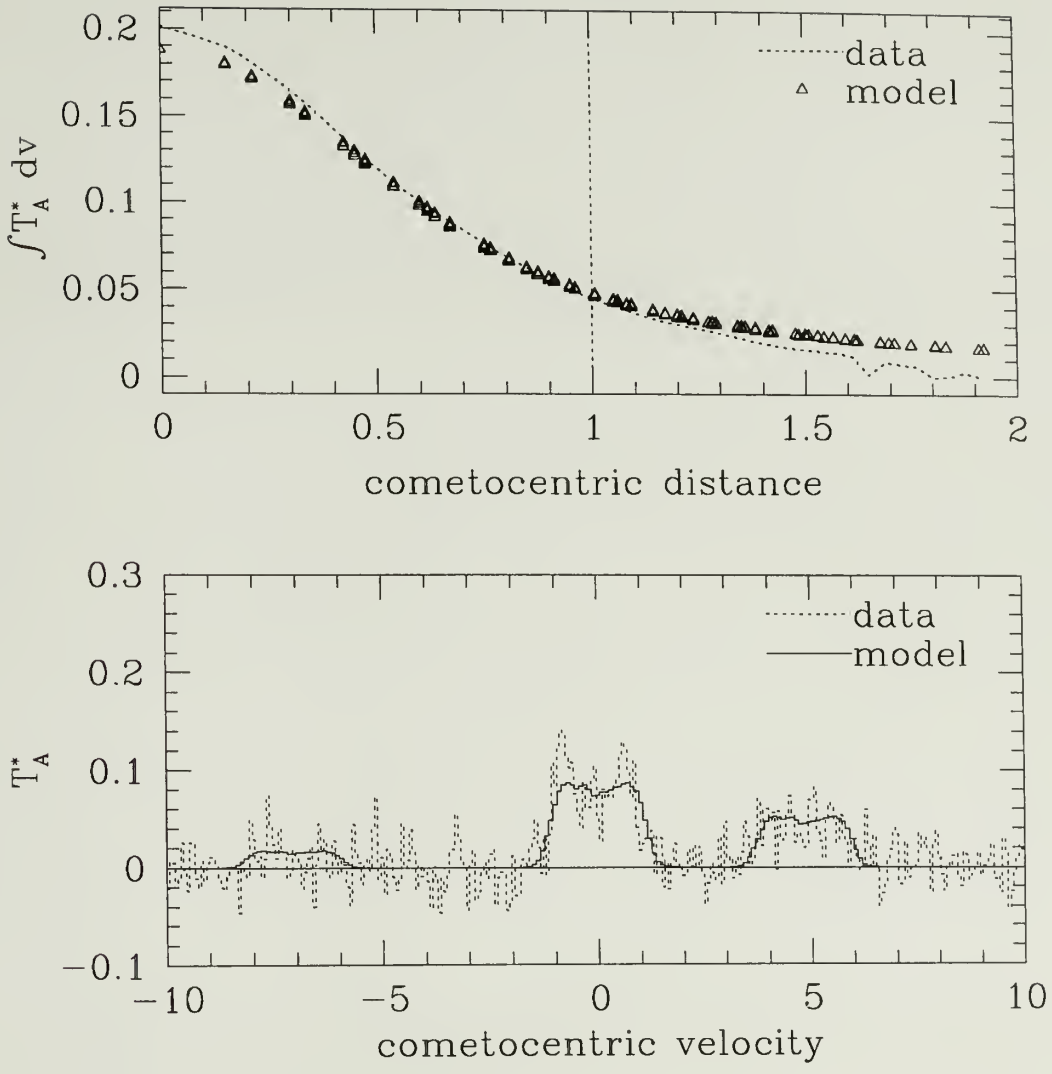

Figure 2.16. Radial profile (upper, in units of 10,000 km) and center spectrum (lower, in units of km s^{-1}) for HCN in comet Hyakutake on March 28, 1996. Symbols are as in Figure 2.14. Here the symmetric model is computed with a constant population in J=1 and a velocity power-law of $V_{exp} = 0.4(r/r_{\rm nucleus})^{0.12}$. The model is scaled by a constant chosen to minimize the value of χ^2 for the model fit, and the radial distribution of the data and model are in good agreement over a large portion of the coma.

others. Following the technique of Ge (1993), we adopt a power-law for the outflow velocity:

$$V_{exp} = V_0 \left(\frac{r}{r_{\text{nucleus}}} \right)^{\alpha}. \tag{2.1}$$

Figure 2.15 illustrates the peak spectrum and radial profile for this model with $V_0 = 0.4$ km s^{-1} and $\alpha = 0.1$. Here, the spectra more closely approximate the observed line shapes, although the model emission is still too extended.

Better agreement in the radial extent of the observed emission is obtained for slightly different excitation conditions. The two-component excitation model described in Appendix B allows for a relatively small upper-state population in the inner collision-dominated region, tending to depress the central emission. If instead we hold the population constant throughout the coma in the simulation, the decrease in emission with cometocentric distance more closely resembles that which is observed. Given that the position of the transition region r_{tran} is not well-defined due to large uncertainties in the collision cross-sections between HCN and H_2O(see discussion in Appendix B; also Bockelée-Morvan *et al.* 1984), it is not unreasonable to consider a constant population in the J=1 state over the observed portions of the coma. Lis *et al.* (1997) suggest that observations of HCN in comet Hyakutake require a value of the H_2O- HCN collision cross-section σ_c (see Appendix B) ten times larger than our adopted value, perhaps even larger (Lis, 1998, personal communication). Thus, we consider the constant-excitation approximation to be a reasonable departure from the parameterization put forth in Appendix B. Figure 2.16 shows a comparison of data and model for this constant-excitation case.

We then apply this constant-excitation approximation to simulations which span a range of parameters, in order to assess the effects of initial velocity V_0 and exponent α on the shapes of the spectral lines. Simulated spectra for the nucleus position are shown in Figures 2.17 and 2.18, with V_0 increasing from 0.2 in the

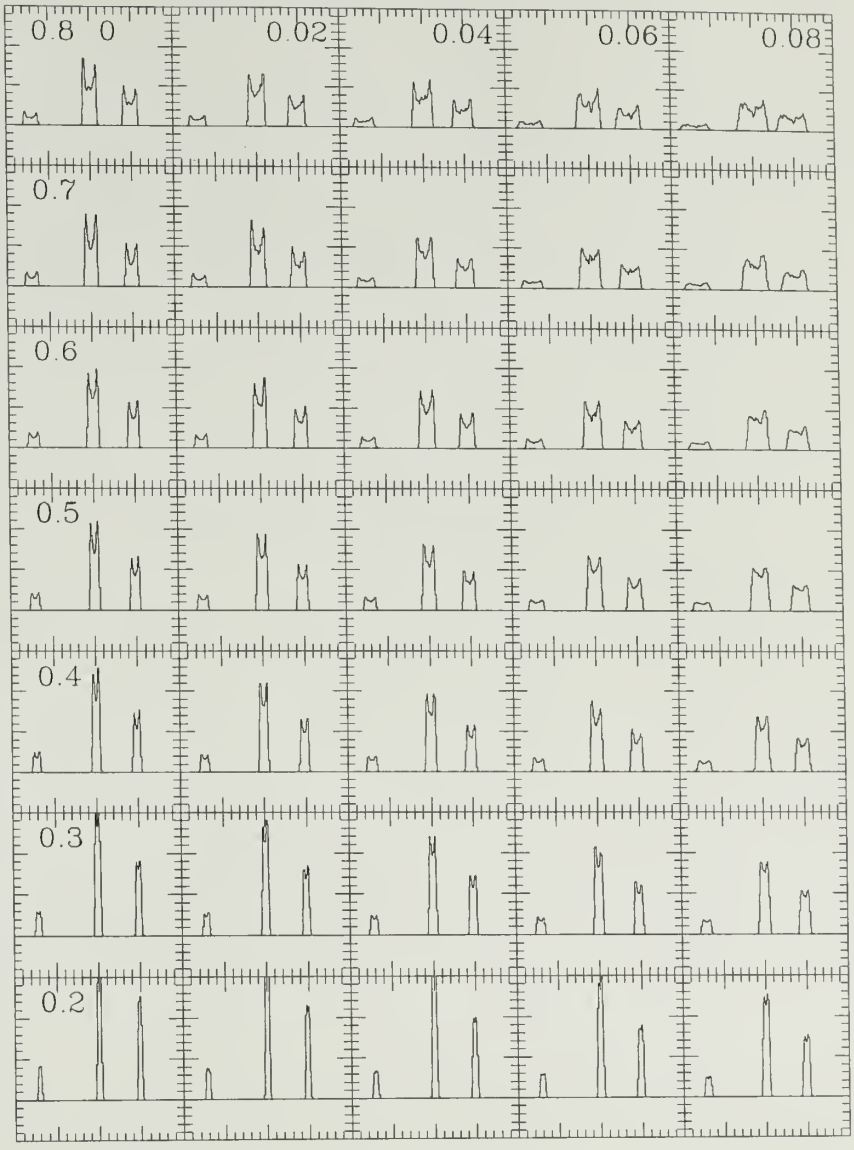

Figure 2.17. A sampling of power-law velocity models for comet Hyakutake for the conditions on March 28, 1996. V_0 is initially 0.2 km s^{-1} in the lower panels, increasing upwards to 0.8 km s^{-1}. α begins at the constant-velocity case on the left, increasing to 0.8 on the right. Note that as the velocity increases, the width of the spectral line increases, as expected. Furthermore, as α increases, the sharp edges of the lines disappear and the double-peaked structure becomes less pronounced.

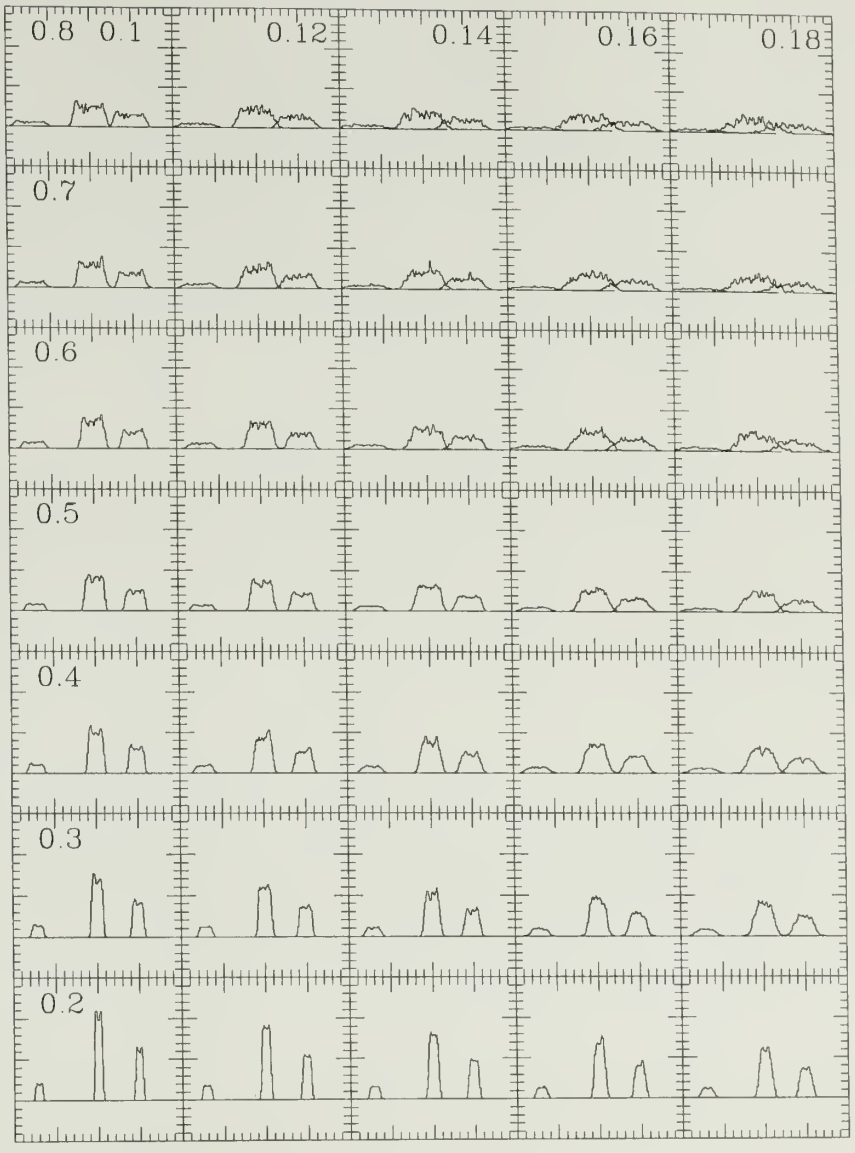

Figure 2.18. A sampling of power-law outflow velocity models of the HCN emission for comet Hyakutake for the conditions on March 28, 1996. V_0 is initially 0.2 km s^{-1} in the lower panels, increasing upwards to 0.8 km s^{-1}. α begins at 1.0 on the left, increasing to 1.8 on the right. Note that in these models, the double-peaked structure is totally absent, and the wings of the lines are progressively less steep as α increases.

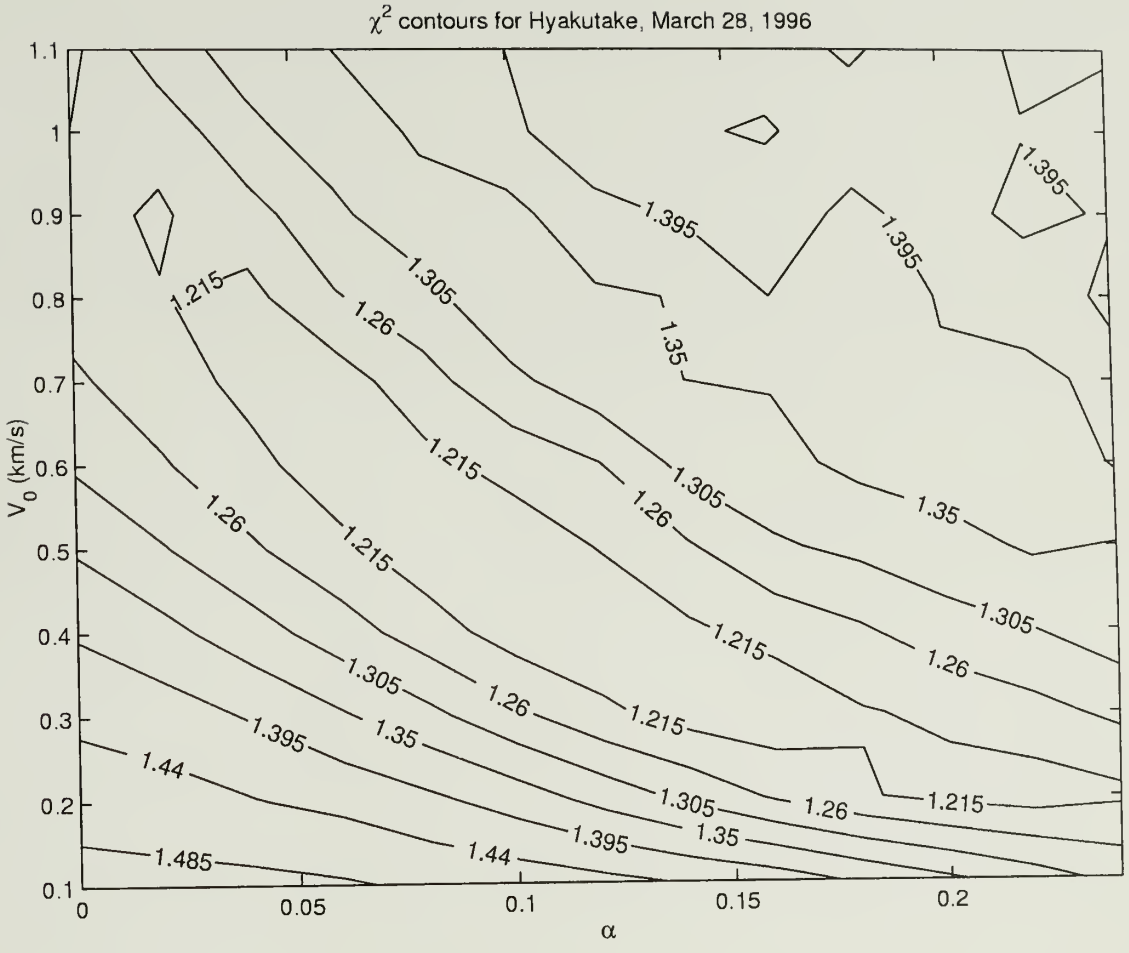

Figure 2.19. Contours of χ^2 for power-law velocity models for comet Hyakutake for the conditions on March 28, 1996. V_0 ranges from 0.1 km s^{-1} to 0.8 km s^{-1}, with α ranging from 0 to to 0.2. Note the elongated minimum in the contours, suggesting that a narrow range of V_0 and α fit equally well.

lower panels, to 0.8 in the upper panels, with α increasing left to right, beginning at the extreme left of Figure 2.17 with the constant-velocity case $\alpha = 0$. To formalize which of these shapes provides the best match to the data, we multiply the model spectrum by a scale factor and compute the residual between this scaled model and the observed spectrum for each channel k. The constant scale factor C is chosen to minimize the value of χ^2 over the detectable coma (indicated by the range of samples $\{i,j\}$:

$$\chi^2 = \sum_i \sum_j \sum_k (C m_{ijk} - d_{ijk})^2. \tag{2.2}$$

Here, the range of spatial samples covers the inner 12,000 km of the coma.

Contours of χ^2 are shown in Figure 2.19, with α increasing along the horizontal axis, and V_0 increasing along the vertical axis. The minimum in χ^2 is elongated, spanning a range of V_0 and α. On-nucleus spectra for the best fits are shown in Figure 2.20. Although each of these models matches the data equally well in a statistical sense, it appears that the larger values of α more closely match the line wings, while smaller values more closely match the two peaks.

Since χ^2 is minimized for the entire detectable coma, the best fits are achieved where both the line shape and the extent of emission are well-fit by the model. The extent of emission is determined by the scale-length L of the molecules: the cometocentric distance reached by the expanding coma during one photodissociation lifetime τ. This scale is given by

$$L = \left(\frac{r_{\text{nucleus}} + V_0 \tau (1 - \alpha)}{r_{\text{nucleus}}^{\alpha}} \right)^{\frac{1}{1-\alpha}}, \tag{2.3}$$

obtained by integrating equation 2.1 from time 0 to time τ, and solving for τ. Figure 2.21 shows these estimates of the scalelength L, plotted versus reduced χ^2, for all the points in the explored parameter range. The pairs of parameters which yield the minimum values of χ^2 fall within a tight cluster of scalelengths, while parameter pairs with larger χ^2 result in scalelengths which are either too large or

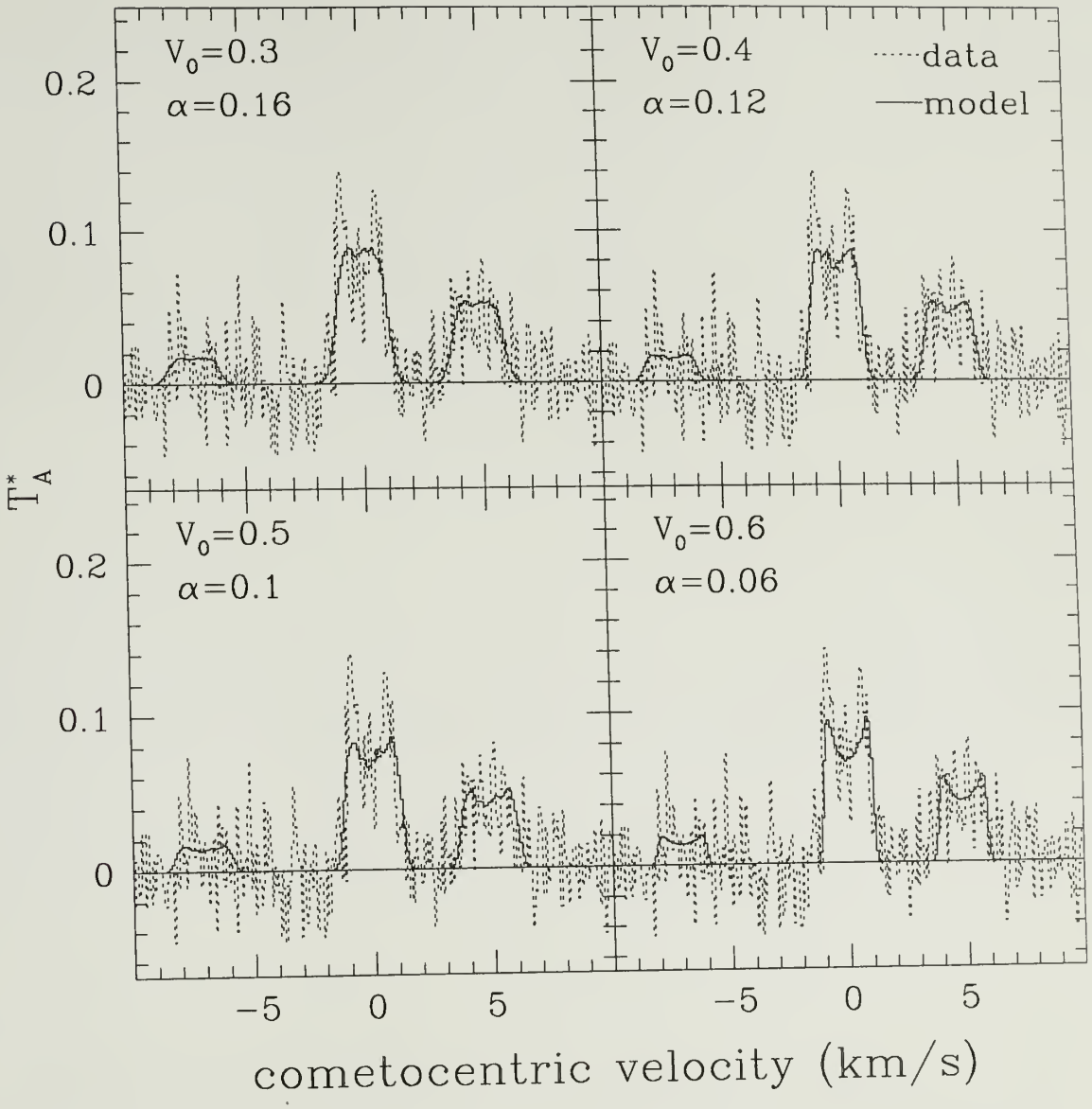

Figure 2.20. A comparison of the on-nucleus observed spectrum (dotted line) with best-fit power-law velocity models (solid line) for comet Hyakutake on March 28, 1996. Note that the lower values of α better reproduce the double-peaked structure, while the higher values better reproduce the line wings. Here we assume a constant J=1 population throughout the coma.

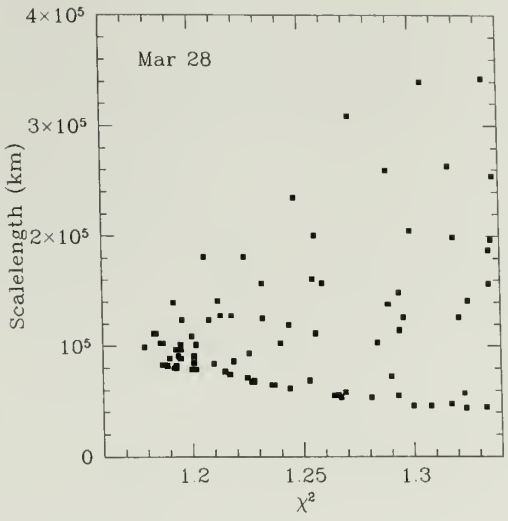

Figure 2.21. The effect of the predicted molecular scalelength on χ^2. Note the tight cluster of points near the minimum in χ^2, and the rapidly diverging scalelengths as χ^2 increases.

too small. These best-fit scalelengths can be converted to a "characteristic velocity" over that scale by dividing by the photodissociation lifetime τ. This velocity must be consistent with the coma outflow velocities, which constrain the width of the spectral lines in the map. Thus, the velocity parameters which yield the minimum χ^2 are those which simultaneously provide the best fit to both the line shape and the molecular scalelength.

2.4.2 Asymmetric model

It is evident from Figures 2.1, 2.3, 2.4, and 2.5–2.11 that some level of asymmetry is present in the coma on most observed dates. Of these, a good signal-to-noise is available for March 22, which displays one of the strongest asymmetries. Figure 2.22 shows the azimuthally symmetric model, using velocity parameters $V_0 = 0.4$ km s^{-1} and $\alpha = 0.12$, as determined above. Here, instead of the azimuthally averaged emission, we plot the individual integrated intensities (top), highlighting those points (filled squares) in the quadrant where the

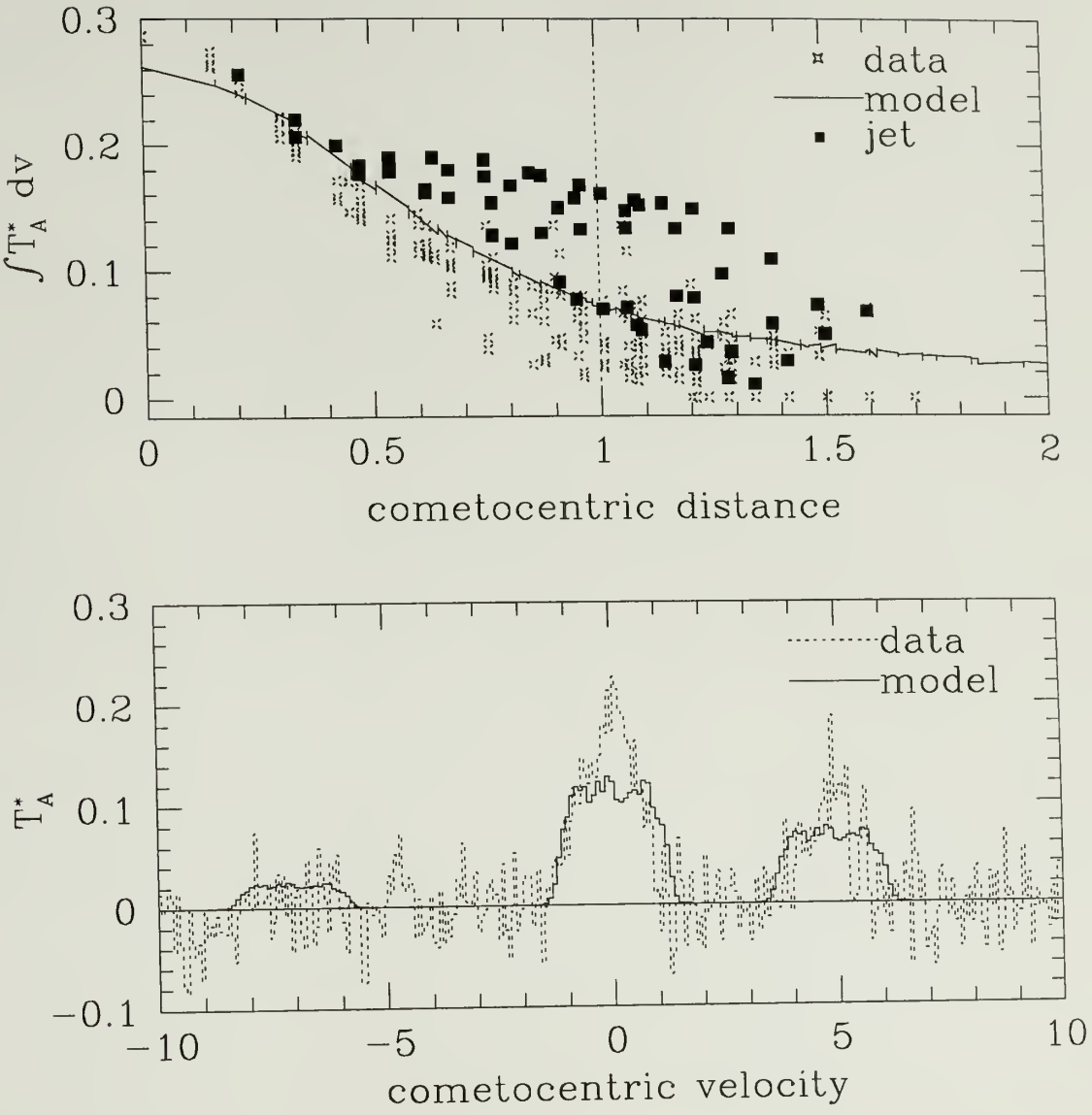

Figure 2.22. Radial distribution (upper) and center spectrum (lower) for comet Hyakutake on March 22, 1996. The cometocentric distance is given in units of 10,000 km, the antenna temperature T_A^* in mK, and the cometocentric velocity in km s^{-1}. Dotted lines are data and solid lines are the model. Here the symmetric model is computed with a constant population in J=1, and a velocity power-law of $0.4(r/r_{\rm nucleus})^{0.12}$. The points in the quadrant where the large asymmetry appears in Figure 2.5 are highlighted as filled squares, to illustrate that the intensities in this quadrant are systematically higher than the average. Also, there is an additional component to the spectrum which protrudes above the model spectrum.

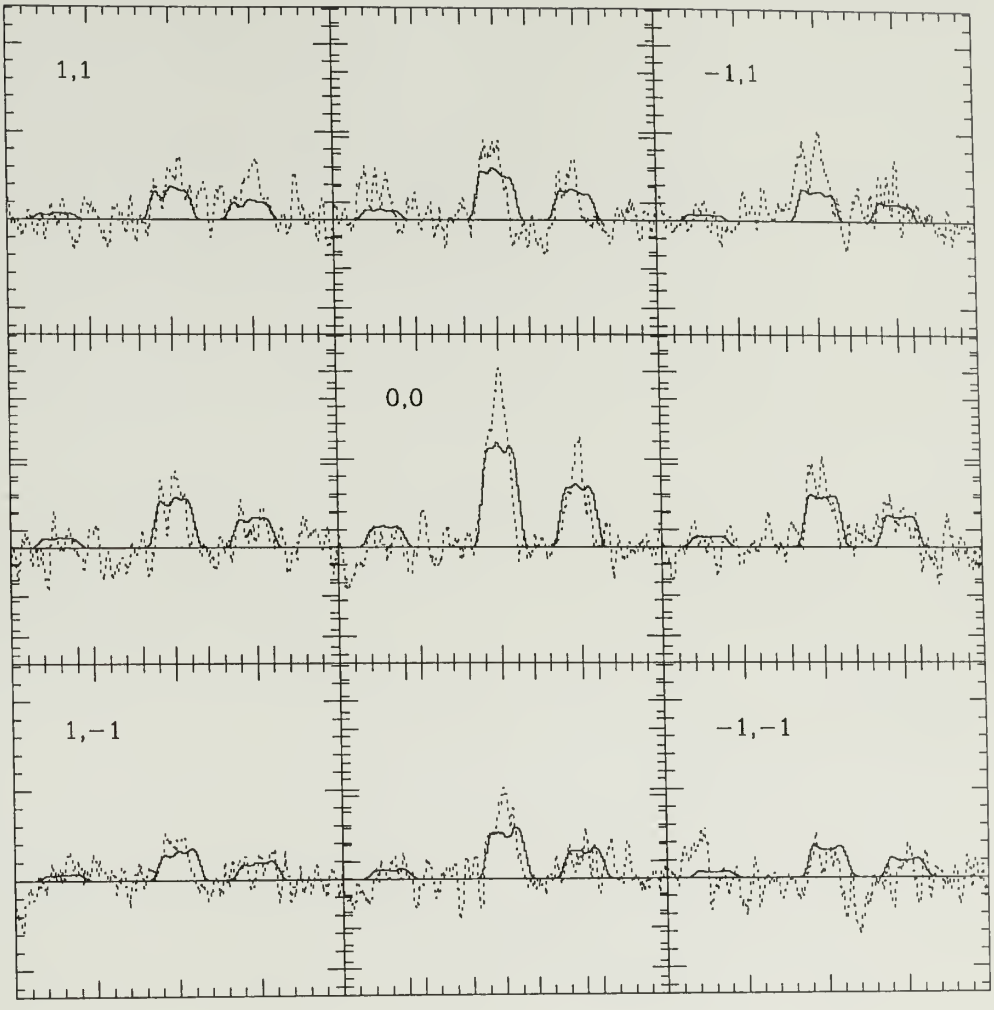

Figure 2.23. A comparison of the on-nucleus observed spectrum for March 22, (center) and other spectra one beam out in the map (as labelled). Superimposed on the data (dotted lines) are the power-law velocity models (solid line) best-fit for comet Hyakutake on March 28 (the symmetric case plotted in Figure 2.20): $V_0 = 0.4$, $\alpha = 0.12$. Although the line shapes fit fairly well in the wings, the models underestimate the observed spectra at the nucleus and in the entire upper-right (-1,1) quadrant. Here we assume a constant J=1 population throughout the coma.

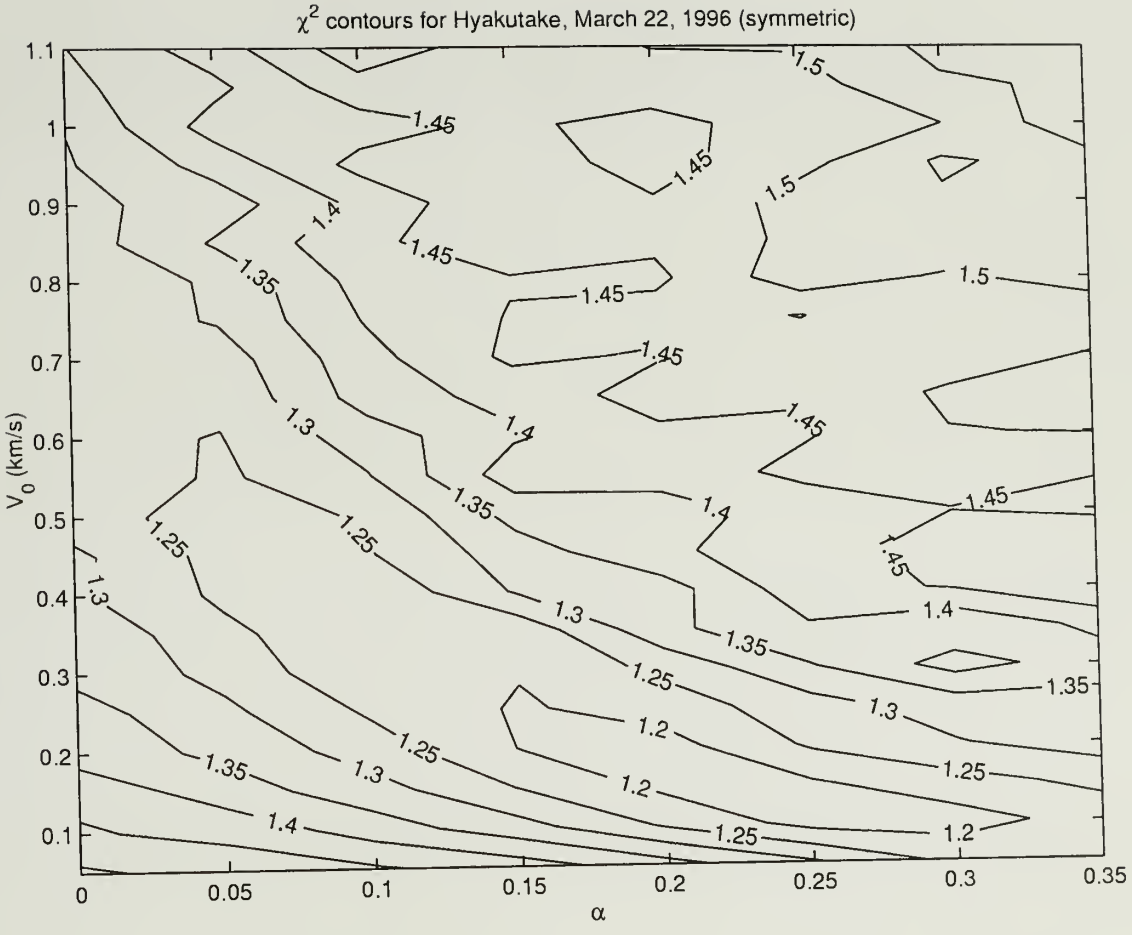

Figure 2.24. Contours of χ^2 for power-law velocity models for comet Hyakutake for the conditions on March 22, 1996. Note the elongated minimum in the contours, which appears to favor small values of V_0 and larger values of α.

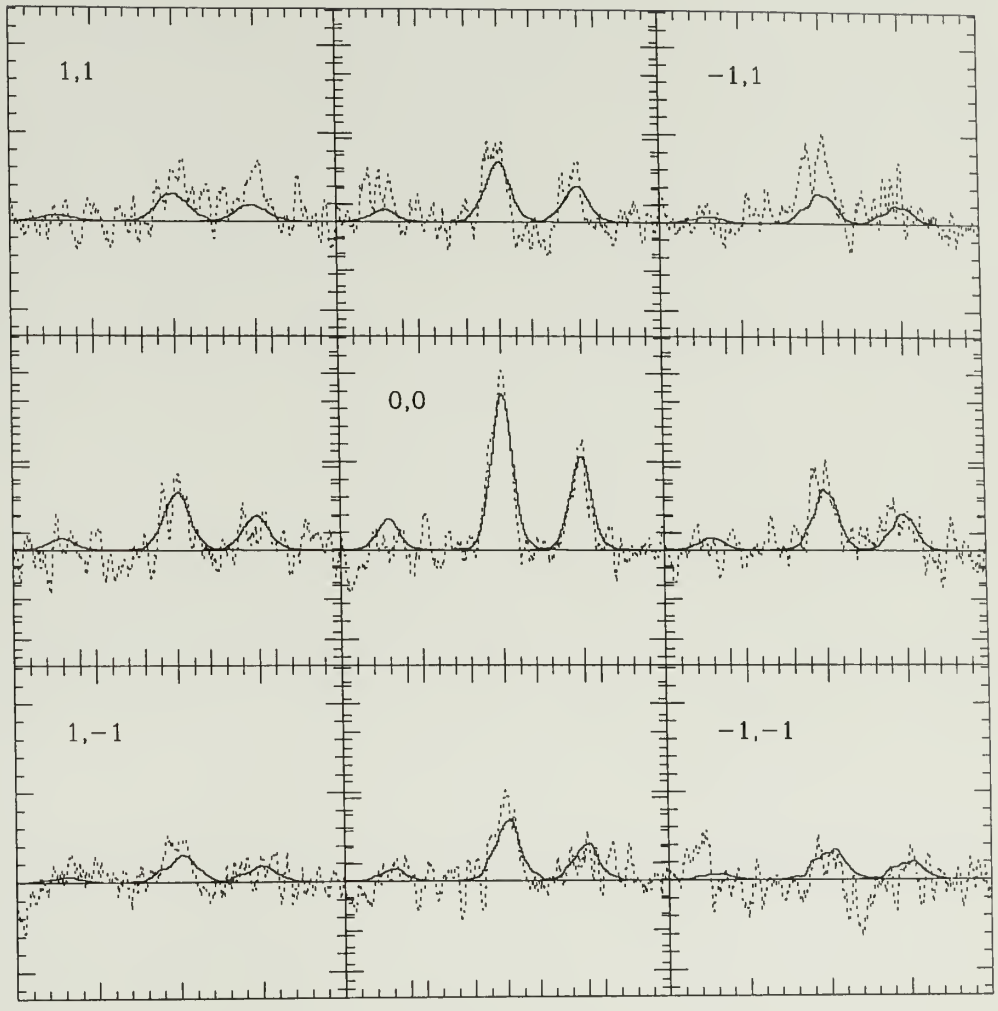

Figure 2.25. A comparison of the on-nucleus observed spectrum (center) and other spectra one beam out in the map (as labelled), for March 22, 1996 in comet Hyakutake. Superimposed on the data (dotted lines) are the power-law velocity models (solid line) best-fit for this date. $V_0 = 0.1$, $\alpha = 0.3$. Although the on-nucleus spectrum approximates the observed fairly well, the models still underestimate the observed spectra in the entire upper-right (-1,1) quadrant.

elongation appears in the data (Figure 2.5). The lower panel is as in Figure 2.16, showing the data (dotted line) and the model (solid line) at the nucleus position. It is clear that the symmetric model with the power-law velocity fails to characterize the data, either in the line shape (lower) or in the distribution of emission (upper), both of which display asymmetries. It is also clear that the observed integrated intensities are systematically higher in the quadrant with the jet (filled squares) than elsewhere (crosses). A grid of spectra for this model is shown in Figure 2.23, comparing the model and data over spectra within one beam of the nucleus position. The model spectra for this choice of $V_0 = 0.4$ km s^{-1} and $\alpha = 0.12$ slightly over-estimate the line width, and significantly underestimate the observed intensity at the nucleus and in the upper-right (-1,1) quadrant.

If, instead of adopting the velocity distribution which matched the data for March 28, we allow the velocity distribution for the two dates to differ, we can solve for new best-fit velocity parameters for March 22. We again investigate a grid of parameters, covering the range $V_0 = 0.05, 1.1$, and $\alpha = 0, 0.35$. In this case, the minimum in χ^2 occurs with $V_0 = 0.1$, $\alpha = 0.3$. The contours of χ^2 are shown in Figure 2.24, and reveal the same "trough" structure as seen in Figure 2.19, shifted to systematically lower initial velocities. In addition, there is a smaller range of better fits with low V_0 and high α: the minimum in χ^2 occurs with $V_0 = 0.1$, $\alpha = 0.3$. Figure 2.26 shows the computed scalelength versus χ^2, as in Figure 2.21. In this case, however, there is a spread in scalelengths, even for the lowest values of χ^2. This can be attributed to the scatter in the intensities at larger cometocentric distances (as seen in the filled squares of Figure 2.22), which cause a range of scale lengths to fit the data equally well. Some parameter pairs will fit the underlying extent of the emission, underestimating the scale in the asymmetry; others will fit the extent of the asymmetry, overestimating the extent of the emission elsewhere in the coma. The comparison of the best-fit model to the data is shown in Figure

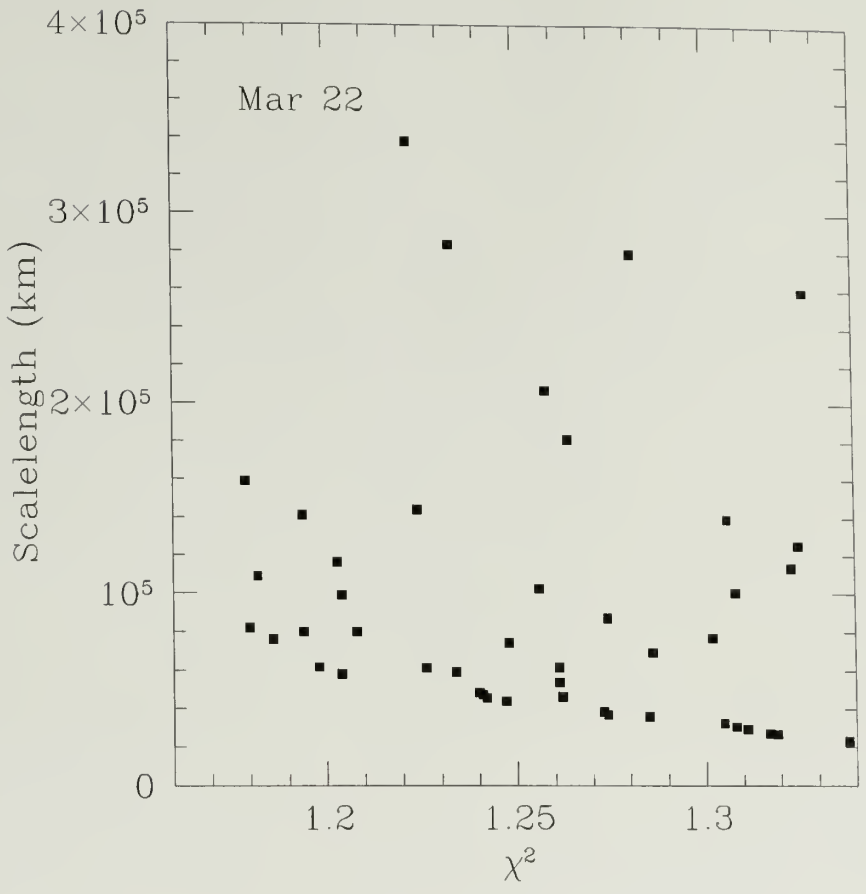

Figure 2.26. The effect of the predicted molecular scalelength on χ^2 for the asymmetric emission of March 22. In contrast to the distribution observed in Figure 2.21, a large range of scalelengths can fit the data equally well, even for small values of χ^2.

2.25, showing a grid of spectra for the nucleus and one beam to either side, with the model superimposed on the data. Although the on-nucleus spectrum is in good agreement with the data, the model at (-1,1) position, which is offset by one beam both above the Sun-comet axis and in the tailward direction, still underestimates the data.

To assess the possibility that asymmetric outgassing could account for the observed map and spectra, we have computed models in which some fraction of the HCN emission is contained in asymmetric "jet" features. The Monte Carlo

program has been modified so that, instead of symmetric outgassing, a given fraction $f_{\rm jet}$ of the total emission is contained in a cone with a half opening angle of γ, to simulate a "jet." The direction of the jet is specified in two angles, with respect to the observer. The azimuthal angle ϕ is measured clockwise from the projected direction to the sun (the positive x-axis of our map). For March 22, we adopt a value of $\phi = 120°$. The second angle, θ is measured away from the line of sight, with $\theta = 0°$ being directly Earthward, and $\theta = 180°$ being anti-Earthward. Since the observed asymmetry in the spectral line of March 22 is slightly redshifted, the feature must be directed away from Earth, and a preliminary investigation of values in the range $90 < \theta < 180$ suggests that the line shapes are best matched for $\theta \sim 165°$.

We explore a range of models, spanning $f_{\rm jet} = 0.05$ to 0.5, and $\gamma = 20°$ to 50°. In this case, we first fix the velocity parameters at $V_0 = 0.4$ and $\alpha = 0.1$, the values which provided the best fit to the spectra which appeared symmetric (section 2.4.1). As seen in Figure 2.27, as the fraction of emission in the jet increases, an additional feature grows atop the spectral line. This asymmetry is sharper for smaller half-opening angles γ, and smoother for larger values. An analysis of the residuals yields a χ^2 estimate as in section 2.4.1, and contours are shown in Figure 2.28. A minimum in χ^2 occurs for a modest 20–30% of emission contained in a cone with a half-opening angle around 30°. This fraction of emission in a small localized region represents a significant enhancement, approximately a factor of 5, over the isotropic emission level.

In order to adapt the model for such asymmetries, a total of six parameters were specified: the original two velocity parameters V_0 and α, plus two directional angles, the cone opening angle γ, and the fraction $f_{\rm jet}$. In this analysis, we have fixed the former four parameters according to reasonable assumptions, and varied only γ and $f_{\rm jet}$. Very likely, a better representation of the data could be achieved

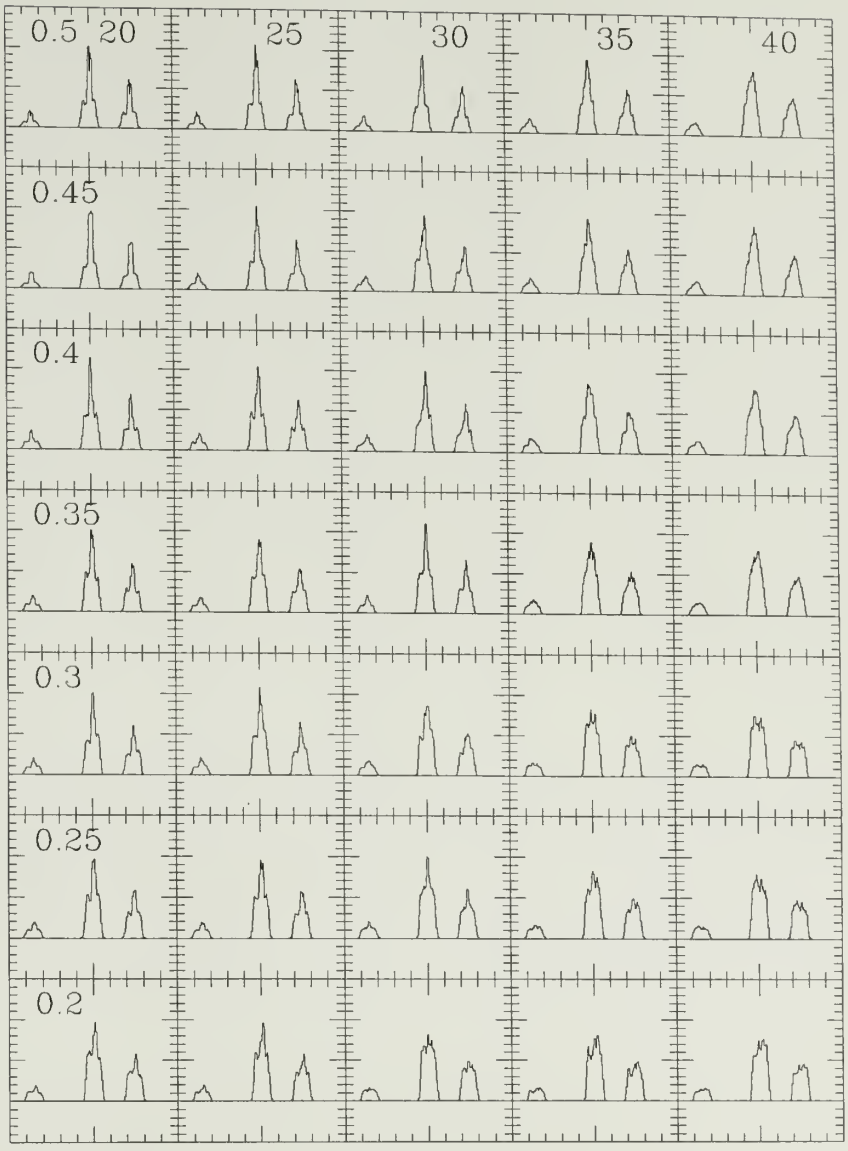

Figure 2.27. A sampling of asymmetric "jet" models for comet Hyakutake for the conditions on March 22, 1996. $f_{\rm jet}$ is initially 0.2 in the lower panels, increasing upwards to 0.5. γ begins at 20° on the left, increasing to 40° on the right. The existence of a jet causes an extra feature atop the smoother distribution from the velocity model. Note that as the opening angle increases, the width of the extra feature increases, and as $f_{\rm jet}$ decreases, it grows less distinctive.

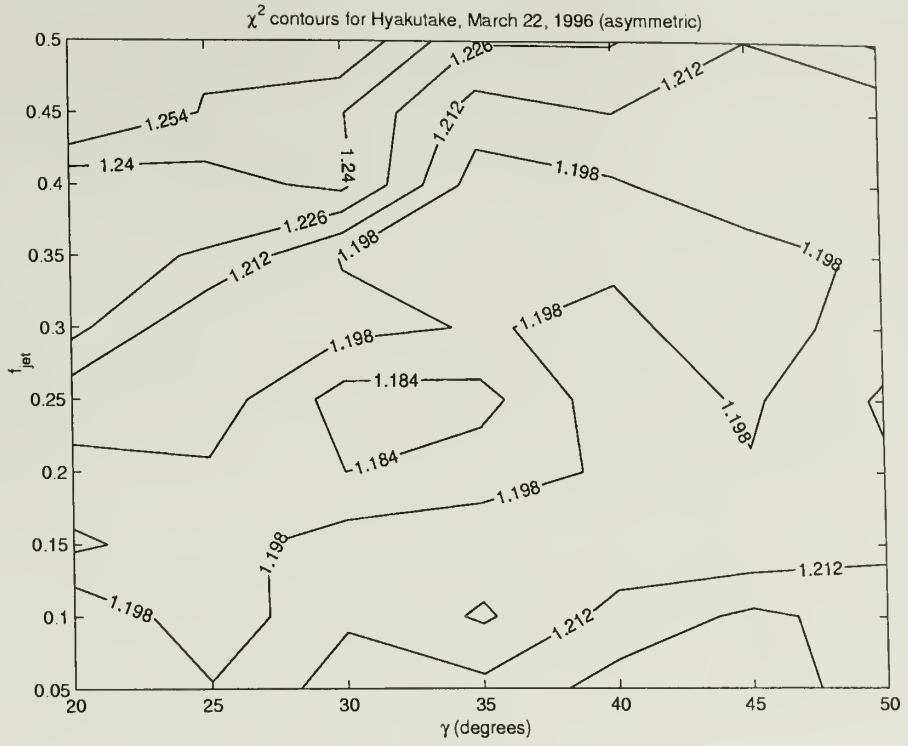

Figure 2.28. Contours of χ^2 for asymmetric "jet" models for comet Hyakutake for the conditions on March 22, 1996. Large values of χ^2 have been truncated for clarity. It can be seen that the best fits to the data occur with opening angles $\gamma \sim 30°$, and a relatively small fraction of emission in the jet $f_{\rm jet} = 0.2$ to 0.3.

by minimizing χ^2 over all parameters. However, given the signal-to-noise ratio of the data set and the computational requirements, we felt that it was sufficient to explore a small range of velocity parameters (from the range of well-fit V_0 and α in the symmetric case of March 28). We found $V_0 = 0.4$, $\alpha = 0.1$ to yield the minimum χ^2, as shown in Table 2.6. A grid of spectra for this best-fit asymmetric model is shown in Figure 2.29.

2.5 Discussion

Since χ^2 is minimized over many spectra in the map, and the asymmetry appears in at most one quadrant, the asymmetric features have a small impact on the total χ^2. This is seen in Table 2.6, where the best-fit symmetric model and the

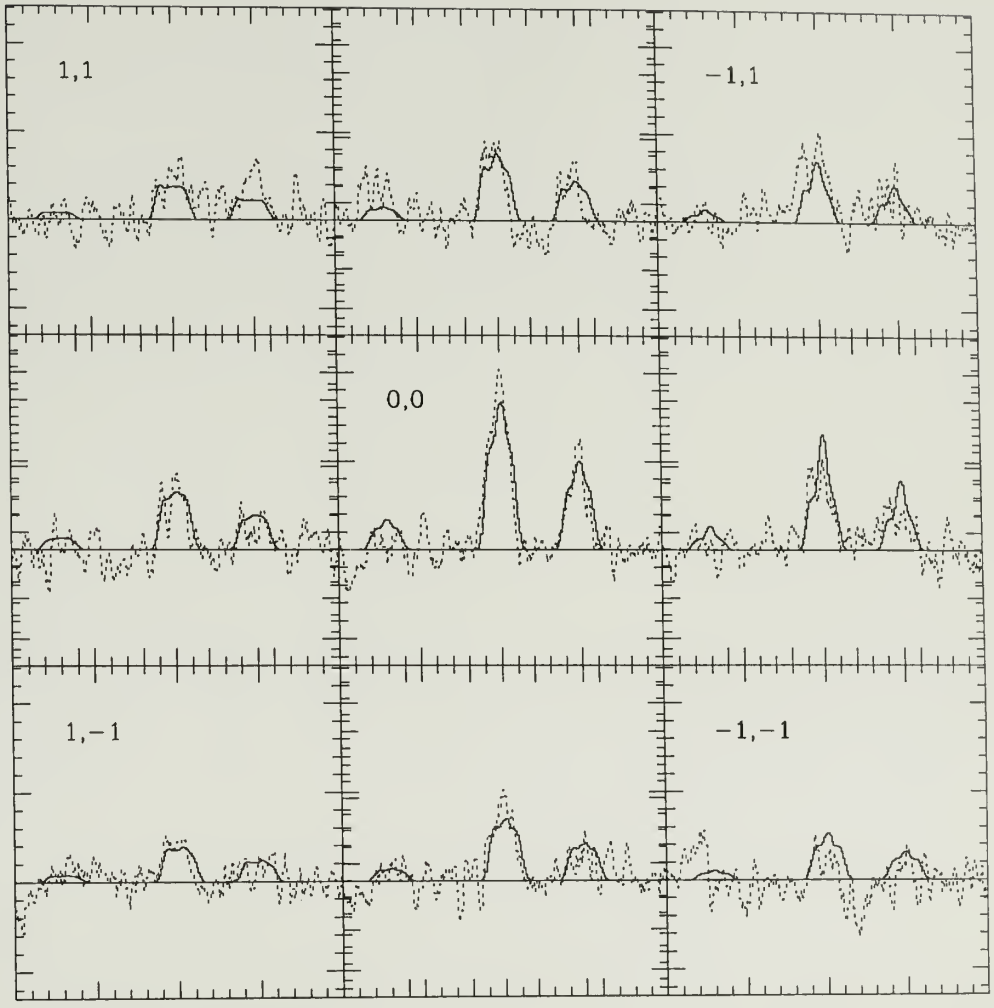

Figure 2.29. A comparison of the on-nucleus observed spectrum for March 22, (center) and other spectra one beam out in the map (as labelled). Superimposed on the data (dotted lines) are the simulated spectra for a model (solid lines) with $V_0 = 0.4$, $\alpha = 0.1$, $\gamma = 25°$ and $f_{\rm jet} = 0.3$.

Table 2.6. Values of the residuals for 4 model parameters

V_0	α	$f_{\rm jet}$	γ	χ^2
0.4	0.12	0.0	0	1.22
0.1	0.30	0.0	0	1.18
0.4	0.1	0.25	30	1.18
0.2	0.15	0.20	50	1.19
0.3	0.16	0.20	25	1.19
0.6	0.05	0.25	30	1.20

best-fit asymmetric model (second and third lines) appear statistically equivalent. However, the relatively large exponent ($\alpha = 0.3$) in the best fit without the asymmetry may exceed the applicability of the power-law approximation to the actual variation in outflow velocity in the coma. At very least, the data of March 22 require significant differences in kinematics from the March 28 case (either a larger distribution of symmetric outflow velocities, or a spatial asymmetry). This result is in agreement with Lis (1997), who suggested that a significant change in the velocity field in the coma occurred around March 24–25.

The notion that a spatial asymmetry was present in the coma on March 22 is corroborated by other observers. Observations of the HCN J=8-7 transition, also on March 22 (Lis *et al.* 1997), revealed even stronger excess emission in the same position in the coma as that reported here. Observations at other wavelengths (Lecacheux *et al.* 1996; Hicks & Fink 1997; Lis *et al.* 1997) also suggest that a change in coma structure and increase in activity occurred during the pre-perigee period March 21–23, and that a small fragmentation of the nucleus likely occurred around March 21.0 (Lecacheux *et al.* 1996; Harris *et al.* 1996; Tozzi *et al.* 1996). Given the unique nature of this event, improvements to the model might be made in three ways. First, instead of a continuously emitting jet along a given direction, the possibility of a one-time outburst should be considered. Second, the outflow velocity within the jet region may not be the same as in the rest of the coma, and

the possibility of a "pile-up" due to slower outflow should be considered, although the need for this is mitigated by the time-averaged nature of our mapping data. Third, a local change in gas density could affect the excitation of the HCN J=1 state in that portion of the coma, enhancing the observed asymmetry. Each of these possibilities still begins with our basic conclusion that there was likely a spatial asymmetry present in the coma of comet Hyakutake on March 22, 1996, with perhaps a factor of 5 local enhancement over the predicted isotropic level of HCN J=1-0 emission.

Finally, in order to analyze the data over the range of heliocentric distance observed, we must compute a total HCN production rate for each observation. This computation requires some assumptions on the distribution of the gas within the coma. In our mapping data, however, we have observed the projected spatial distribution of HCN, which can be used as a constraint in the model. As shown above, this constraint suggests that a constant population in the J=1 state characterizes the data better than the two-component distribution of collisional and radiative excitation outlined in Appendix B. Thus, we compute the production rates Q using a constant population in J=1. However, as shown in Figure B.4, less than 10% of the HCN is in the J=1 state in the collision-dominated region of the coma at these temperatures (approximately 75 K, (Lis *et al.* 1997)). The J=1 population in the radiation-dominated portion of the coma is predicted to be 40–50%, nearly a factor of 5 greater than in the collision-dominated limit. As such, accurate computation of the production rate will strongly depend upon which limit we choose for the overall HCN population distribution. Since it has been suggested that the collision-dominated region is quite large (Lis *et al.* 1997), by a factor of 3 or more over our assumed value of r_{tran}, we adopt the thermal population at 75 K.

We use the spherically symmetric constant velocity distribution to model the spatial distribution of HCN, as outlined in section A.4 of Appendix A. Although

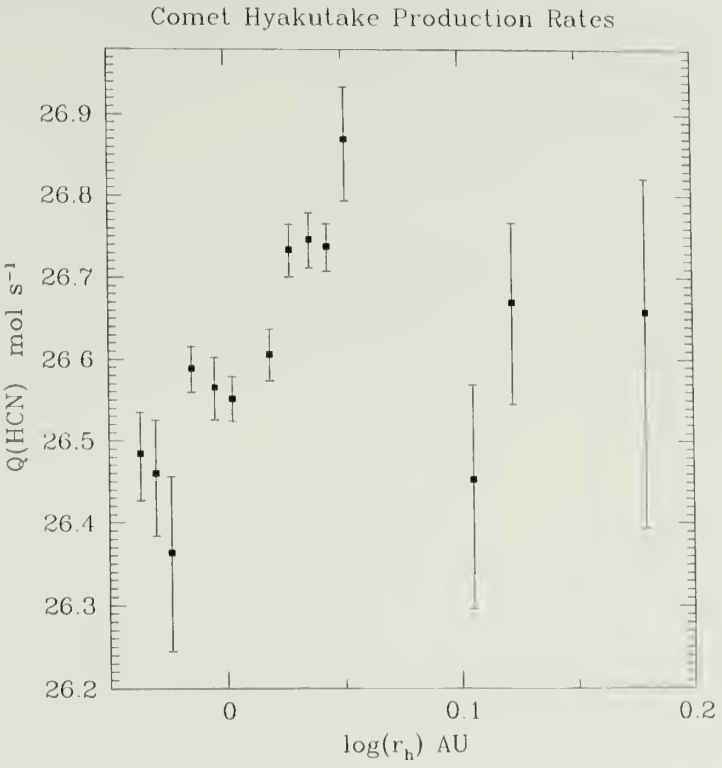

Figure 2.30. Production rates for HCN in comet Hyakutake versus r_h. Despite the fact that the heliocentric distance decreased throughout the observation period, and the production rate might be expected to exhibit an overall increase, a noticeable decrease in production rate occurred for points near r_h=1 AU.

this model does not accurately reflect the observed line shapes, the integrated line intensity is relatively insensitive to the velocity model. Thus, we choose the simplest (constant) velocity in the production rate computation. The resulting production rates for comet Hyakutake are shown in Table 2.7, and plotted versus r_h in Figure 2.30. Using the H_2O production rates of Hicks & Fink (1997), we derive an approximate abundance of 0.2% relative to water. A relative abundance of HCN/H_2O of 0.2% is typical of that reported by others for this comet (Lis *et al.* 1997).

All HCN detections were made pre-perihelion, so the heliocentric distance was monotonically decreasing and the production rate would be expected to increase during this time. Nonetheless, there is a general decrease in the production rate over the near-perigee observation period. This is in agreement with the trend observed by Lis (Lis *et al.* 1997), who reported a 50% decrease in production rate between March 22.5 and March 23.5. Although the overall water production rate in comet Hyakutake is reported to depend on $r_h{}^{-1.5}$ (Hicks & Fink 1997), individual observations, as well as those of other observers (Lecacheux *et al.* 1996; Gérard *et al.* 1997; Lis *et al.* 1997) reveal a brightening in the comet around March 21, either related to or as a cause of the morphology changes discussed above. Thus, the observed departure from the overall trend in gas production is not surprising.

2.6 Conclusions

We have observed emission from the J=1-0 rotational transition of HCN in comet Hyakutake, and created spatially-resolved coma maps for a 10-day portion of the 1996 apparition. Both the individual spectral lines and the emission maps display varying degrees of symmetry over the observation period. The line shape varies from an asymmetric, single peak, to a flat-topped, square profile or a double-peaked "horned" shape. During the same time, the emission maps reveal

Table 2.7. Production rates for comet Hyakutake in 1996

UT date 1996	Δ (AU)	r (AU)	Q (mol/s)	σ_Q (mol/s)	log(Q)
01mar	0.815	1.513	4.55e+26	2.07e+26	26.66
11mar	0.482	1.326	4.68e+26	1.17e+26	26.67
14mar	0.396	1.275	2.84e+26	8.67e+25	26.45
21mar	0.167	1.125	7.40e+26	1.18e+26	26.87
22mar	0.143	1.105	5.46e+26	3.64e+25	26.74
23mar	0.123	1.086	5.57e+26	4.27e+25	26.75
24mar	0.108	1.065	5.42e+26	3.96e+25	26.73
25mar	0.102	1.044	4.04e+26	2.93e+25	26.61
26mar	0.116	1.006	3.56e+26	2.23e+25	26.55
27mar	0.131	0.989	3.68e+26	3.25e+25	26.57
28mar	0.154	0.967	3.88e+26	2.50e+25	26.59
29mar	0.179	0.947	2.31e+26	5.50e+25	26.36
30mar	0.197	0.933	2.89e+26	4.66e+25	26.46
31mar	0.214	0.919	3.05e+26	3.78e+25	26.48
16apr	0.715	0.548	4.21e+26	1.95e+26	26.62

Production rates calculated as in Appendix A, assuming a collision-dominated population at 75 K. σ_Q is an estimate of the uncertainty in the model fit, including the data uncertainties.

initially strong, asymmetric HCN emission, which evolves to weaker, more symmetric distributions.

On most dates, at least some degree of real asymmetry was observed in both the coma maps and the grid spectra. We find that a constant outflow velocity does not accurately reflect the observed velocity structures in the lines, nor does a simple two-component approximation to the excitation in the coma. Simulations which allow for a constant population in the J=1 level, for the outflow velocity to vary as a power-law with cometocentric distance, and for some fraction of the emission to be contained in localized "jet" features can account for some of the features seen in the data.

The observed gas production rates show a slight decrease during the observed time interval, in contrast to the longer-term overall trend versus heliocentric distance. This is consistent with the observed increase in activity of the nucleus,

which likely led to a nuclear splitting event (Lis *et al.* 1997). Our observations on March 22, 1996, shortly after the reported nuclear splitting, suggest that regions on the nucleus experienced enhanced production above the nominal isotropic outgassing. A good representation of the data is achieved with a model wherein a significant ($\sim$ factor of 5) enhancement in the emission occurred within a $\sim 30^{\circ}$ cone, in a direction facing away from both the Earth and the Sun.

Chapter 3

Molecular Mapping of Hydrogen Cyanide in Comet Hale-Bopp

3.1 Introduction

Comet C/1995 O1 was discovered independently by Alan Hale and Thomas Bopp on July 25, 1995, while it was 7 AU from the Sun and still more than 6 AU from Earth. This discovery provided an opportunity to plan and execute a wide variety of observations over a long period of time, a luxury which is rarely afforded to comet observers. Comet Hale-Bopp passed 1.3 AU from the Earth at perigee on March 23, 1997, almost exactly a year after the spectacular apparition of comet Hyakutake. Only nine days later, it reached perihelion at 0.91 AU from the Sun on April 1, 1997. The comet, with a large nuclear size of 30–40 km (Weaver *et al.* 1997; Fernández *et al.* 1998) was extremely active, even at large heliocentric distances. At perihelion, the total gas production rate is reported to have been 1 $\times 10^{31}$ molecules s^{-1} (Biver *et al.* 1998, and references therein), more than an order of magnitude more than either comet Halley or comet Hyakutake.

In this chapter, we present the observations and analysis of HCN mapping of comet Hale-Bopp carried out at FCRAO. As discussed in chapter 2, repeated mapping of the molecule HCN provides a record of the gas production and kinematics in the coma of the comet over time. The result of such observations is a better understanding of the processes at work in the coma, and how these evolve with time. Due to the early discovery of comet Hale-Bopp, we were able to plan observations and map the HCN J=1-0 transition over 9 months, between October, 1996, and June, 1997. We first detected HCN emission at a pre-perihelion

geocentric distance of 3 AU, corresponding to a heliocentric distance $r_h = 2.8$ AU, and continued to detect it post-perihelion to a distance of $r_h = 1.5$ AU.

3.2 Observations

The J=1-0 rotational transition of HCN at 88.63185 GHz was observed in comet Hale-Bopp, using the QUARRY array receiver (Erickson *et al.* 1992) on the FCRAO 14-m telescope, in a similar manner to that described in section 2.2 for comet Hyakutake. The 20 MHz correlator bandwidth was used, resulting in 0.066 km s^{-1} spacing in the velocity channels. Spectra were obtained by frequency-switching with an offset of 6.0 MHz. Half-beam (Nyquist) sampled maps were made for all HCN observations. At larger heliocentric distances ($r_h > 1.5$), several adjacent days of observations are combined into a single map, in order to improve the signal-to-noise ratio. All HCN observations are summarized in Table 3.1, referenced by the averaged UT date for each map. Also given in Table 3.1 are the geocentric and heliocentric distances (Δ and r_h), the phase angle of the comet ($\phi_{\rm ph}$), and the total number of hours integrated into each map.

In order to maintain a fixed reference in comet coordinates, the array receiver was rotated to follow the position angle of the Sun-comet axis on the sky, as reported in the ephemeris of D. Yeomans (JPL WWW site). This rotation angle was computed automatically by the ephemeris tracking program at the telescope to align the 5-pixel rows (Figure 1.1) of the array with the projected tail vector of the comet on the sky. The mapping errors which were discovered during our observations of comet Hyakutake were corrected before this observing campaign.

In order to interpret the maps on the physical scale of the comet, the raw spectra from each observed position were convolved with a Gaussian function and re-sampled, as described in section 2.2.2. The Hale-Bopp HCN data are divided into three groups, according to the geocentric distance Δ and the signal-to-noise ratio in the spectra. The first grouping is of pre-perihelion data with $\Delta \geq 2$ AU.

Table 3.1. Log of HCN J=1–0 observations for comet Hale-Bopp

UT Date	Δ (AU)	r_h (AU)	$\phi_{\rm ph}$ (deg)	$t_{\rm int}$ (hrs)	(km) eff. beam ($''$)	
Oct 07.38	3.011	2.812	19.4	12.67	239,000	110
Oct 26.82	3.053	2.579	17.9	29.12	240,000	109
Nov 04.84	3.048	2.469	16.9	16.03	240,000	109
Nov 13.27	3.026	2.365	15.8	13.14	240,000	109
Nov 24.20	2.973	2.230	14.5	12.94	238,000	110
Nov 30.54	2.929	2.150	13.9	13.16	237,000	112
Dec 23.29	2.687	1.863	13.8	8.69	232,000	119
Jan 03.20	2.528	1.725	15.6	13.98	229,000	124
Jan 13.22	2.359	1.599	18.5	15.34	225,000	131
Jan 24.46	2.151	1.459	22.8	9.84	221,000	141
Feb 02.66	1.972	1.348	27.1	8.46	218,000	151
Mar 11.61	1.363	0.985	46.7	8.14	84,500	85
Mar 20.55	1.317	0.937	49.0	5.94	83,000	87
Mar 24.72	1.317	0.924	49.1	10.48	83,000	87
Mar 30.78	1.342	0.914	48.1	9.41	83,600	86
Apr 03.81	1.374	0.915	46.7	2.76	84,500	85
Apr 09.87	1.441	0.927	43.7	6.36	86,400	83
Apr 21.47	1.610	0.983	36.4	2.53	92,000	79
Apr 22.63	1.629	0.991	35.6	2.15	92,500	79
Apr 27.61	1.712	1.028	32.3	2.57	95,300	77
May 03.58	1.814	1.079	28.5	0.48	127,000	97
May 12.77	1.971	1.170	23.4	9.48	131,000	93
May 18.65	2.068	1.233	20.6	4.25	134,000	90
May 20.91	2.104	1.258	19.7	3.78	135,000	89
May 23.67	2.148	1.290	18.6	3.06	137,000	88
May 30.82	2.255	1.374	16.4	6.59	140,000	86
Jun 09.77	2.392	1.495	14.4	5.98	144,000	83
Jun 11.76	2.418	1.520	14.2	7.50	145,000	83
Jun 16.74	2.479	1.582	13.8	8.44	147,000	82
Jun 23.73	2.559	1.670	13.7	7.55	149,000	81

Date shown is the average over the range of observations. Δ and r_h are the geocentric and heliocentric distances, respectively, with the horizontal line drawn at perihelion. $\phi_{\rm ph}$ is the phase angle of the comet at the time of the observation, and $t_{\rm int}$ is the on-source integration time. The effective post-convolution beam size is given in both kilometers and arcsec.

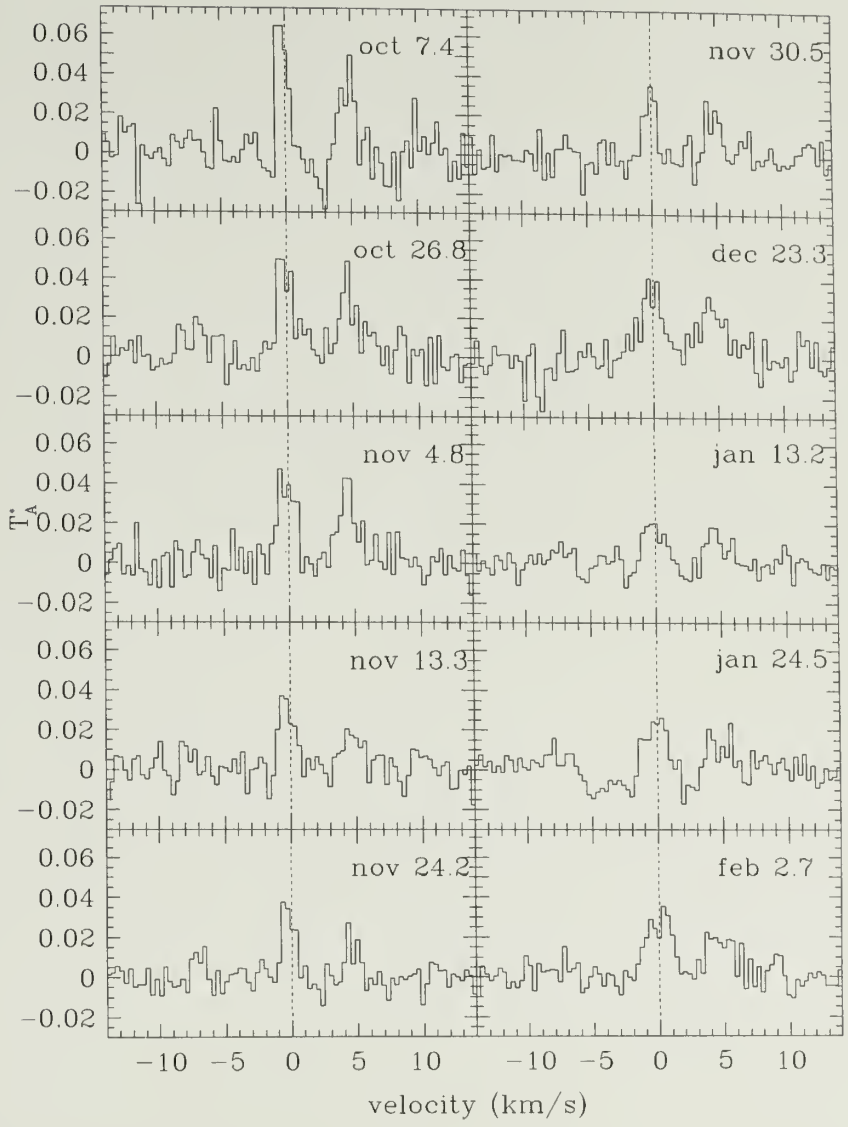

Figure 3.1. Spectra of HCN J=1-0 in comet Hale-Bopp, for the ephemeris position towards the nucleus, smoothed to a velocity resolution of 0.33 km s^{-1}, with a convolution scale of 200,000 km in the coma. The lines appear very narrow in early observations, and broaden as the comet approaches the Sun. The F=2-1 and F=1-1 hyperfine components, at 0 km s^{-1} and 4.84 km s^{-1}cometocentric velocity, respectively, are visible in all spectra, with the F=0-1 component at -7.06 km s^{-1} lying below the noise level.

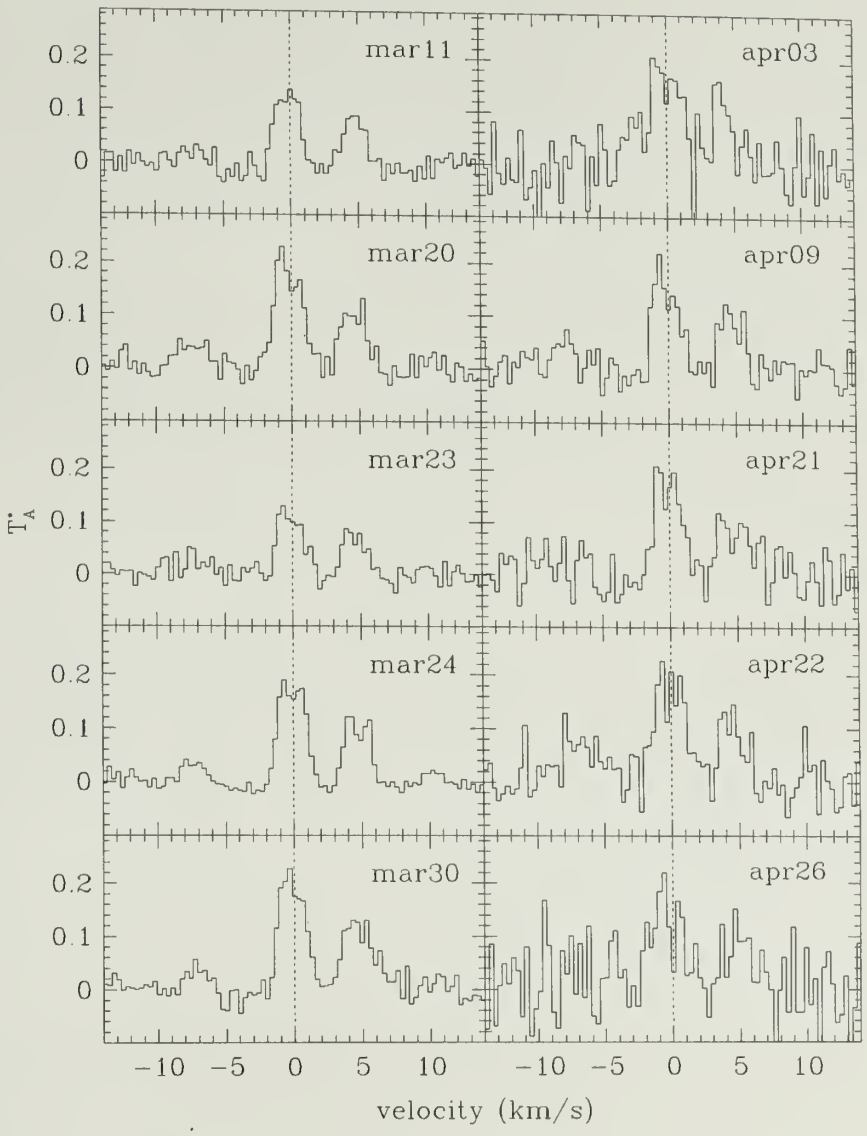

Figure 3.2. Spectra of HCN J=1-0 in comet Hale-Bopp, for the ephemeris position towards the nucleus, smoothed to a velocity resolution of 0.33 km s^{-1}, with a convolution scale of 60,000 km in the coma.

For these data, the low signal-to-noise ratio necessitated a large value of the convolution scale, which was chosen to be 200,000 km, or approximately twice the average beam resolution during this time. The convolved spectra for the nucleus position (effectively all the emission for this large an effective beam) are shown in Figure 3.1. All spectra, unless otherwise noted, are smoothed in velocity to a resolution of 0.33 km s^{-1}. The second grouping includes both perigee and perihelion of the comet, and spans March and April, 1997. A convolution scale of 60,000 km was chosen because it represents the average beam resolution during this period, with $\Delta \leq 1.7$ AU. These on-nucleus spectra are displayed in Figure 3.2. Post-perihelion, a third grouping was chosen for $1.8 < \Delta < 2.6$ AU, from the beginning of May until the close of observations in June, 1997. During this time, we employ a convolution scale of 100,000 km, representing the average beam resolution of this range of observations. These on-nucleus spectra are shown in Figure 3.3.

A grid of individual HCN J=1-0 spectra are displayed in Figure 3.4 for March 24, 1997. The samples, which have been smoothed by 5 velocity channels, are spaced by half the convolution scale (as in Table 3.1), and labelled with the offset from the nucleus in units of number of quarter-beam samples. It is evident in this figure that the HCN emission is detected over an extended area. Furthermore, it is evident that there are no striking anomalies in line width or in line shape across a single map.

3.3 Results

3.3.1 Spectral line shapes

As seen in Figures 3.1–3.3, the HCN J=1-0 line is split into 3 hyperfine components: F=2-1 (at a nominal velocity of 0 km s^{-1}), F=1-1 (offset to 4.84 km s^{-1}), and F=0-1 (offset -7.06 km s^{-1}). These hyperfine components appear, within the noise, in their expected statistical ratio of 5:3:1, which is consistent with

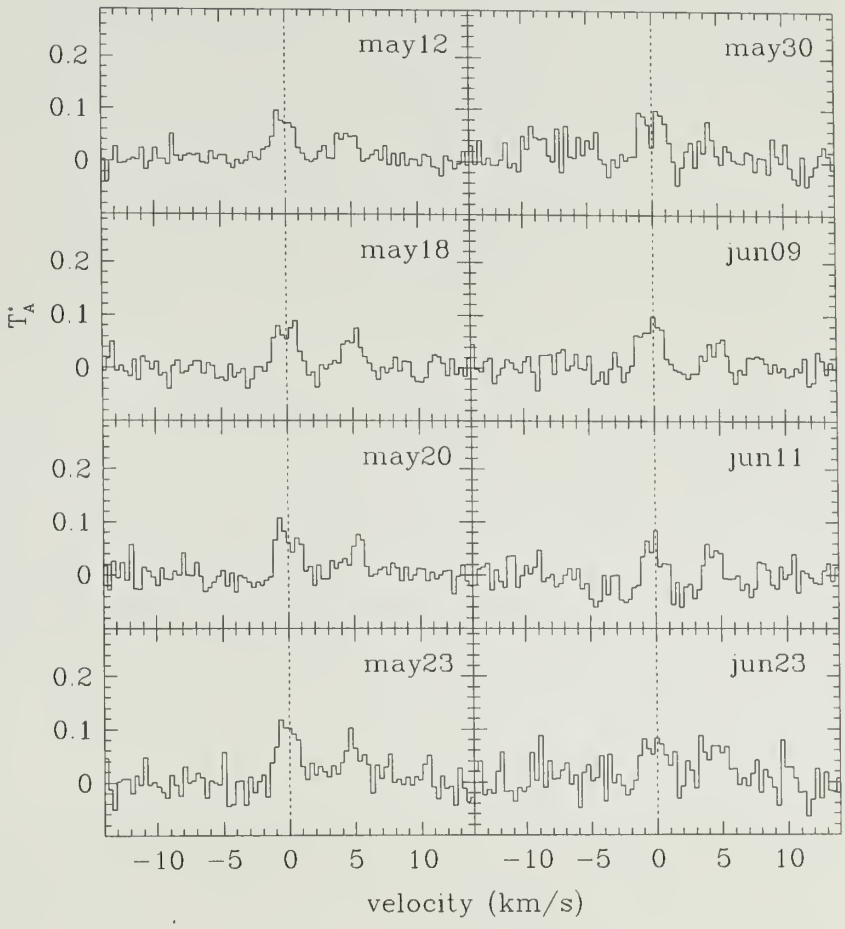

Figure 3.3. Spectra of HCN J=1-0 in comet Hale-Bopp, for the ephemeris position towards the nucleus, smoothed to a velocity resolution of 0.33 km s^{-1}, with a convolution scale of 100,000 km in the coma.

Table 3.2. HCN J=1-0 line parameters for on-nucleus spectra in comet Hale-Bopp

Average Date	Δ AU	r_h AU	ϕ_{rmph} deg.	peak mK	$\int$T dv mK $\frac{km}{s}$	$\sigma_{\int Tdv}$ mK $\frac{km}{s}$	Δv $\frac{km}{s}$	$\sigma_{\Delta v}$ $\frac{km}{s}$	$\overline{v}$ $\frac{km}{s}$
7.38 Oct	3.011	2.812	19.4	46	64	8	1.40	0.57	-0.26
26.82 Oct	3.053	2.579	17.9	46	73	7	1.59	0.55	-0.19
4.84 Nov	3.048	2.469	16.9	34	68	6	1.97	0.81	-0.26
13.27 Nov	3.026	2.365	15.8	28	48	5	1.72	0.75	-0.40
24.20 Nov	2.973	2.230	14.5	28	39	5	1.41	0.61	-0.33
30.54 Nov	2.929	2.150	13.9	27	36	6	1.32	0.66	-0.13
23.29 Dec	2.687	1.863	13.8	35	69	7	1.98	0.86	-0.07
3.20 Jan	2.528	1.725	15.6	19	16	5	0.83	0.57	-0.07
13.22 Jan	2.359	1.599	18.5	17	38	4	2.29	1.35	-0.20
24.46 Jan	2.151	1.459	22.8	23	48	4	2.09	0.92	-0.20
2.66 Feb	1.972	1.348	27.1	29	67	5	2.27	0.82	0.07
11.61 Mar	1.363	0.985	46.7	118	268	16	2.28	0.63	-0.27
20.55 Mar	1.317	0.937	49.0	169	479	18	2.84	0.58	-0.33
23.60 Mar	1.315	0.929	49.1	96	249	14	2.60	0.76	-0.26
24.72 Mar	1.317	0.924	49.1	139	422	11	3.03	0.47	-0.13
30.78 Mar	1.342	0.914	48.1	159	464	16	2.92	0.57	-0.26
3.81 Apr	1.374	0.915	46.7	173	484	50	2.80	1.58	-0.26
9.87 Apr	1.441	0.927	43.7	183	385	27	2.10	0.61	-0.40
20.50 Apr	1.586	0.974	37.4	252	313	55	1.24	0.57	-0.00
21.47 Apr	1.610	0.983	36.4	151	424	36	2.80	1.30	-0.13
22.63 Apr	1.629	0.991	35.6	163	511	37	3.13	1.39	-0.13
26.62 Apr	1.685	1.015	33.4	142	402	53	2.82	2.08	-0.59
27.61 Apr	1.712	1.028	32.3	210	272	52	1.29	0.67	0.07
12.77 May	1.971	1.170	23.4	71	170	12	2.40	0.80	-0.27
18.65 May	2.068	1.233	20.6	94	155	15	1.65	0.60	-0.13
20.91 May	2.104	1.258	19.7	69	161	15	2.35	1.16	-0.27
23.67 May	2.148	1.290	18.6	78	206	20	2.64	1.57	-0.26
30.82 May	2.255	1.374	16.4	67	197	21	2.92	2.08	0.13
9.77 Jun	2.392	1.495	14.4	71	177	15	2.50	1.24	-0.20
11.76 Jun	2.418	1.520	14.2	84	69	18	0.83	0.46	-0.33
16.74 Jun	2.479	1.582	13.8	45	59	18	1.32	1.24	-0.20
23.73 Jun	2.559	1.670	13.7	79	177	24	2.23	1.57	-0.13

Notes: Δ is the Earth-comet distance; r is the Sun-comet distance, with the horizontal line indicating perihelion. $\int Tdv$ is the integrated intensity in the J=1-0 F=2-1 line, of width Δv. The error on the median velocity $\overline{v}$ is assumed to be half the channel width, ~ 0.03.

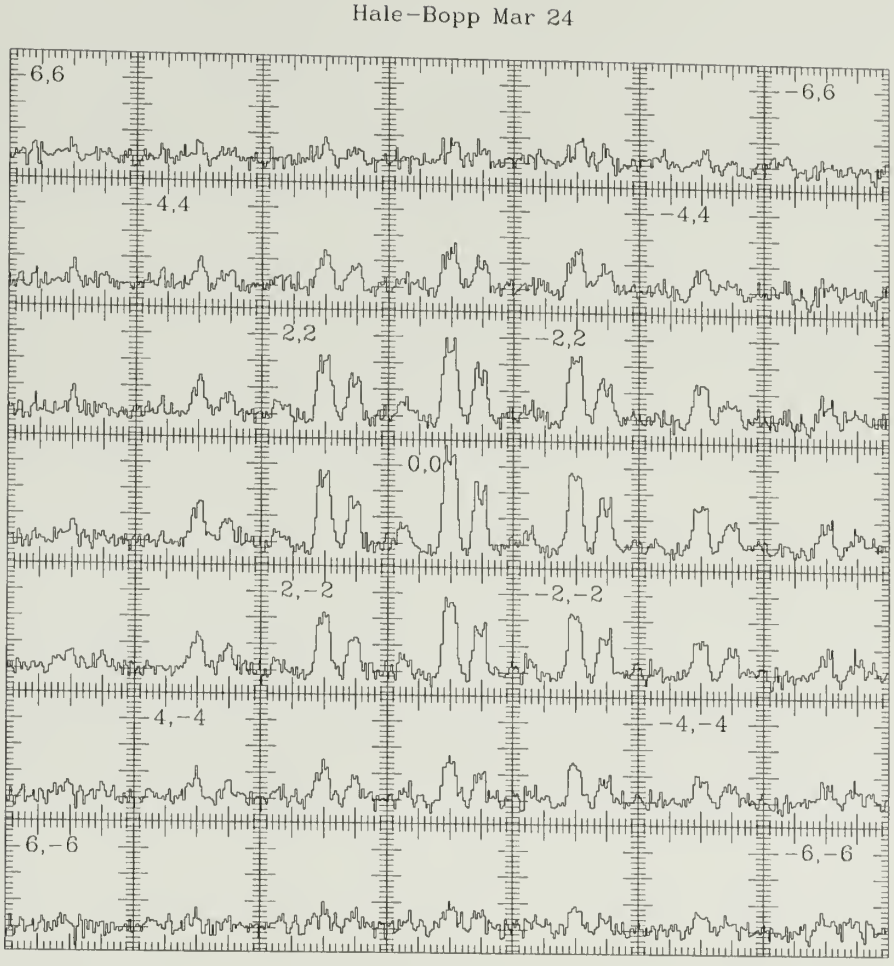

Figure 3.4. Convolved, 5-channel smoothed spectra corresponding to the map of March 24. Samples appear at half-beam intervals (30,000 km), with a self-consistent vertical scale, set by the nuclear spectrum.

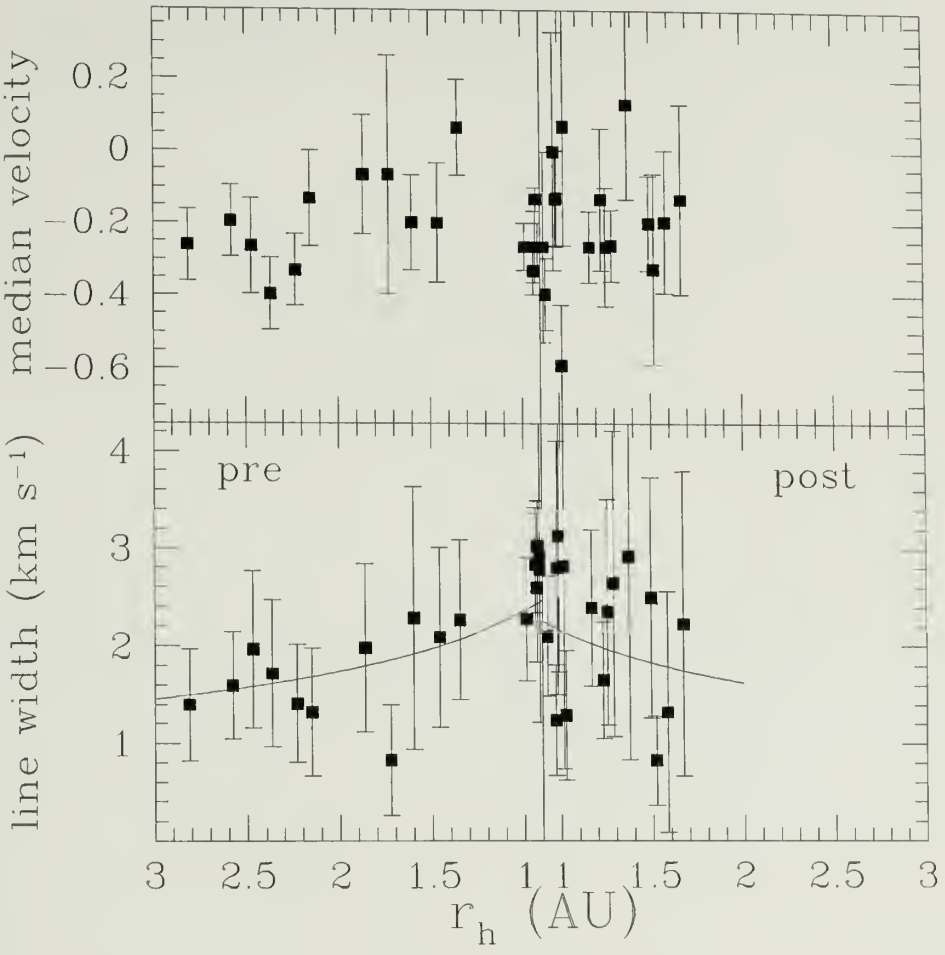

Figure 3.5. Estimates of the median velocity (upper) and line width (lower) versus r_h for comet Hale-Bopp. The solid curves in the lower panel represent twice the pre- and post-perihelion coma outflow velocities of Biver *et al.* (1998).

optically thin emission. The lines in Figure 3.1 are narrow, with a slight velocity offset towards the blue side of the line. As the comet approached the Sun (spectra in Figure 3.2), the lines became more symmetric and increased in width as the outflow velocity increased. Most spectra throughout the apparition appear broadly single-peaked, or even flat-topped, with a slight bias towards the blue wing.

3.3.2 Velocity distribution

In order to assess the degree of shift in velocity with respect to the ephemeris velocity of the comet, we compute the median velocity $\overline{v}$ of each spectrum: the point which divides the observed line area equally into two parts. These values, along with other observed line parameters and convolution scales for these spectra are given in Table 3.2. The integrated intensity, median velocity, and line width are computed after the removal of a baseline from the spectra, and assume that the line lies entirely within the cometocentric velocity range {-2,2}. $\sigma_{\rm int}$ is an estimate of the error on the integrated intensity.

The upper panels of Figure 3.5 display the evolution of the median velocity, versus pre- and post-perihelion heliocentric distance r_h. This velocity is generally blue-shifted approximately 0.2 km s^{-1} with respect to the cometocentric velocity, with progressively more blue shift at larger pre-perihelion distances. The lower panel of Figure 3.5 shows the estimated line width in the spectra, estimated by dividing the integrated intensity by the peak temperature. For comparison, superimposed on the points is a solid curve, representing twice the line half-width derived by Biver *et al.* (1998) for the appropriate (pre- or post-perihelion) case. Although these values are generally consistent with those derived by Biver *et al.*, the immediately pre-perihelion data of March, 1997 suggest slightly larger outflow velocities.

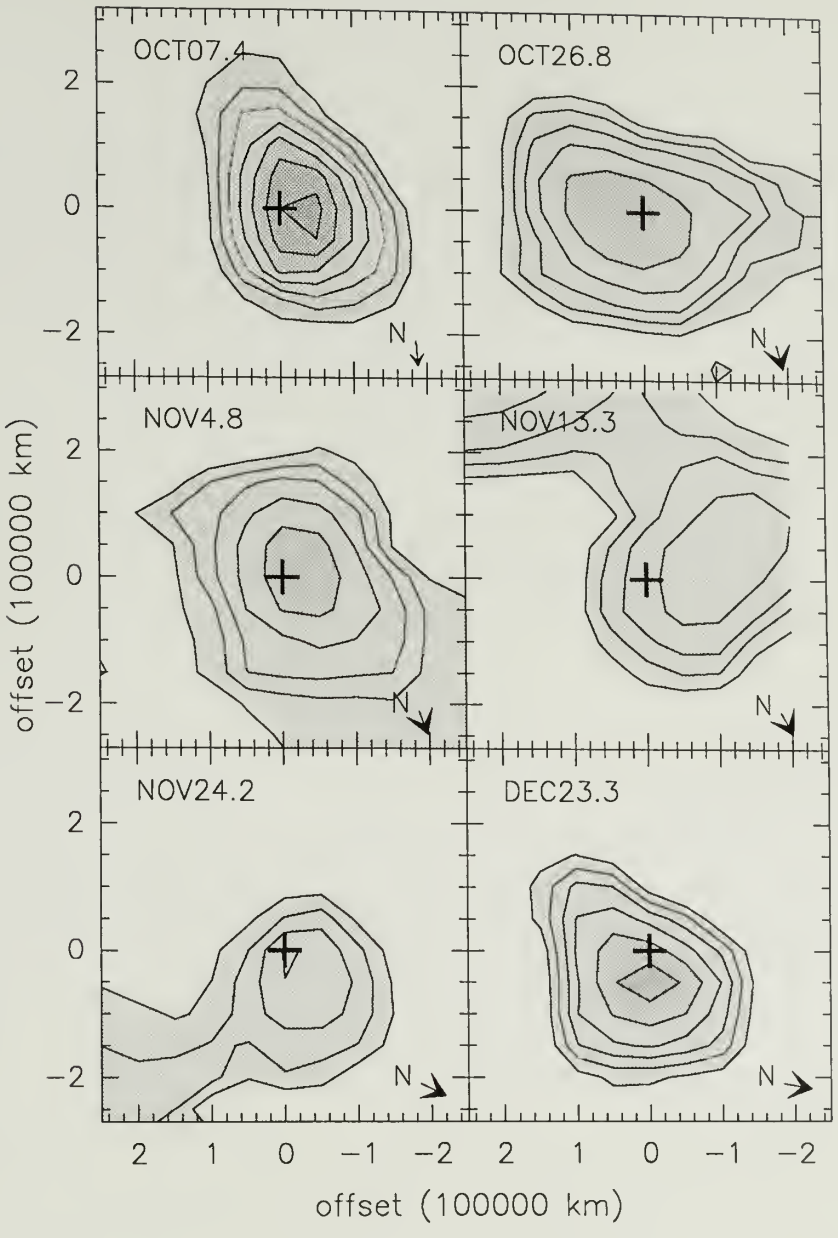

Figure 3.6. Maps of integrated intensity in the HCN J=1-0 F=2-1 line for comet Hale-Bopp between Oct 6 – Dec 23, 1996. In this and all other contour maps, the cross indicates the nucleus ephemeris position, with the projected direction to the Sun on the left, and the direction of North as indicated. The spatial axes of the map are in units of 100,000 km of the coma, with a 200,000 km convolution scale. The contour interval is 8 mK km s^{-1}, beginning at 24 mK km s^{-1}.

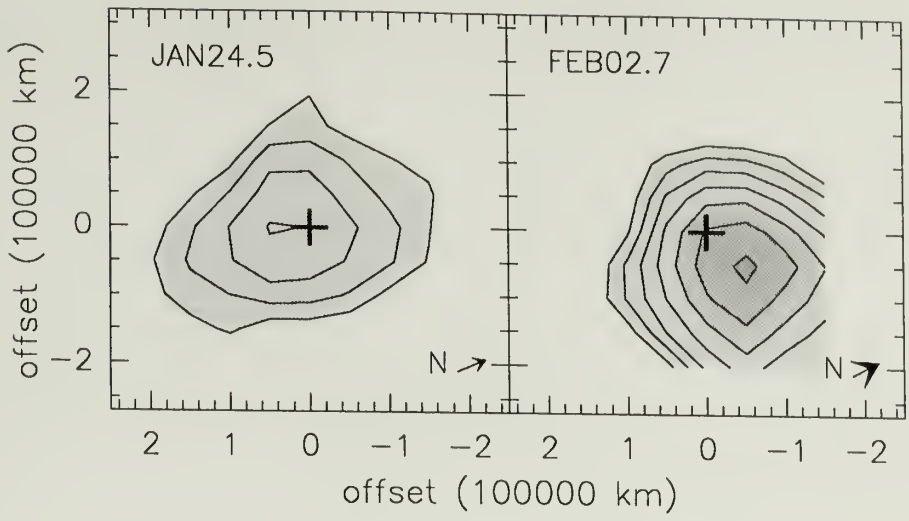

Figure 3.7. Maps of integrated intensity in the HCN J=1-0 line for comet Hale-Bopp on Jan 24 and Feb 2, 1997, as in Figure 3.6.

3.3.3 Map morphologies

HCN spectra were assembled into emission maps by computing the integrated intensity in each J=1-0 F=2-1 line over the velocity interval {-1,1} for early data, and {-2,2} for near-perihelion data. The distant pre-perigee maps are shown in Figures 3.6 and 3.7, contoured at intervals of 8 mK km s^{-1}, approximately one standard deviation in a typical averaged map. The near-perihelion data are shown in Figure 3.8, contoured at intervals of 23 mK km s^{-1}. Due to the poor weather which prevailed over the latter part of April, 1997, the line rms was considerably higher, so these maps are shown in Figure 3.9, with a contour interval of 40 mK km s^{-1}. The remaining post-perihelion maps, at the larger convolution scale of 100,000 km, are displayed in Figure 3.10, with a contour interval of 15 mK km s^{-1}.

In order to assess the degree of symmetry which appears in the maps, we average the integrated intensities at each cometocentric distance, to create a single radial profile of the emission. These radial distributions, a selection of which are shown in Figure 3.11, were then subtracted away from the maps of Figures 3.8 —

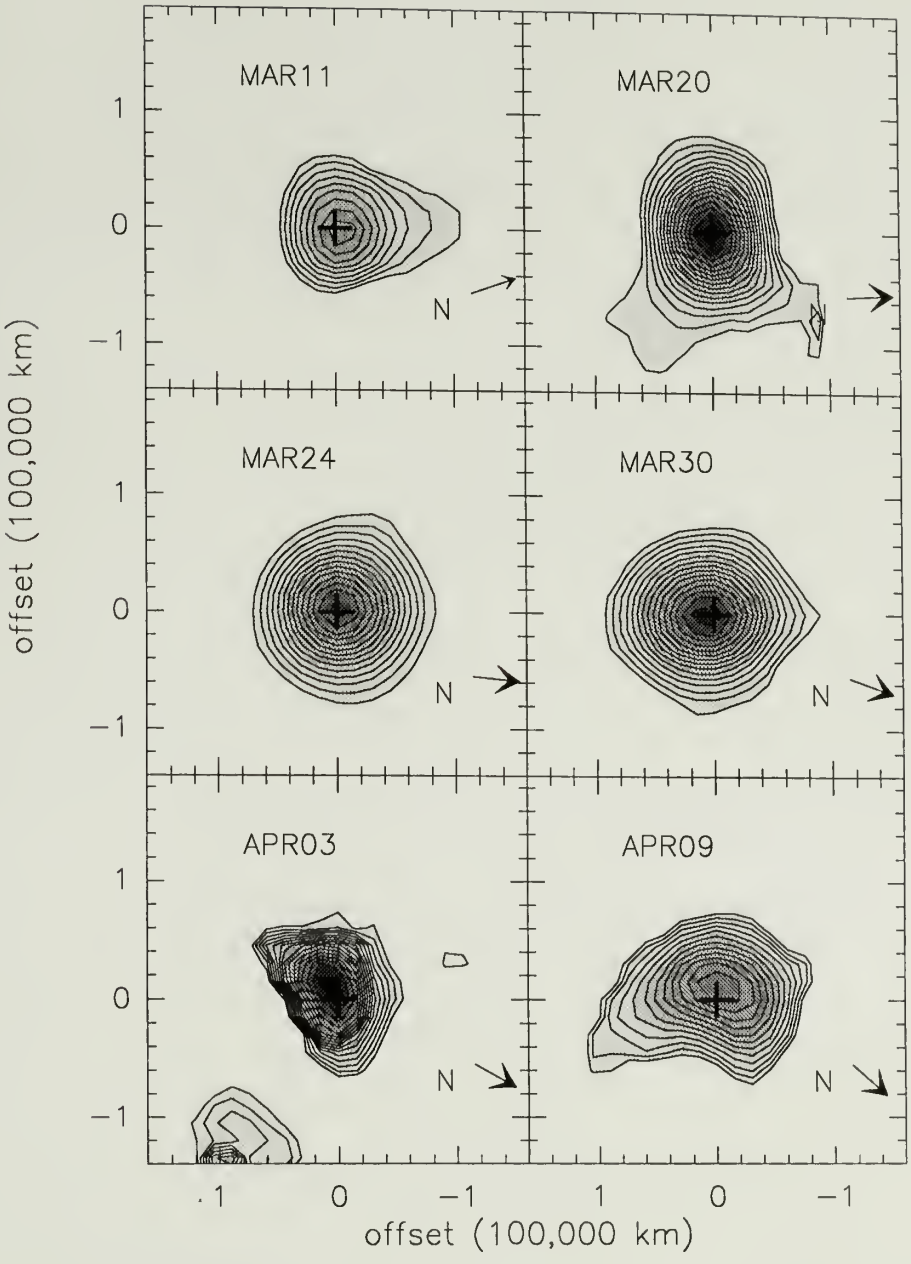

Figure 3.8. Maps of integrated intensity in the HCN J=1-0 F=2-1 line for comet Hale-Bopp between March March 11 – April 09, 1997. The contour interval is 23 mK km s^{-1}, beginning at 115 mK km s^{-1}, approximately the 10- σ level.

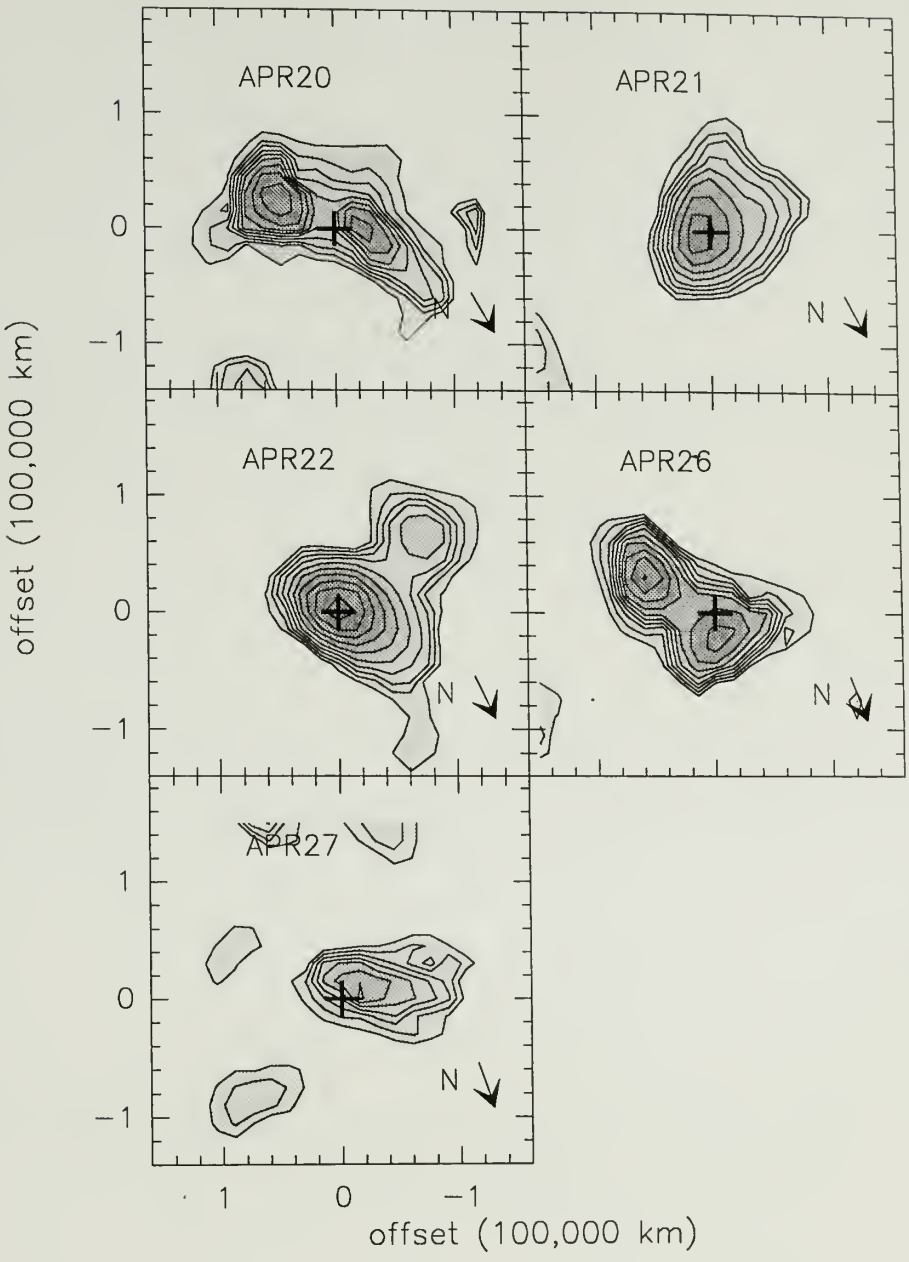

Figure 3.9. Maps of integrated intensity in the HCN J=1-0 line for comet Hale-Bopp in the latter part of April 1997. The contour interval is 40 mK km s^{-1}, beginning at 120 mK km s^{-1}.

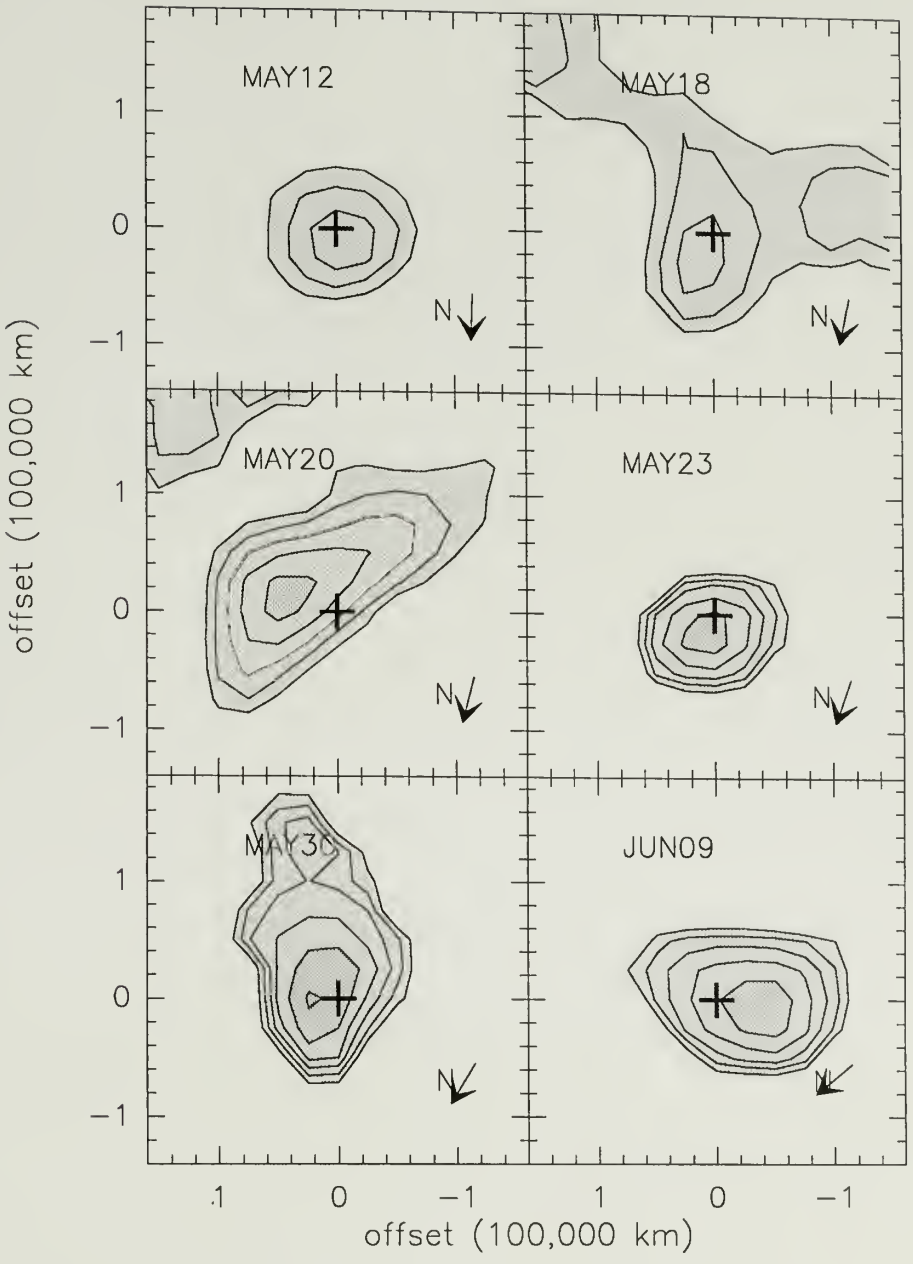

Figure 3.10. Maps of integrated intensity in the HCN J=1-0 line for comet Hale-Bopp between May 12 – June 09, 1997. The contour interval is 20 mK km s^{-1}, beginning at 100 mK km s^{-1}.

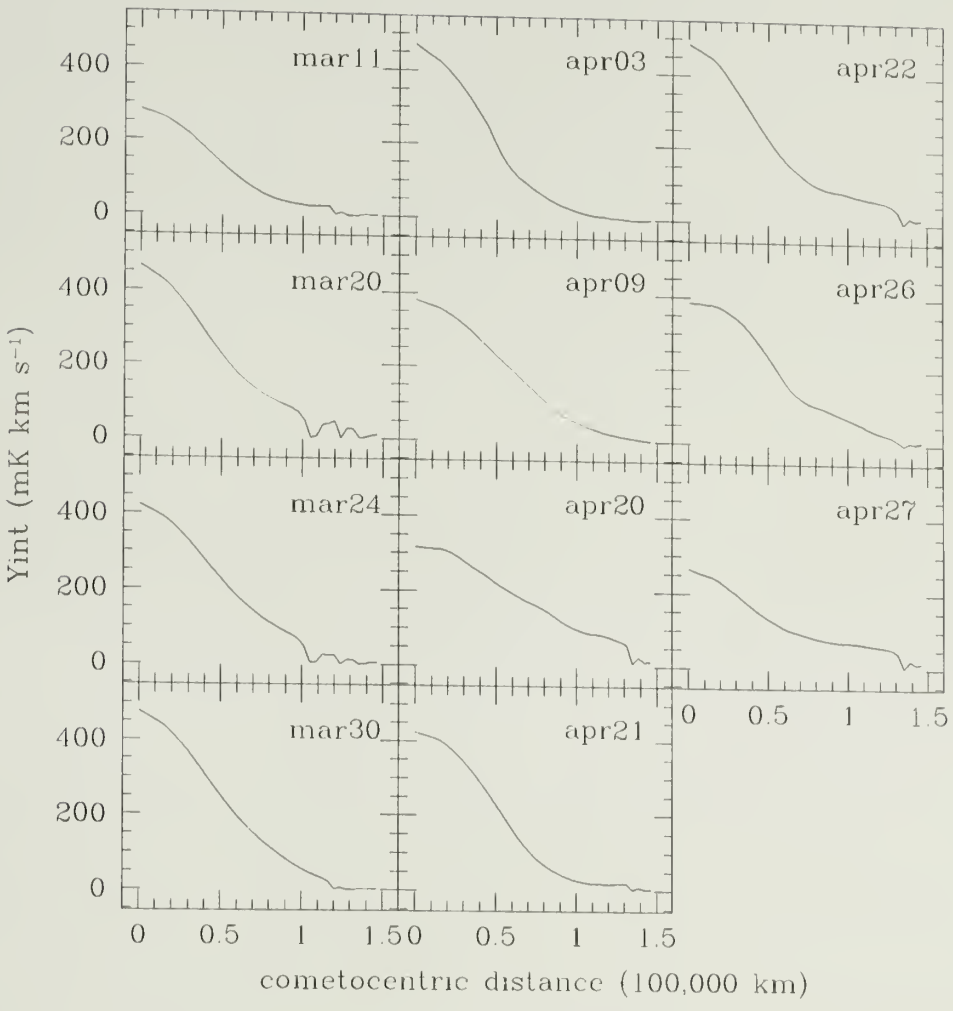

Figure 3.11. Azimuthally averaged integrated intensity versus cometocentric distance, for the maps shown in Figures 3.8 and 3.9.

shown in Figure 3.11, were then subtracted away from the maps of Figures 3.8 — 3.9 to create residual maps. Such residual maps, shown in Figure 3.12 — 3.13, may reveal inaccuracies in the assumed nucleus position in addition to actual coma structures. The contours lie at intervals of σ, the mean rms level for each date, beginning at 3 σ for both positive levels, indicating an excess of HCN with respect to the average, and negative, indicating a deficiency. A small overabundance of HCN appears at the periphery of the maps on March 11 and 20, with occasional 3-5 σ areas such as that near the nucleus on March 30. Generally speaking, the appearance of a large residual on the periphery of the map may indicate a discrepancy between the observed and the actual position of the comet (such as seen by the offset in the peak relative to the tracked position in the map of Feb. 02, 1997), or an edge effect in the subtraction (as seen March 24, 1997).

3.4 Analysis

Spectral line mapping data provide several means of probing structures in cometary comae. First, spatially resolved images provide a means to assess the extent of emission and the degree of symmetry in the maps. Second, individual spectra resolve velocity structures which constrain the motions of the gas within the observed beam. Finally, the variations in spectral line shapes over the mapped region further constrain the kinematics of the gas over the entire observed coma. A model of the coma must appropriately predict both the observed line shapes and the spatial distribution of the emission.

We have simulated the HCN distribution in the coma of comet Hale-Bopp using the Monte Carlo model described in Appendix A. The model spectra which result from the simulation provide a means to assess the accuracy of the model in terms of the line width and shape as well as the extent and distribution of emission in the map. Furthermore, the amplitude of the model spectra can be related to the data through the gas production rate of the comet. As in Chapter 2,

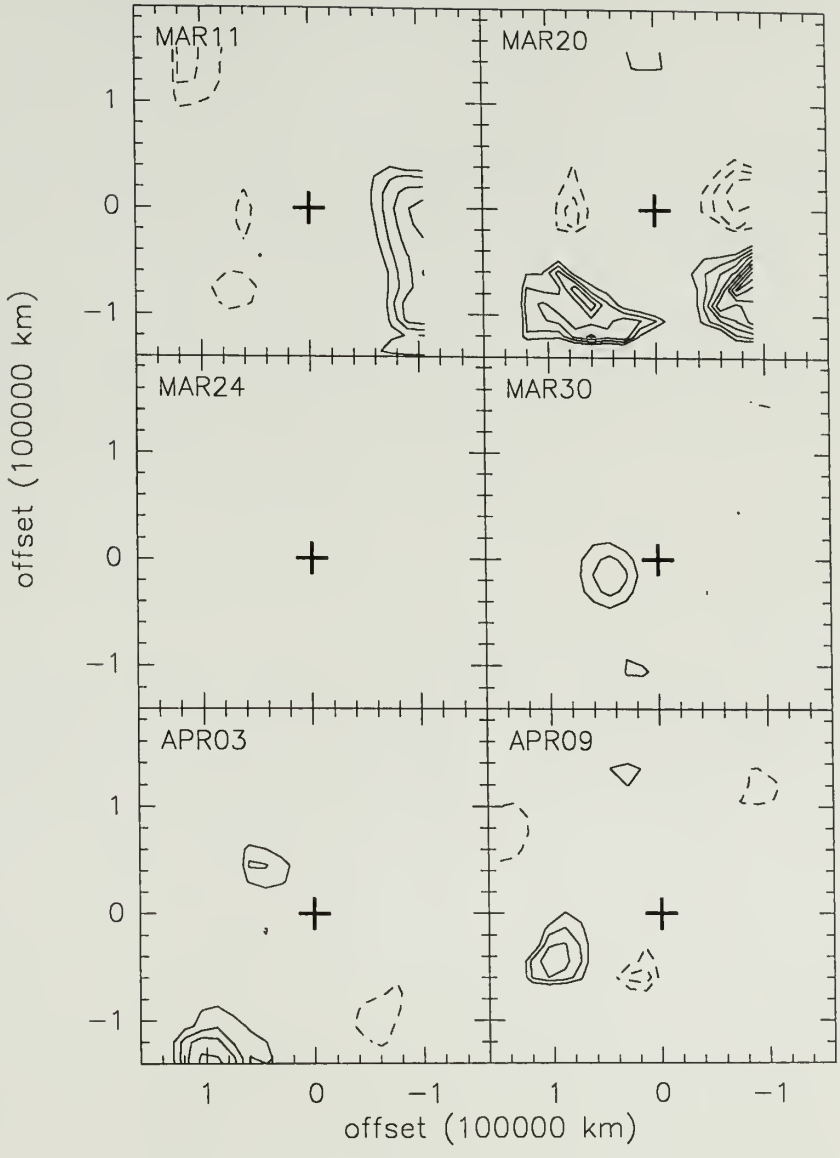

Figure 3.12. Maps of residual integrated intensity, after an azimuthally-averaged profile has been subtracted. The contour interval is approximately equal to the typical noise level of the maps, truncated below 3- σ, so the intensity of the residual image approximates the level to which the asymmetry exceeds the noise. Images are oriented as in Figures 3.8.

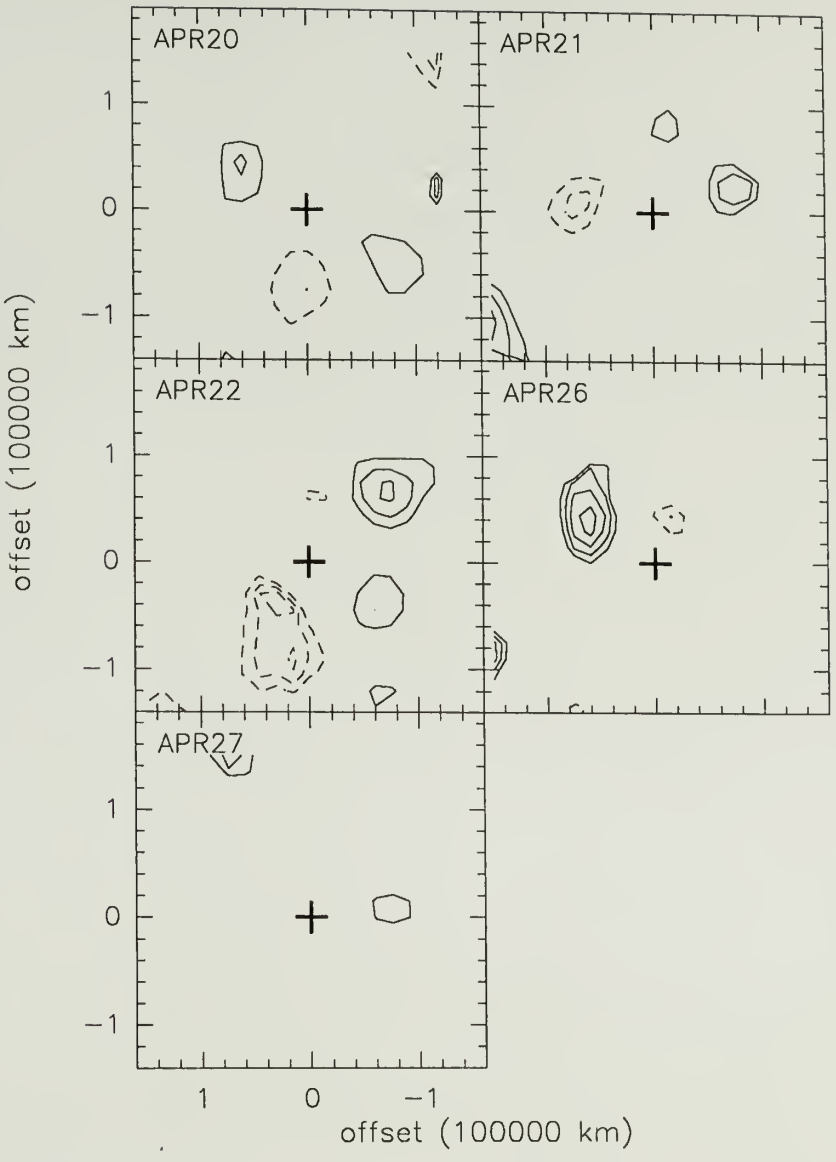

Figure 3.13. Maps of residual integrated intensity in the HCN J=1-0 line for comet Hale-Bopp, after an azimuthally-averaged profile has been subtracted, as in Figure 3.12.

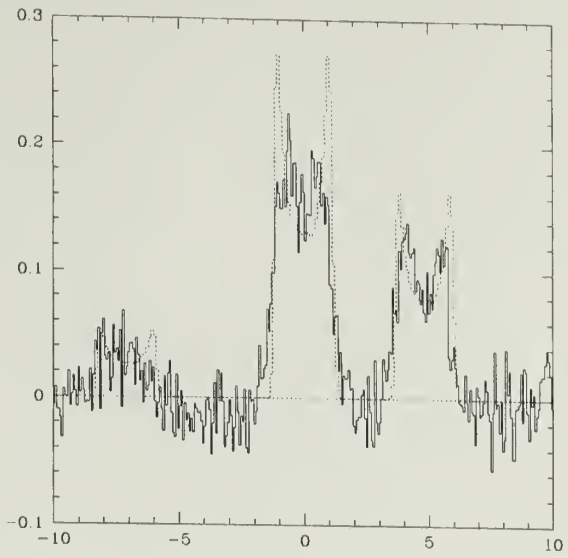

Figure 3.14. Spectrum for comet Hale-Bopp, March 24, 1997, data (solid lines) and spherically-symmetric constant-velocity model (dotted lines). Note that the model predicts sharper peaks than appear in the data.

the data are better characterized by models with a constant fraction of HCN molecules in the J=1 state than by the two-component excitation discussed in Appendix B; however, the difference in predicted intensity is minimal due to the large beam size (due to geocentric distances $\Delta > 0.9$ AU). For simplicity, we assume a constant excitation, in the collisional limit, unless otherwise specified. We use this model to estimate the level of velocity structure present in the coma of comet Hale-Bopp, and to estimate the production rate of HCN.

3.4.1 Line shapes

For an optically thin coma which is expanding at a constant velocity in a perfectly symmetric spherical manner, the expected line shape would be sharply double-peaked (Olofsson *et al.* 1982). However, the observed lines in comet Hale-Bopp are generally inconsistent with such an idealized model of the coma. As seen in Figures 3.1–3.3, the on-nucleus spectra appear broadly single-peaked or

flat-topped on most occasions. When a double-peaked morphology does occur, it is only a fraction of what would be expected in the ideal case. For example, the on-nucleus spectrum on March 24, 1997, displayed with no smoothing in Figure 3.14, appears with two small rounded peaks atop a broader flat distribution. This structure is even more apparent in the F=1-1 hyperfine line centered at 4.8 km s^{-1}. The simulated spectrum with a constant expansion velocity is superimposed for comparison. Obviously, the model (solid line) is more sharply peaked than the data (dotted line).

As shown in Chapter 2 for comet Hyakutake, a more accurate representation of the data is achieved if the outflow velocity in the coma is allowed to vary with distance from the nucleus. Such structure is also consistent with both *in situ* measurements of gas velocities in comet P/Halley (Lammerzahl *et al.*, 1987) and theoretical computations (Combi, 1989; Combi, 1996). We employ a simple power-law approximation for the outflow velocity (Ge, 1993):

$$V_{exp} = V_0 \left(\frac{r}{r_{\text{nucleus}}} \right)^{\alpha}. \tag{3.1}$$

The value of these velocity parameters depends upon both heliocentric distance r_h and production rate (Tacconi-Garman 1989). Due to the high water production rate of comet Hale Bopp ($\sim 10^{31}$ mol s^{-1} at perihelion) and large nuclear size, we might expect different values of V_0 and α than those which characterized the observations of comet Hyakutake. Furthermore, the spectral line shapes are wider than 1 km s^{-1}, and typically single-peaked or flat-topped. As shown in Figures 2.17 and 2.18, such morphologies can occur within the range of parameters investigated. We have chosen 4 dates in March, 1997, to analyze for a determination of the best-fit velocity model parameters. These dates are March 11 and 20, which display some degree of asymmetry (Figures 3.8, 3.12), and March 24 and 30, which appear more symmetric. The on-nucleus spectrum for March 20

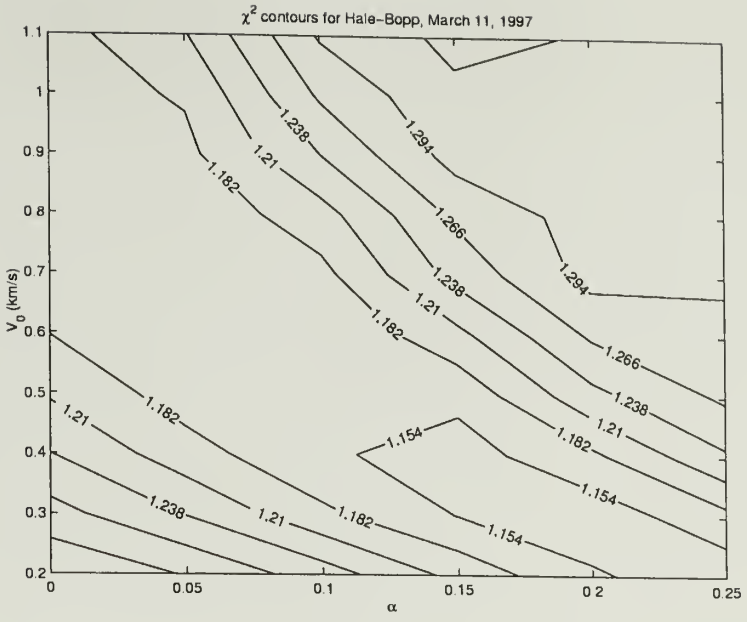

Figure 3.15. Contours of χ^2 for power-law velocity models for comet Hale-Bopp for the conditions on March 11, 1997. Although a range of pairs of parameters appear to minimize χ^2, power-laws with larger α are favored. On this date, the trough in χ^2 falls at fairly low values of initial velocity V_0.

shows a slight excess on the blue side of the peak, otherwise the spectra appear symmetric.

We examine a range of parameters $V_0 = 0.2$ to 1.1, and $\alpha = 0$ (the constant velocity case) to 0.25. We compute the residuals between the data and the model, and estimate χ^2 over 25 points in the map, including the nucleus position. The values of χ^2 are small along a "trough" spanning from the expected constant-velocity case (with outflow velocities ~ 1.1 km s^{-1}), to low initial velocities with relatively large ($\alpha \sim 0.2$) exponents. Contours of χ^2 are shown for constant-excitation models on all four of these dates, in Figures 3.15 – 3.18. The velocity structures on the latter three dates appear to be consistent with the same set of velocity models, with the smallest χ^2 around $V_0 \sim 0.5$ km s^{-1} and $\alpha \sim 0.14$. The contours of minimum χ^2 for March 11, on the other hand, are shifted towards

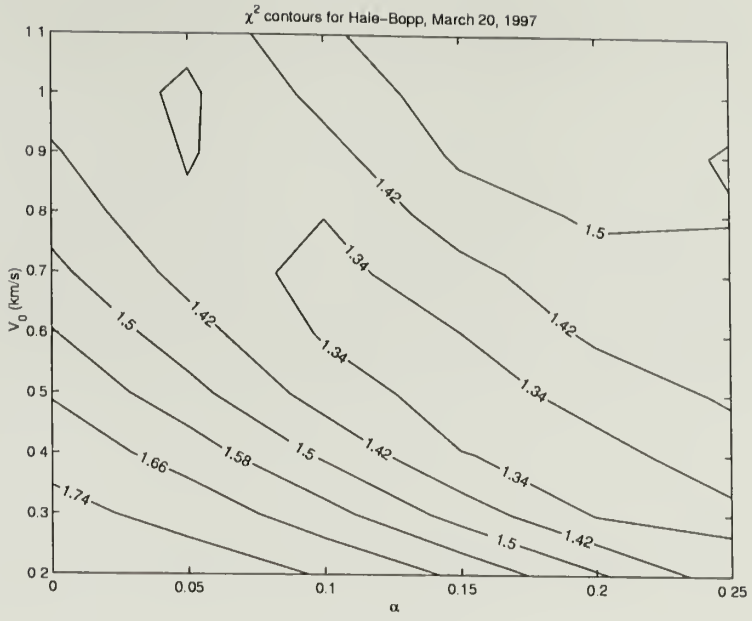

Figure 3.16. Contours of χ^2 for power-law velocity models for comet Hale-Bopp for the conditions on March 20, 1997.

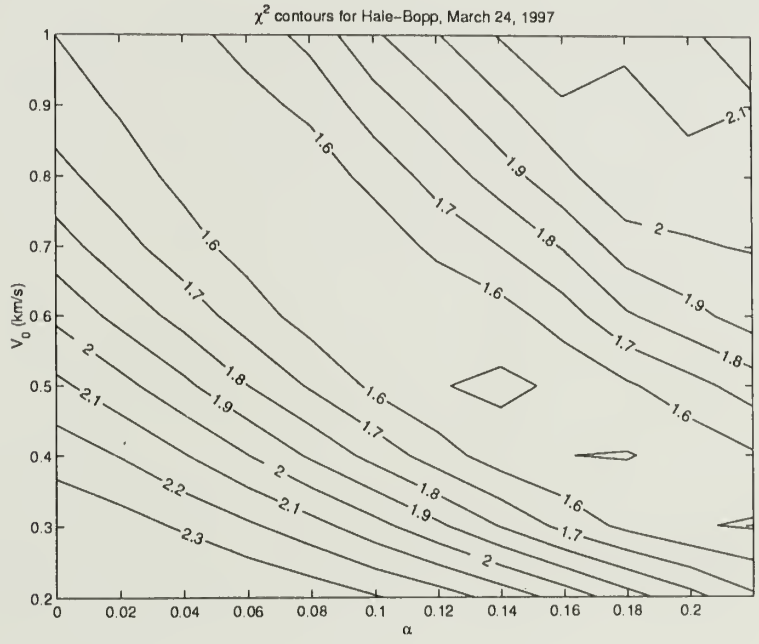

Figure 3.17. Contours of χ^2 for power-law velocity models for comet Hale-Bopp for the conditions on March 24, 1997.

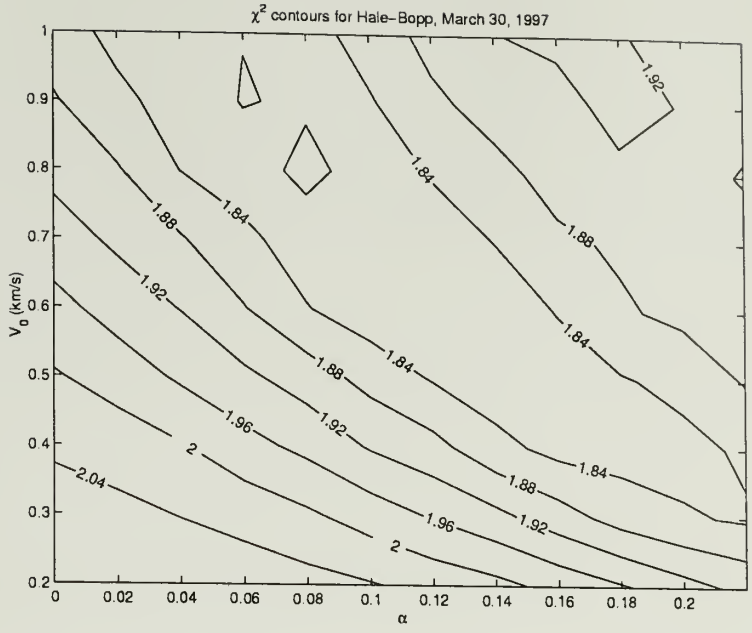

Figure 3.18. Contours of χ^2 for power-law velocity models for comet Hale-Bopp for the conditions on March 30, 1997.

lower initial velocities, and favor higher exponents. The minimum in χ^2 on this date occurred at the extreme of the investigated range at $V_0 = 0.2$ km s^{-1} and $\alpha = 0.25$.

Grids of the best-fit velocity model in comparison to the data are shown for March 11 in Figure 3.19, and for March 20 in Figure 3.20. On both these dates, though more strikingly on March 11, there are excesses in the observed spectra (in one or more positions) over the value which is predicted by the model. These excesses also appear in the residual maps of Figure 3.12. In addition, the on-nucleus (0,0) spectrum for March 20 highlights the blue-side asymmetry of the observed line. Grid spectra for March 24 and 30 are shown in Figures 3.21 and 3.22, respectively. These model lines represent the data well over the entire grid.

We propose that the observed emission from comet Hale-Bopp was largely symmetric on the spatial scales observable by our beam. However, smaller spatial

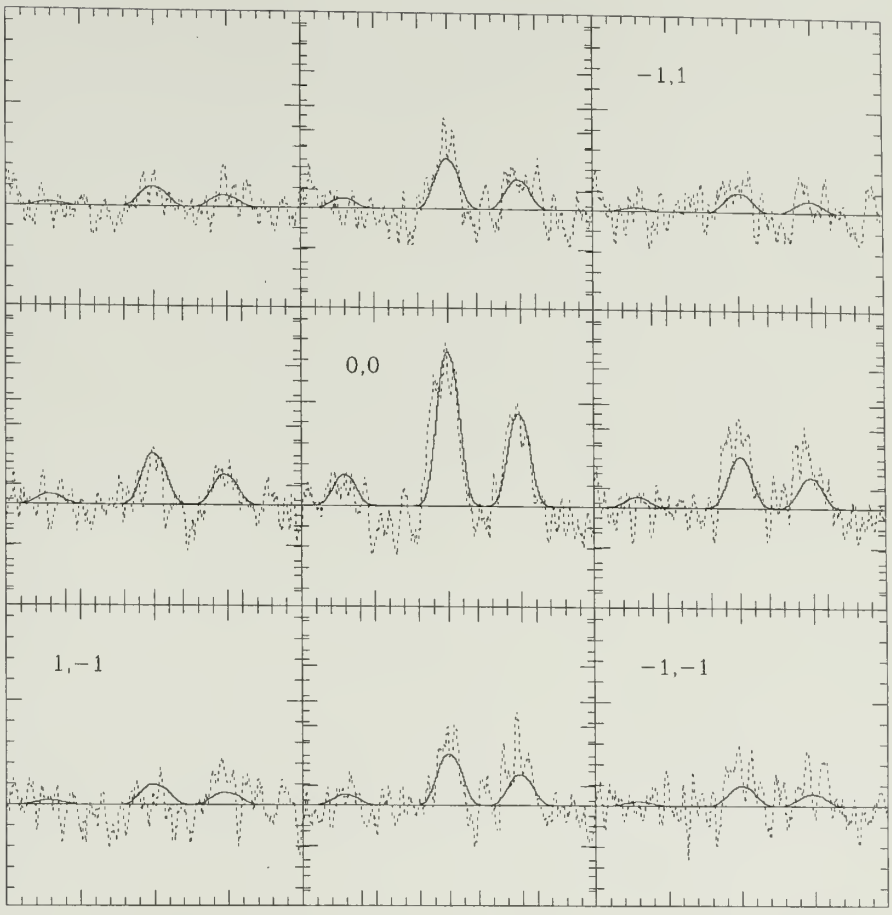

Figure 3.19. A comparison of the HCN J=1-0 on-nucleus observed spectrum (center) and other spectra one beam out in the map (as labelled). Superimposed on the data (dotted lines) are the power-law velocity models (solid line) best-fit for comet Hale-Bopp on March 11, 1997. $V_0 = 0.2$, $\alpha = 0.12$ in equation 3.1. Although the line shapes and intensity distribution fit fairly well in most positions, the model underestimates the observed spectra in the (-1,0) and (-1,-1) positions.

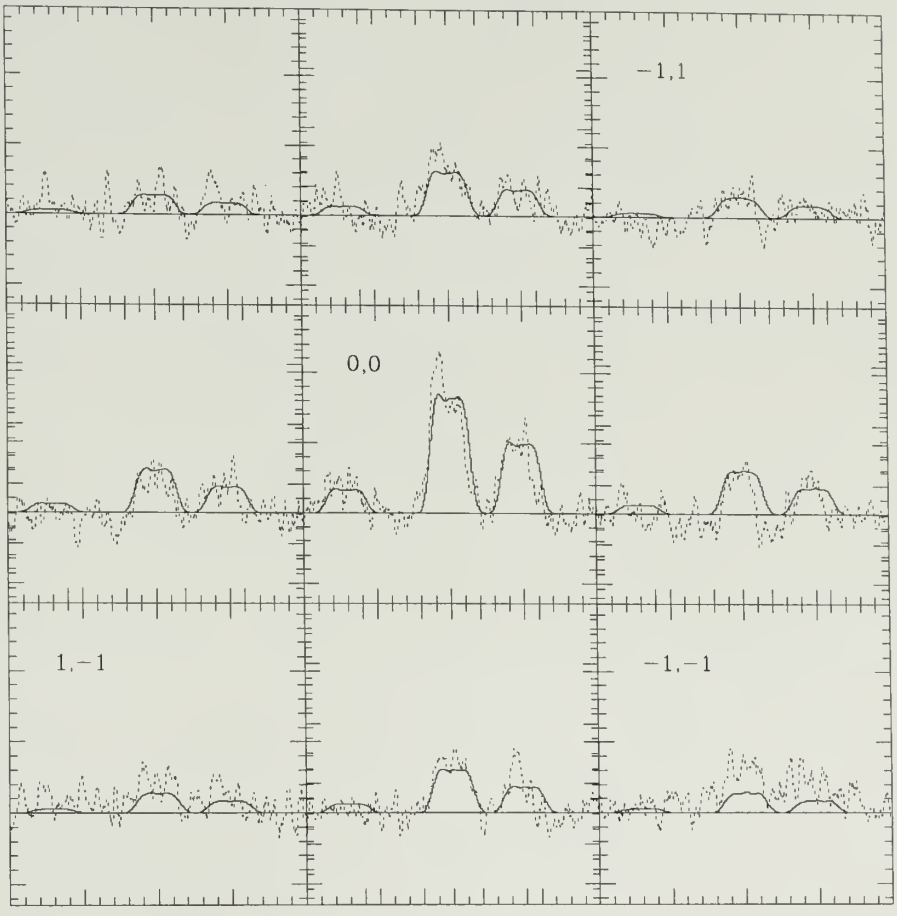

Figure 3.20. A comparison of the HCN J=1-0 on-nucleus observed spectrum (center) and other spectra one beam out in the map (as labelled). Superimposed on the data (dotted lines) are the power-law velocity models (solid line) best-fit for comet Hale-Bopp on March 20, 1997. $V_0 = 0.5$, $\alpha = 0.15$ in equation 3.1. Although the line shapes and intensity distribution fit fairly well in most positions, the model underestimates the observed spectrum in the (-1,-1) position, and the on-nucleus spectrum and (0,1) display a slight excess on the blue side.

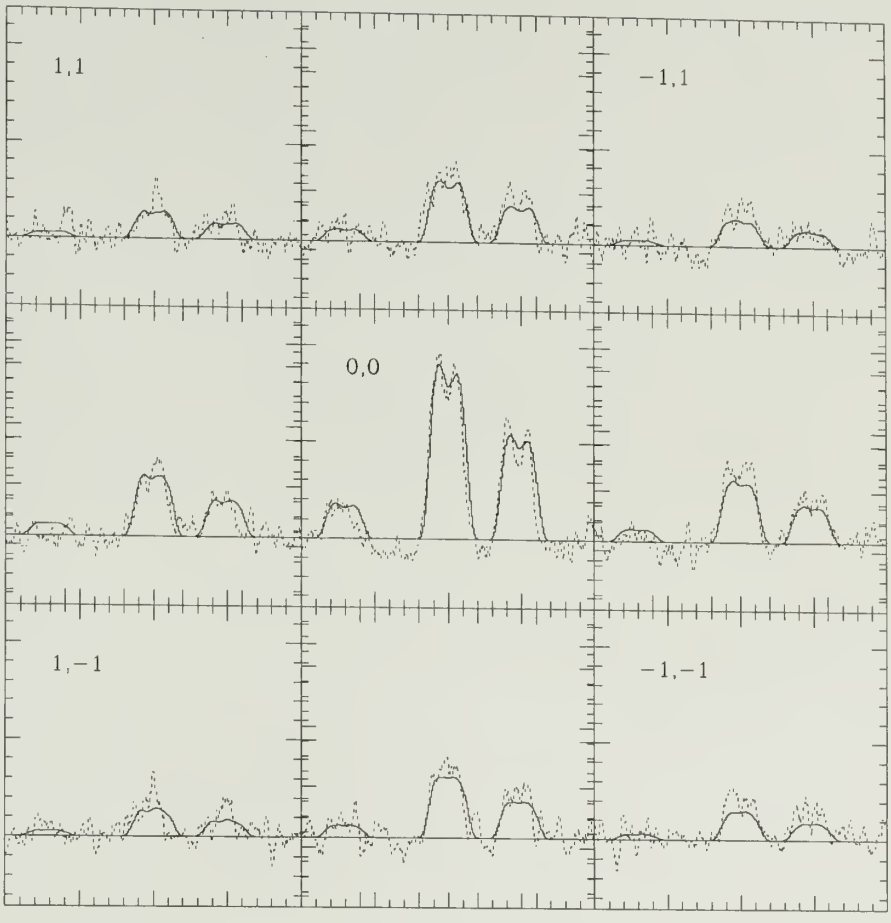

Figure 3.21. A comparison of the HCN J=1-0 on-nucleus observed spectrum (center) and other spectra one beam out in the map (as labelled). Superimposed on the data (dotted lines) are the power-law velocity models (solid line) best-fit for comet Hale-Bopp on March 24, 1997. $V_0 = 0.5$, $\alpha = 0.14$ in equation 3.1. The line shapes and intensity distribution fit fairly well over the area, although the model appears flatter than the observed double-peaked spectrum at (0,0).

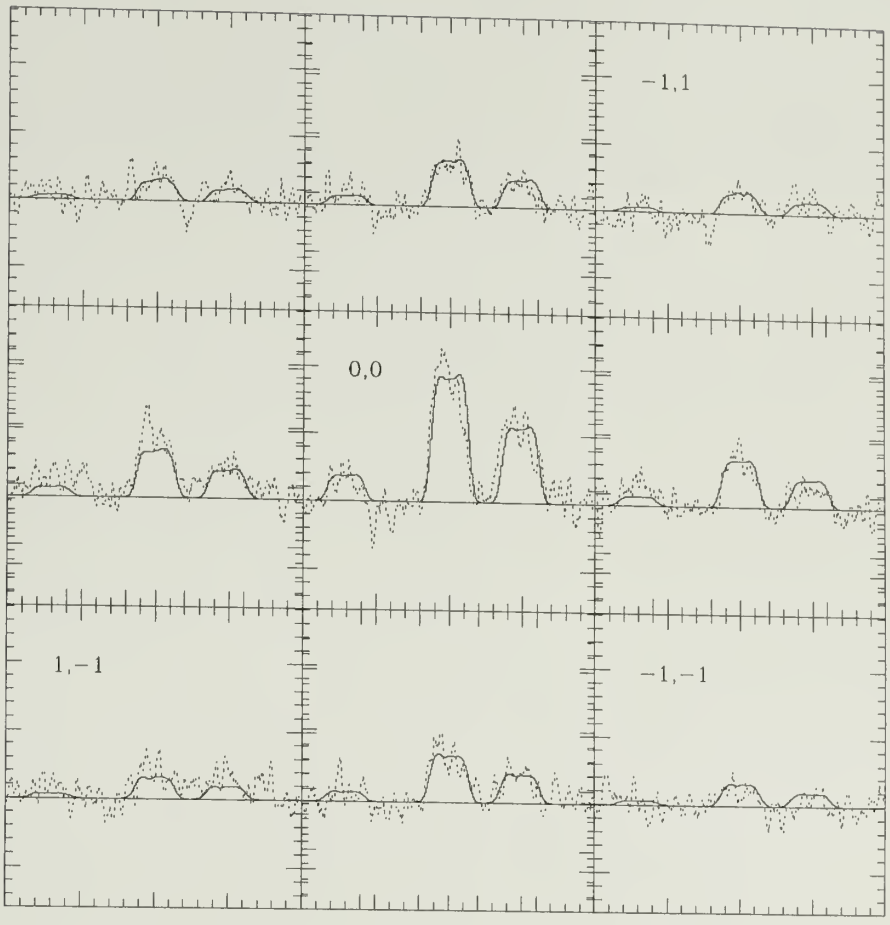

Figure 3.22. A comparison of the HCN J=1-0 on-nucleus observed spectrum (center) and other spectra one beam out in the map (as labelled). Superimposed on the data (dotted lines) are the power-law velocity models (solid line) best-fit for comet Hale-Bopp on March 30, 1997. $V_0 = 0.5$, $\alpha = 0.14$. The line shapes and intensity distribution fit fairly well over the area.

asymmetries likely exist, corroborated by excess residuals with respect to the average data (as on the periphery of maps for March 11 or 20), and with respect to the symmetric model in one or more of the grid spectra. Comparison of the data and a spatially symmetric model with an outflow velocity approximated by a power-law provides a means of identifying such asymmetries. Since the spectra are highly resolved in velocity, the effects of coma kinematics appear as features in the spectral shape. Uniform outflow creates very sharp double-peaked lines, while a large range of velocities along the line of sight creates rounded or flat-topped lines. In more pronounced cases, coma structures affect the spectral lines to the point where model fits favor larger exponents in the power-law. We do not believe that the actual outflow velocity is necessarily following a steeper power-law in these cases, only that a steeper representative power-law is indicative of additional irregularities in the coma kinematics. The evidence for this is shown in comparison between the χ^2 contours for March 11, 1997 in comet Hale-Bopp (Figure 3.15) and the contours for March 22, 1996 in comet Hyakutake (Figure 2.24). In both of these cases, there appears to be a significant spatial asymmetry, and the lowest values of χ^2 occur at large values of the power-law exponent α, suggesting that a broad range of velocities are observed within the beam.

3.4.2 Gas Production Rates

As part of the analysis of the data over the range of heliocentric distance observed, we must compute a total HCN production rate for each observation. The excitation conditions for comet Hale-Bopp are outlined in Appendix B, where it is estimated that the transition from thermal collision-dominated excitation to solar radiative excitation occurs around 30,000 km from the nucleus. This value is computed assuming a small value of the collision-cross section, and likely underestimates the true size of the thermally-excited coma. We follow the approach used in Chapter 2, in adopting a constant population in the J=1 state,

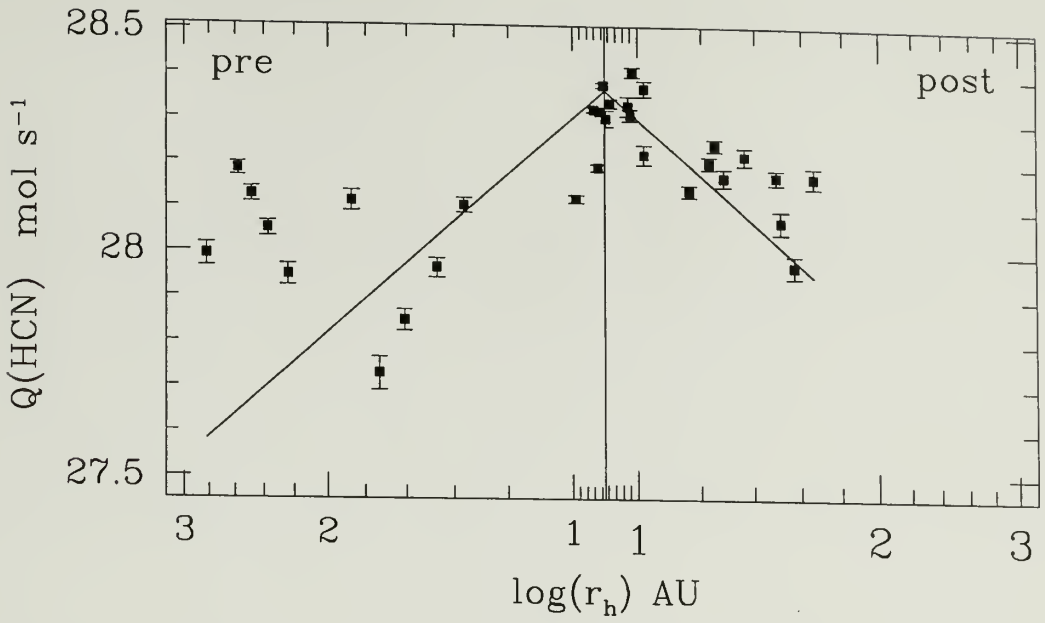

Figure 3.23. Production rates for HCN in comet Hale-Bopp, for both pre-perihelion (left) and post-perihelion (right) observations. The solid line shows the water production rate of Biver *et al.*(1998), scaled by 0.002.

due to excitation by collisions. The temperature is approximated with the law given by Biver *et al.*(1998), shown in Table A.1.

We use the spherically symmetric constant velocity distribution to model the spatial distribution of HCN. This technique is outlined in section A.4 of Appendix A. The resulting production rates for comet Hale-Bopp are shown in Table 3.3, and plotted versus r_h in Figure 3.23. Superimposed for comparison is the H_2O production rate of Biver *et al.* (1998), scaled by 0.002, suggesting a relative abundance relative to water of 0.2%. The points at larger heliocentric distance lie above the scaled observed trend in water production; however, at this distance, the assumption of collision-dominated excitation throughout the coma may be less valid, causing an over-estimate of the production rate. Moreover, a step-change in the power-law fit to HCN production versus heliocentric distance was also reported by Biver *et al.* (1998) around 2 AU pre-perihelion.

Table 3.3. Production rates for HCN in comet Hale-Bopp.

date	Δ (AU)	r (AU)	Q (mol/s)	σ_Q (mol/s)	log(Q)
Oct 07.4	3.010	2.820	9.82e+27	5.77e+26	27.99
Oct 26.8	3.050	2.580	1.52e+28	5.34e+26	28.18
Nov 04.8	3.050	2.480	1.34e+28	5.17e+26	28.13
Nov 13.3	3.030	2.370	1.12e+28	4.55e+26	28.05
Nov 24.2	2.980	2.240	8.87e+27	4.80e+26	27.95
Dec 23.3	2.690	1.870	1.30e+28	6.68e+26	28.11
Jan 03.2	2.540	1.730	5.37e+27	4.57e+26	27.73
Jan 13.2	2.370	1.610	7.06e+27	3.84e+26	27.85
Jan 24.5	2.170	1.470	9.22e+27	4.57e+26	27.96
Feb 02.7	1.990	1.360	1.27e+28	4.93e+26	28.10
Mar 11	1.370	0.989	1.32e+28	2.68e+26	28.12
Mar 20	1.320	0.940	2.10e+28	3.02e+26	28.32
Mar 23	1.320	0.929	1.55e+28	2.86e+26	28.19
Mar 24	1.320	0.926	2.08e+28	2.20e+26	28.32
Mar 30	1.340	0.915	2.38e+28	3.06e+26	28.38
Apr 03	1.370	0.915	2.00e+28	8.64e+26	28.30
Apr 09	1.430	0.925	2.17e+28	4.89e+26	28.34
Apr 20	1.590	0.974	2.14e+28	1.09e+27	28.33
Apr 21	1.600	0.980	2.04e+28	6.21e+26	28.31
Apr 22	1.620	0.987	2.55e+28	6.85e+26	28.41
Apr 26	1.690	1.020	2.35e+28	9.63e+26	28.37
Apr 27	1.700	1.020	1.66e+28	8.50e+26	28.22
May 12	1.960	1.160	1.38e+28	4.00e+26	28.14
May 18	2.060	1.230	1.59e+28	5.38e+26	28.20
May 20	2.090	1.250	1.75e+28	5.45e+26	28.24
May 23	2.140	1.280	1.48e+28	6.89e+26	28.17
May 30	2.240	1.360	1.65e+28	7.59e+26	28.22
Jun 09	2.380	1.490	1.48e+28	5.53e+26	28.17
Jun 11	2.410	1.510	1.18e+28	6.92e+26	28.07
Jun 16	2.470	1.570	9.35e+27	5.47e+26	27.97
Jun 23	2.550	1.660	1.48e+28	7.75e+26	28.17

Notes: Q indicates HCN production rate in mol s^{-1}, with uncertainty σ_Q.

3.5 Conclusions

We have monitored HCN via its J=1-0 rotational transition in a mapping campaign which spanned nine months and nearly 2 AU of heliocentric distance. The observed HCN distributions over this time are consistent with its sublimation from the nucleus as a parent molecule, with few large spatial asymmetries apparent in the maps. The spectral lines consistently differ from the expected line profile if the coma were the product solely of spherically symmetric outgassing at a constant velocity. We find better agreement between the data and models which allow for a power-law velocity, with a narrow range of initial velocities and exponents which represent the data equally well. On two dates which display the most symmetric emission, the model lines well represent the line shape and distribution of emission throughout the map with an initial velocity of ~ 0.5 km s^{-1}, and an exponent of $\alpha \sim 0.14$, in the power-law of equation 3.1. These parameters differ slightly from those found using the same power-law for comet Levy (Ge 1993): $V_0 = 0.3$ and $\alpha \sim 0.15$. However, comet Hale-Bopp was considerably more productive than comet Levy, which is consistent with higher outflow velocities (Tacconi-Garman 1989). Small asymmetries appear in both the map and spectra of March 11 and 20, although the line anomalies are greater on March 11, as are the best-fit values of α. We suggest that coma structures on scales comparable to, or below, the beam resolution will cause the velocity model to favor power-laws with larger exponents.

Using a constant fractional population in J=1, equal to the thermal population at the temperature given by Biver *et al.* (1998): $T = 103\ r_h^{-1.1}$, we compute a gas production rate of 2×10^{28} molecules s^{-1} of HCN at 1 AU, or an abundance of 0.2% relative to H_2O. These values are consistent with those derived by other observers, as well as with the relative abundance of HCN in other comets (Ge 1993; Bockelée-Morvan *et al.* 1984; Womack, Stern, & Festou 1997; Crovisier *et al.* 1990; Lis *et al.* 1997; Lis *et al.* 1998).

Chapter 4

HCO^+ Imaging of Comet Hale-Bopp

4.1 Introduction

The 1997 apparition of comet Hale-Bopp presented an unprecedented opportunity to study a large, highly productive comet in the inner solar system. The early discovery allowed for careful observation plans, many of which resulted in new cometary molecular detections. Among these new cometary detections in comet Hale-Bopp was that of the molecular ion HCO^+ through its J=1-0 rotational transition at 89.189 GHz (Veal *et al.* 1997). Spectral line maps of this ion at the Five College Radio Astronomy Observatory (FCRAO), made to follow up the discovery, revealed an intensity distribution that was dramatically different from that of neutral molecules (Lovell *et al.* 1997). This chapter summarizes the results of a three-month observing campaign to map HCO^+ in comet Hale-Bopp.

4.2 Observations

All observations were performed with the FCRAO 14-m radome-enclosed telescope in New Salem, Massachusetts, with the same instrumentation and techniques described in Chapters 2 and 3. The HCO^+ J=1-0 rotational transition at 89.18852 GHz was observed in comet Hale-Bopp during a period from March 10 to June 20, 1997, which includes both perigee ($\Delta = 1.3$ AU) and perihelion ($r = 0.91$ AU). All HCO^+ maps were obtained by frequency-switching with a 6 MHz offset. The comet was sampled by the 60″ beams of the array at 25″ intervals, half the beam spacing in the rows of Figure 1.1.

Table 4.1. Log of FCRAO HCO^+ mapping observations.

UT date 1997	Δ (AU)	r (AU)	ϕ_{ph} (deg)	PA (deg)	T_{sys} (K)	Conv. (km)	eff. beam (km)	(″)
10 Mar	1.378	0.996	46.1	338.8	450	80,000	91,000	126
12 Mar	1.360	0.982	46.9	341.8	430	80,000	90,700	127
†13 Mar	1.344	0.970	47.6	345.1	460	80,000	90,500	129
21 Mar	1.316	0.936	49.0	359.0	460	80,000	89,800	132
23 Mar	1.315	0.929	49.1	3.6	420	80,000	89,600	133
25 Mar	1.318	0.923	49.1	8.2	520	80,000	89,500	134
27 Mar	1.323	0.919	48.9	13.0	450	80,000	89,400	134
28 Mar	1.327	0.917	48.7	15.3	490	80,000	89,400	134
03 Apr	1.367	0.915	47.0	29.1	500	80,000	89,400	135
07 Apr	1.406	0.920	45.2	37.6	460	80,000	89,500	134
08 Apr	1.418	0.922	44.7	39.5	420	80,000	89,500	134
10 Apr	1.442	0.928	43.6	43.4	410	80,000	89,600	133
16 Apr	1.525	0.952	40.0	53.9	460	80,000	90,100	130
20 Apr	1.586	0.974	37.4	60.3	500	80,000	90,500	128
26 Apr	1.690	1.019	33.0	69.8	450	80,000	91,500	124
05 May	1.839	1.092	27.7	81.7	440	80,000	93,000	117
11 May	1.941	1.151	24.3	90.2	470	100,000	112,000	134
17 May	2.041	1.215	21.3	99.2	570	100,000	113,000	128
21 May	2.121	1.271	19.2	107.2	650	100,000	114,000	124
23 May	2.153	1.294	18.5	110.6	520	100,000	115,000	122
31 May	2.258	1.376	16.3	123.0	630	100,000	117,000	117
†03 Jun	2.315	1.424	15.4	130.5	520	100,000	118,000	114
†07 Jun	2.369	1.473	14.7	138.2	520	100,000	119,000	111
†14 Jun	2.458	1.560	13.9	151.7	520	100,000	121,000	107

† denotes two-day average

† denotes two-day average; Δ and r_h are the geocentric and heliocentric distances, respectively; ϕ_{ph} is the phase angle; PA is the astronomical position angle of the tail-vector, as computed in the ephemeris; T_{sys} is a typical mid-elevation system temperature. The observed spectra were convolved with a Gaussian beam, indicated in column 7, to yield the effective resolution given at the right.

The first observations of HCO^+ were made as a test on March 10, 1997, to assess the detectability of the J=1-0 line with our facilities. After confirmation that the line was detected at the nucleus position in the test observation, we proceeded to make a half-beam (Nyquist) sampled map on March 12, 1997. Figure 4.1 shows the spectra from this map (left), displayed at half-beam intervals across the array, along with the contour map (right), assembled from the integrated intensity in the velocity interval {-2,5} km s^{-1}. It is readily apparent in Figure 4.1 that the emission is more extended than a single "footprint" of the array, and that the peak of emission occurs at a significant offset from the nucleus position (indicated by the cross). Thus, subsequent observations were made with four different pointing centers (a 2 by 2 map with the array), to cover an area approximately 8′by 8′.

A log of observations is presented in Table 4.1. Δ and r are the geocentric and heliocentric distance in astronomical units (AU), ϕ is the phase angle (sun-comet-observer), PA is the astronomical position angle of the tail vector (East of North, given in the ephemeris by D. Yeomans, JPL), and T_{sys} indicates a typical mid-elevation system temperature for the observing period. As described in section 2.2.2, the spectra are convolved with a Gaussian beam and re-sampled. From March 10—May 03, 1997, a convolution of 80,000 km was used, as noted in Table 4.1. Thereafter, a slightly larger value of 100,000 was used, with the resulting post-convolution resolution as shown (in both kilometers and arcseconds). Generally, the data are averaged together as a block of observations on a single day (or fraction thereof); however, if the integration time was short or the quality of the data was low, observations on adjacent days are averaged together. Dates for which such an average is created are indicated by the cross † in the left column of Table 4.1.

A comprehensive set of maps of the integrated HCO^+ line area is presented in Figures 4.2–4.4. In these maps, as in all that follow, the Sun is to the left of the

Table 4.2. Peak HCO^+ map positions and values.

Date	x offset km	y offset km	x ″	y ″	peak mK km s^{-1}	σ_{peak}
Mar 12	-100,000	-60,000	-137	-82	356	16
Mar 13-14	0	40,000	0	55	305	23
Mar 15	0	-60,000	0	-82	278	23
Mar 21	-120,000	-40,000	-164	-54	400	17
Mar 23	-100,000	-20,000	-137	-27	456	23
Mar 25	-140,000	-40,000	-192	-54	517	38
Mar 27	-100,000	-40,000	-137	-54	523	25
Mar 28a	-80,000	0	-109	0	497	32
Mar 28b	-100,000	-20,000	-137	-27	610	38
Mar 28	-80,000	-20,000	-109	-27	523	25
Apr 03a	-140,000	20,000	-192	28	498	35
Apr 03b	-80,000	-40,000	-109	-54	525	36
Apr 03	-100,000	0	-137	0	476	24
Apr 07	-140,000	-20,000	-192	-27	629	27
Apr 08	-80,000	40,000	-109	55	322	30
Apr 10	-60,000	-60,000	-82	-82	431	24
Apr 16	-100,000	0	-137	0	395	29
Apr 20	-100,000	-80,000	-137	-109	330	23
Apr 26	-120,000	20,000	-164	28	305	27
Apr 27	20,000	-40,000	28	-54	329	35
May 05	-60,000	40,000	-82	55	320	27
May 07	-120,000	-140,000	-164	-192	196	27
May 11	-75,000	25,000	-102	34	348	13
May 17	-50,000	0	-68	0	218	22
May 21	-25,000	25,000	-33	34	163	15
May 22	-350,000	250,000	-482	345	228	53
May 23	-75,000	0	-102	0	160	17
May 24	-125,000	-50,000	-171	-68	157	7
May 31	-50,000	-100,000	-68	-137	119	21
Jun 03	75,000	-175,000	103	-240	99	22
Jun 04	-150,000	275,000	-206	379	122	24
Jun 07-08	-50,000	-100,000	-68	-137	104	15
Jun 14-15	-375,000	-400,000	-516	-551	274	37

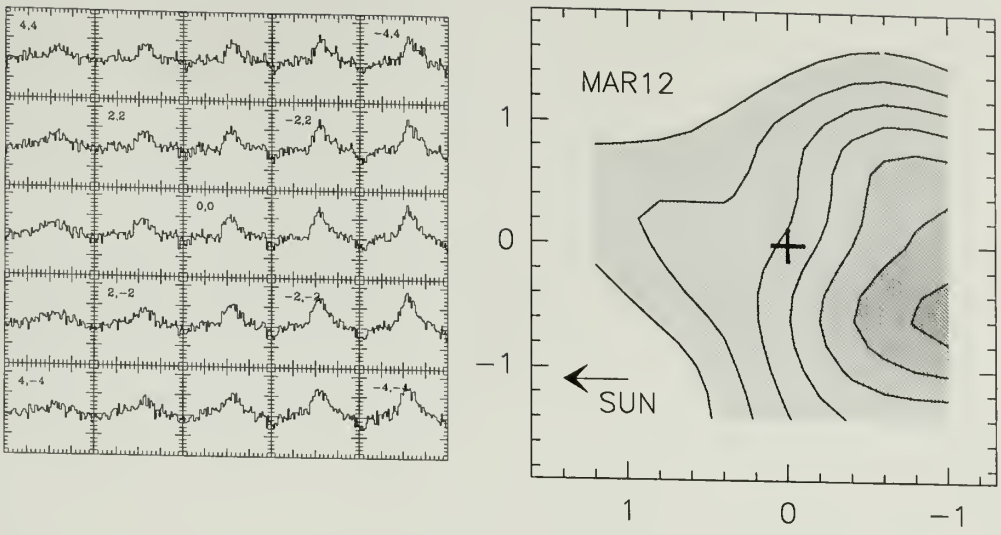

Figure 4.1. Spectra and integrated intensity map of HCO^+ on March 12, 1997, in comet Hale-Bopp. On the left is a grid of smoothed spectra at half-beam (40,000 km) intervals; on the right is the integrated intensity map, with axes in units of 100,000 km. The integrated intensity is computed in the interval -2 km s^{-1} to 5 km $s^{-1}$and contoured at 40 mK km s^{-1}, beginning at 100 mK km s^{-1}. The projected direction to the Sun is indicated by the arrow, and the tracked position of the nucleus by the cross.

figure, with the projected tail vector along the negative x-axis. The position of the nucleus (the cross) and North (an arrow) are indicated to facilitate comparison with images in other coordinate systems. Table 4.2 indicates the value of the peak in the emission, along with the position of the peak in map coordinates. The peak integrated line intensity in mK km s^{-1} occurs at the coordinates shown (in both km and arcsec), where X is along the solar-antisolar axis of the comet (sunward is positive), and Y is the perpendicular offset. From both the images of Figures 4.2–4.4 and the data in Table 4.2, it can be seen that the peak in emission is generally anti-sunward, though not necessarily along the Sun-comet axis. A collection of peak spectra are displayed in Figure 4.5.

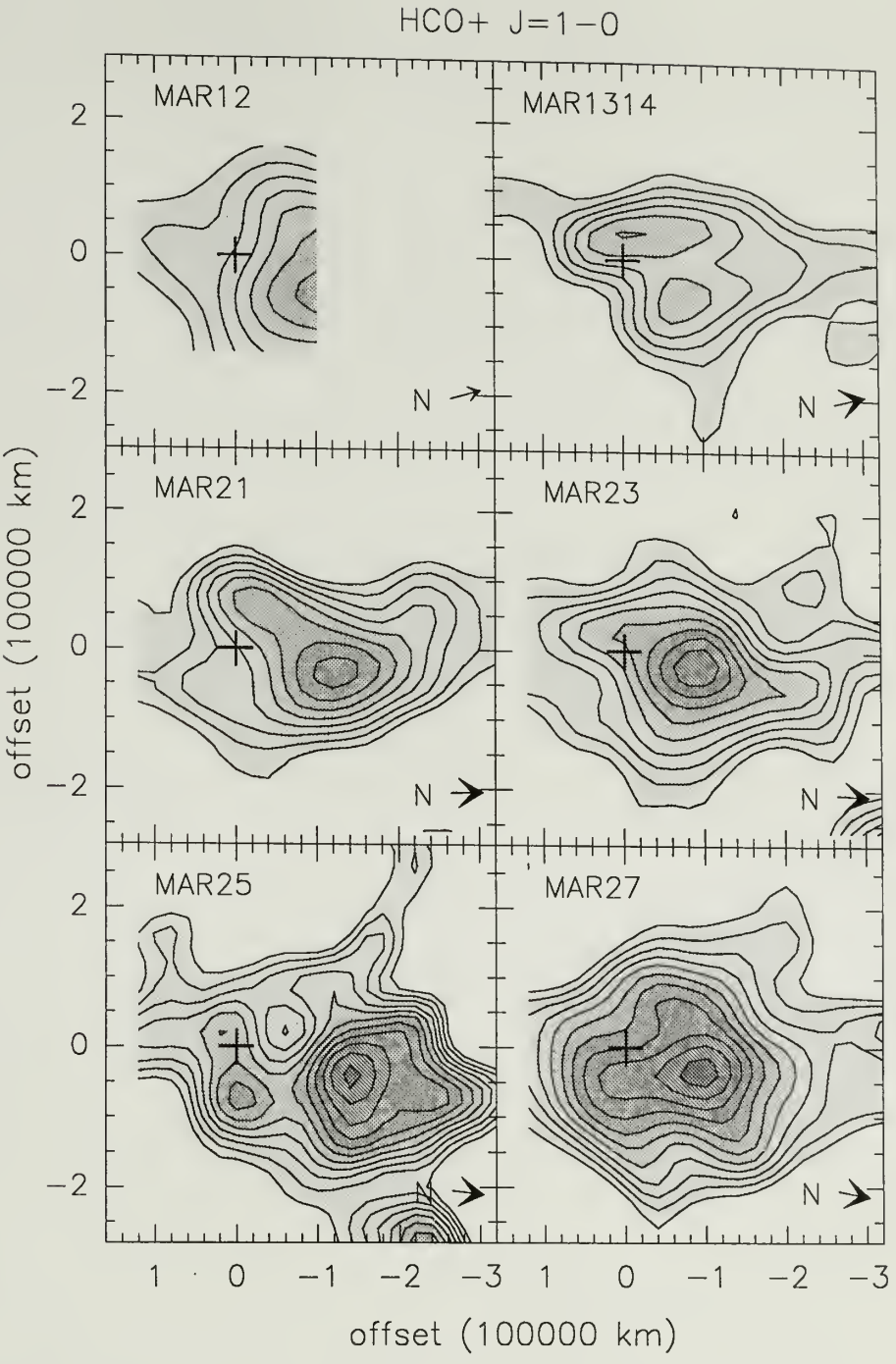

Figure 4.2. Contour maps of HCO^+ integrated intensity in comet Hale-Bopp for March 12–27, 1997. The axes are in units of 100,000 km from the nucleus position (indicated by the cross), with the Sun to the left (positive x), and north in the direction of the arrow. The beam size for this set of images is approximately 58,000 km. The contour interval is 50 mK km s^{-1}, beginning at 80 mK km s^{-1}.

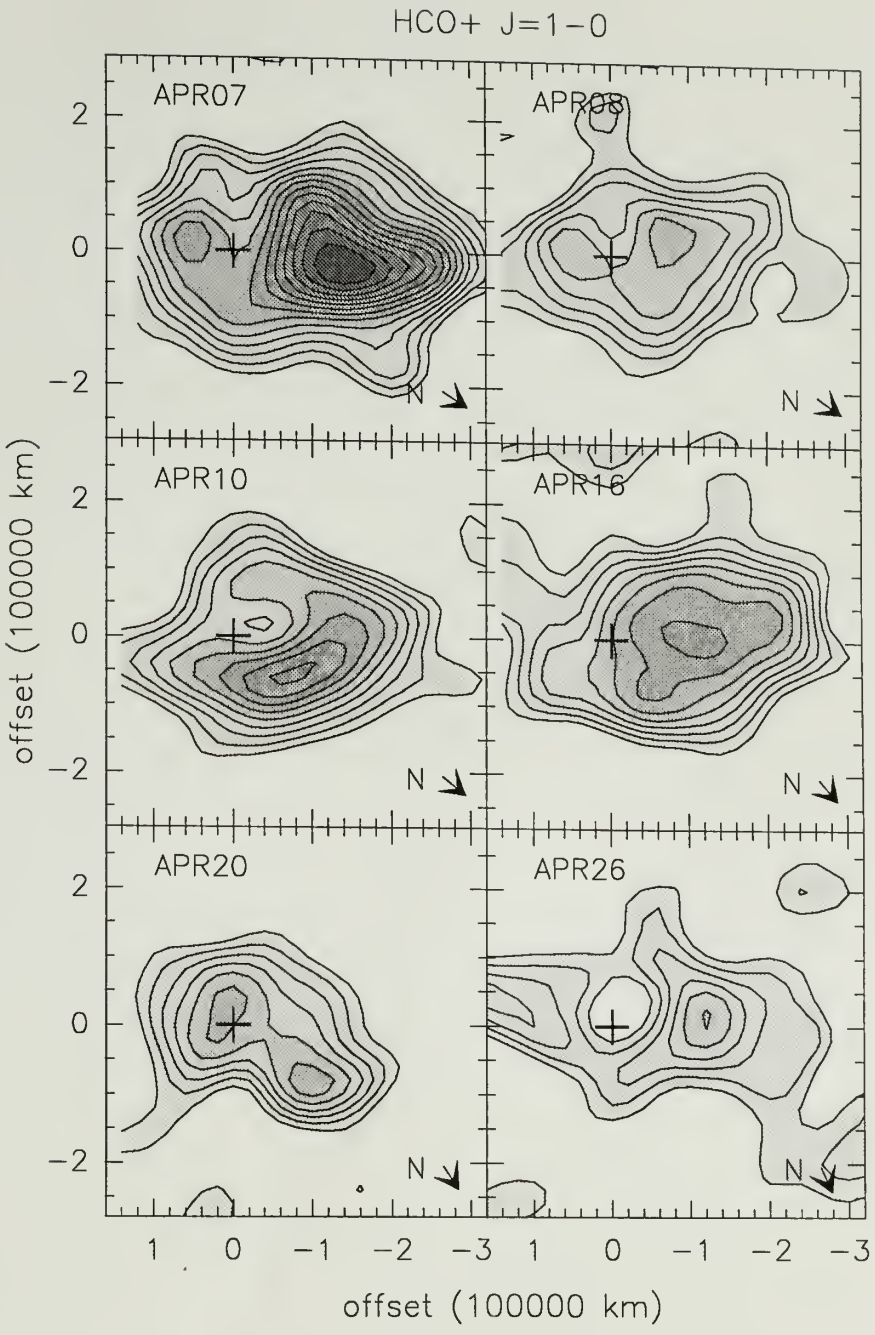

Figure 4.3. Contours of HCO^+ integrated intensity in comet Hale-Bopp for April 7–26, 1997. Orientation, symbols and contours are as in Figure 4.2. Note the distinctive shift in morphology from a strong single peak on April 7 to a more diffuse ring/horseshoe structure on April 8. A ring-like morphology is also evident April 10 and 26.

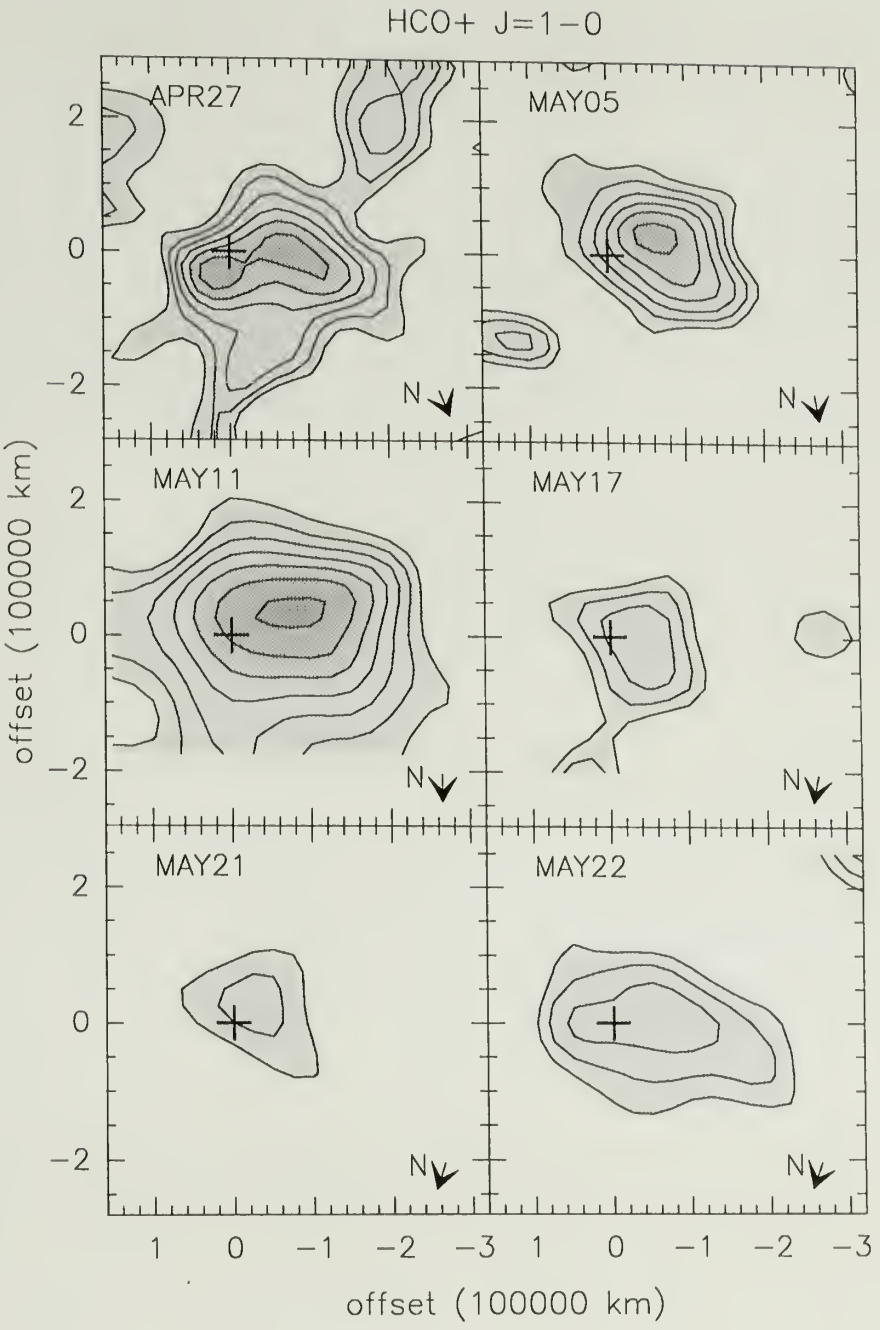

Figure 4.4. Contours of HCO^+ integrated intensity in comet Hale-Bopp for April 27–May 22, 1997. Orientation, symbols and contours are as in Figure 4.2. Due to the larger geocentric and heliocentric distances, the emission is weaker than that seen in Figures 4.2–4.3; however, there are notable exceptions, as on May 11 and 22. Observations beyond this date lack the sufficient signal-to-noise ratio to make individual maps.

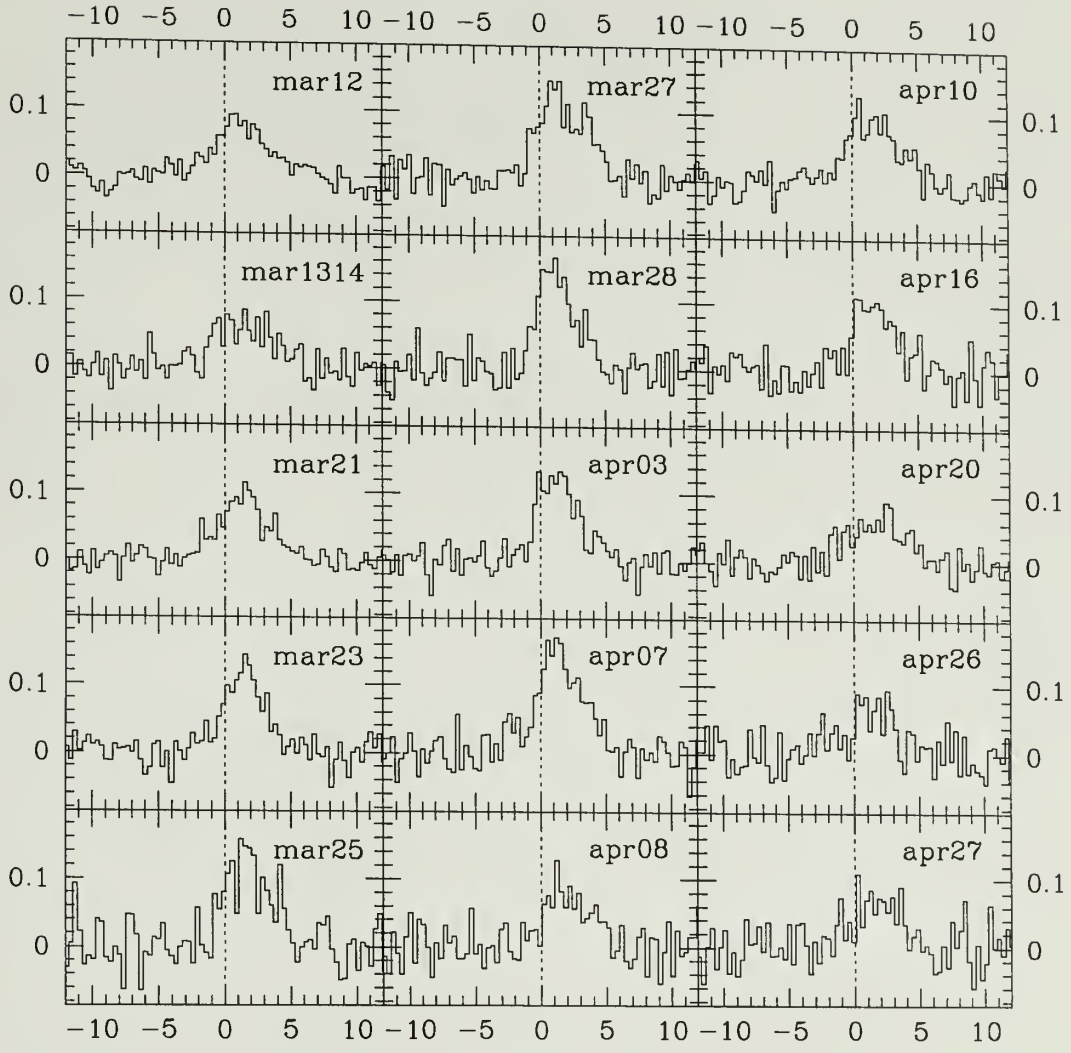

Figure 4.5. HCO^+ spectra for the peak map position (indicated in Table 4.2) for each observed date between March 12 and April 27, 1997. Spectra have been averaged over 5 velocity channels, to give a resulting velocity resolution of ~ 0.3 km s^{-1}.

4.3 Results

4.3.1 Spatial extent and offset in peak emission

Several features are apparent upon inspection of the maps in Figures 4.2–4.4. First, in contrast to neutral species observed with the same instrumentation (*cf.* Chapter 3), the HCO^+ ion is detected over a wide spatial region, and the emission peaks in the tailward direction, rather than on the nucleus position. This result is in agreement with the mapping observations of the HCO^+ J=3-2 observations made on March 15, 1997 (Womack *et al.* 1998). Figure 4.6 shows a comparison between maps of HCO^+ and the neutral molecule HCN (for which the observed J=1-0 transition has similar excitation requirements to the J=1-0 HCO^+ line) obtained on adjacent days, to illustrate the difference in extent and peak position of the emission. The ion emission is detected over an area approximately 4 times that of the neutral emission, and its peak is obviously shifted anti-sunward. All significant HCO^+ J=1-0 emission is contained within a rectangular area spanning 100,000 km sunward to 300,000 km tailward along the Sun-comet axis, and $\pm$ 150,000 km in the perpendicular direction.

4.3.2 Broad, redshifted spectral lines

Figure 4.7 shows the striking differences between the spectra of a neutral molecule (HCN) and HCO^+. The lower panel is an HCN spectrum on the nucleus position, taken March 24, 1997, and processed in the same manner as the HCO^+ spectra. The line is < 3 km s^{-1} wide, and very slightly blue-shifted with respect to the cometocentric velocity. The center panel is the HCO^+ spectrum at the nucleus position, taken March 27, 1997. The line appears slightly wider, and obviously redshifted with respect to the motion of the comet. The top panel is the HCO^+ spectrum at the peak of emission, in the tailward direction (Table 4.2). The line is 4–5 km s^{-1} wide, and redshifted more than 1 km s^{-1}.

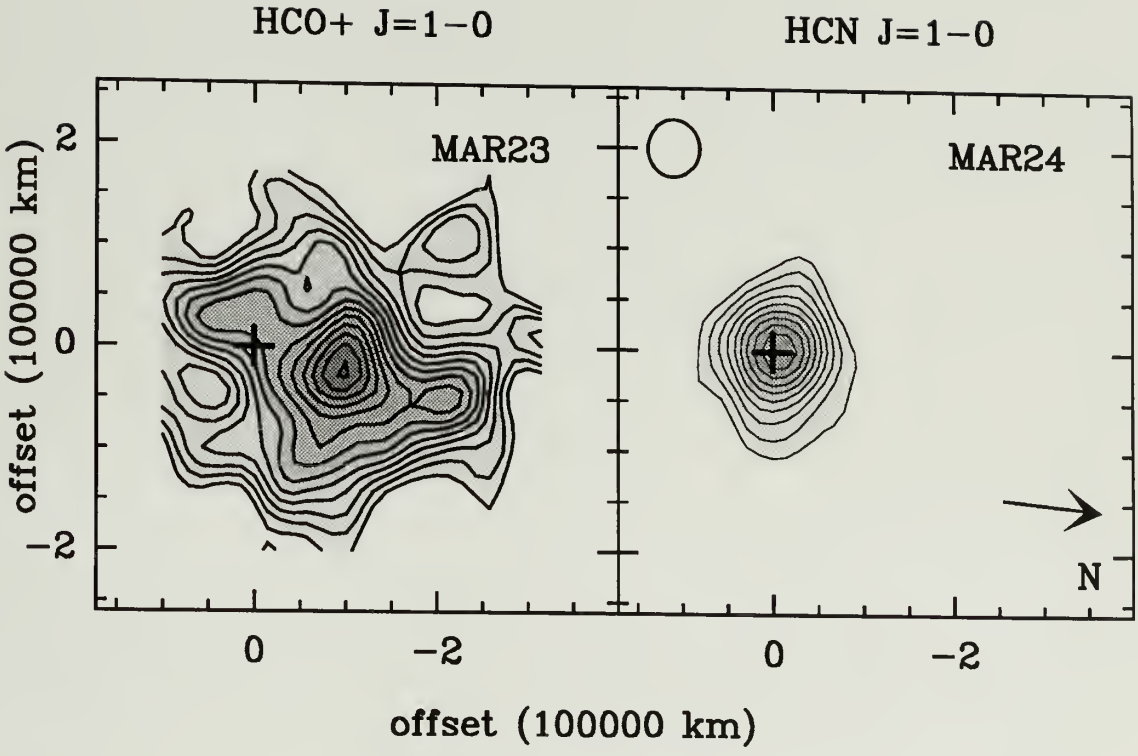

Figure 4.6. Comparison of maps of HCO^+ J=1-0 and HCN J=1-0 emission obtained on successive days (March 23 and 24, 1997), at the same spatial resolution. Although these molecules have similar excitation requirements, and are observed with the same size beam, the ion emission is observable over a larger area and offset from the nucleus position. Symbols are as in Figure 4.2.

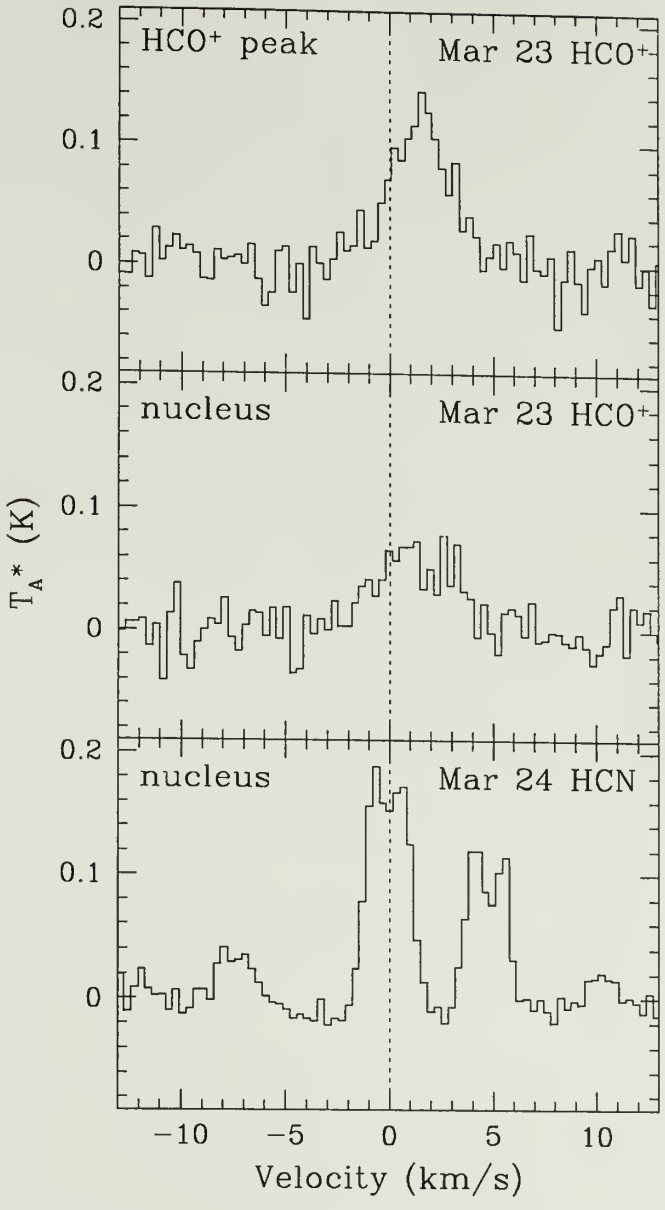

Figure 4.7. Sample spectra to illustrate the distinctive nature of HCO^+ spectra in comet Hale-Bopp. The HCO^+ spectrum from the nucleus position (top) is compared to the peak spectrum in the map for March 23 (center). Both spectra are redshifted from the nominal velocity of the comet (0 km/s), with a stronger, broader, more redshifted line at the peak. The spectrum for March 24, HCN J=1-0 emission (bottom) is shown for comparison.

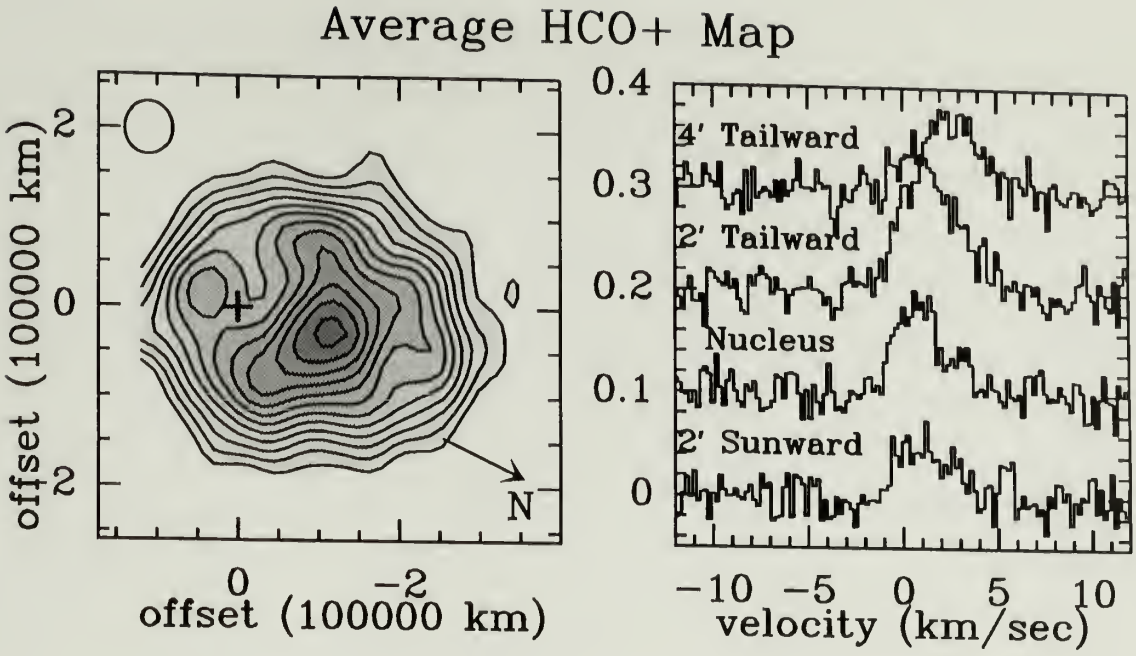

Figure 4.8. (Left) Averaged maps for all observations between March 23 and April 10. (Right) Spectra for points along the Sun-tail axis of the comet for the averaged map. Note the increase in strength and redshift with distance along the tail.

Clearly, the HCO^+ spectral lines are broad and redshifted with respect to the nucleus velocity. Furthermore, the amount of the redshift increases as one observes progressively farther down the tail of the comet. This can be seen in the averaged spectra in Figure 4.8, where spectra are shown at regular intervals along the Sun-tail axis of the comet. Here the averaged spectra and maps are processed as outlined in section 2.2.2.

4.3.3 Time and spatial variability

It is also apparent from Figures 4.2–4.4 that the HCO^+ emission is time-variable. On March 28 and April 3, 1997, our closest observation dates to perihelion, there was sufficient signal-to-noise in the data to permit the data to be subdivided into two maps: one pre-transit and one and post-transit. These maps (Figure 4.9, top and bottom), which are separated in time by approximately 4

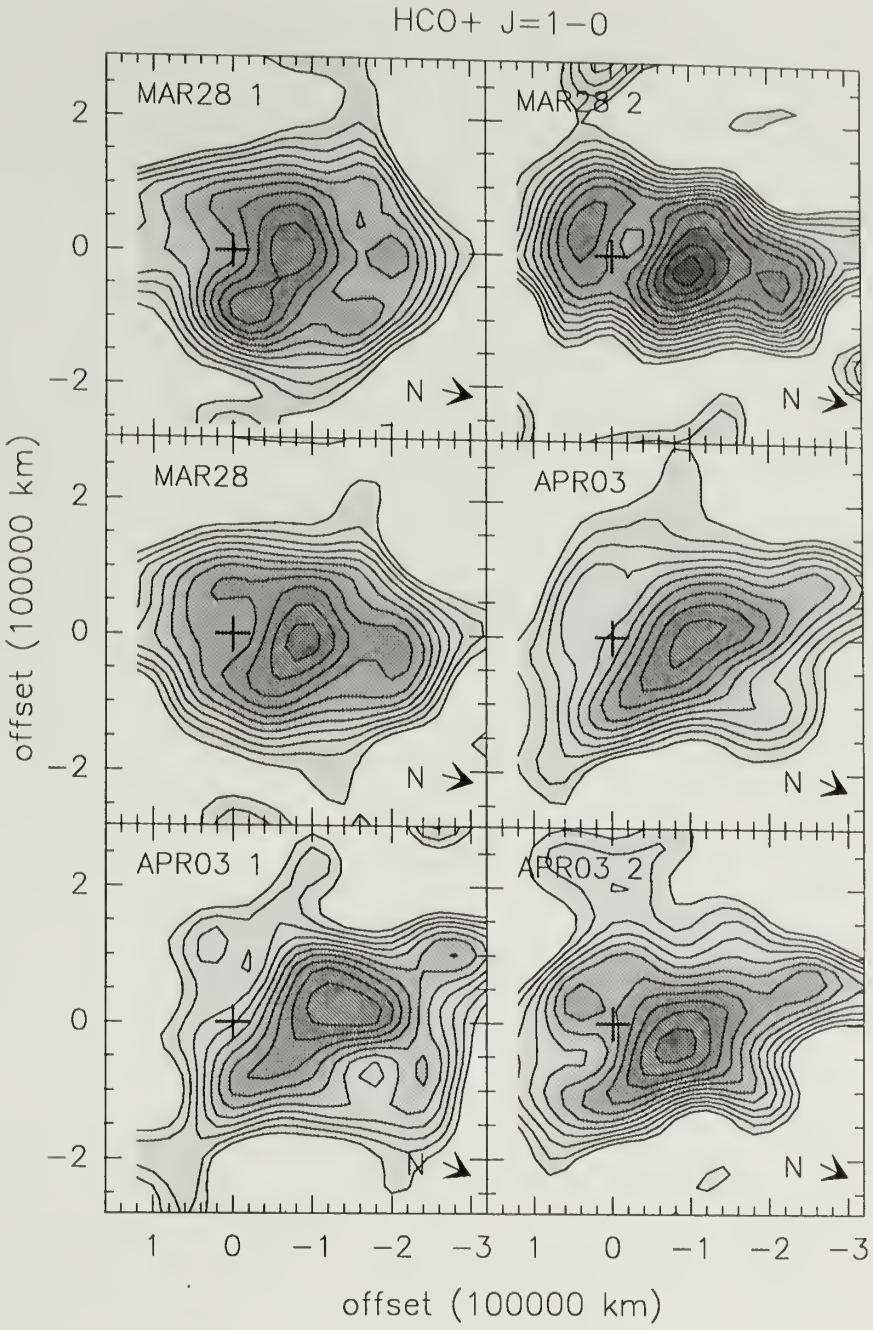

Figure 4.9. HCO^+ integrated intensity in comet Hale-Bopp for March 28 and April 3, 1997, our closest data to perihelion. Orientation, symbols and contours are as in Figure 4.2. In the two center panels, the maps represent the average over the entire indicated date. Above and below, the maps are separated into (1) pre- and (2) post-transit portions (separated by approximately 4 hours), to illustrate how rapidly spatial variations occur.

hours, along with the full-day averaged maps (Figure 4.9, center) illustrate how the character of the mapped emission changes on time scales of less than a few hours. Significant intensity changes also occur between maps on adjacent observing days, as is nicely illustrated by the April maps (Figure 4.3). These maps also demonstrate two distinctive morphologies that are apparent in the HCO^+ emission: a single strong peak which is displaced antisunward (as on April 7 and 16), and more diffuse emission spread out into a ring or horseshoe shape (as on April 8, 10, or 26), with a local minimum on the nucleus position. In both cases, the emission towards the nucleus is weaker than is observed elsewhere in the coma.

In order to evaluate the typical bulk behavior of HCO^+ emission from the comet, we have assembled two long-term averaged maps, one between March 13 and March 28 (3 weeks pre-perihelion), and another between April 3 and April 26 (post-perihelion). The resulting integrated intensity maps are shown in Figure 4.10, along with the corresponding intensity profile along the Sun-tail axis. The spectral line emission in the average maps follows the basic trends identified in the maps on individual days: the HCO^+ emission is clearly stronger in the antisolar direction, and there is a depression in the map at the position of the nucleus. The similarities between these two independent maps illustrate that, although the emission may fluctuate rapidly, the smoothed overall structure of the HCO^+ J=1-0 emission in comet Hale-Bopp remained steady over more than six weeks.

4.4 Discussion

In order to interpret the observational results, we must investigate the physical processes at work in the coma of comet Hale-Bopp. Here, we address briefly the process of ion-molecule reactions in the coma, along with acceleration of ions.

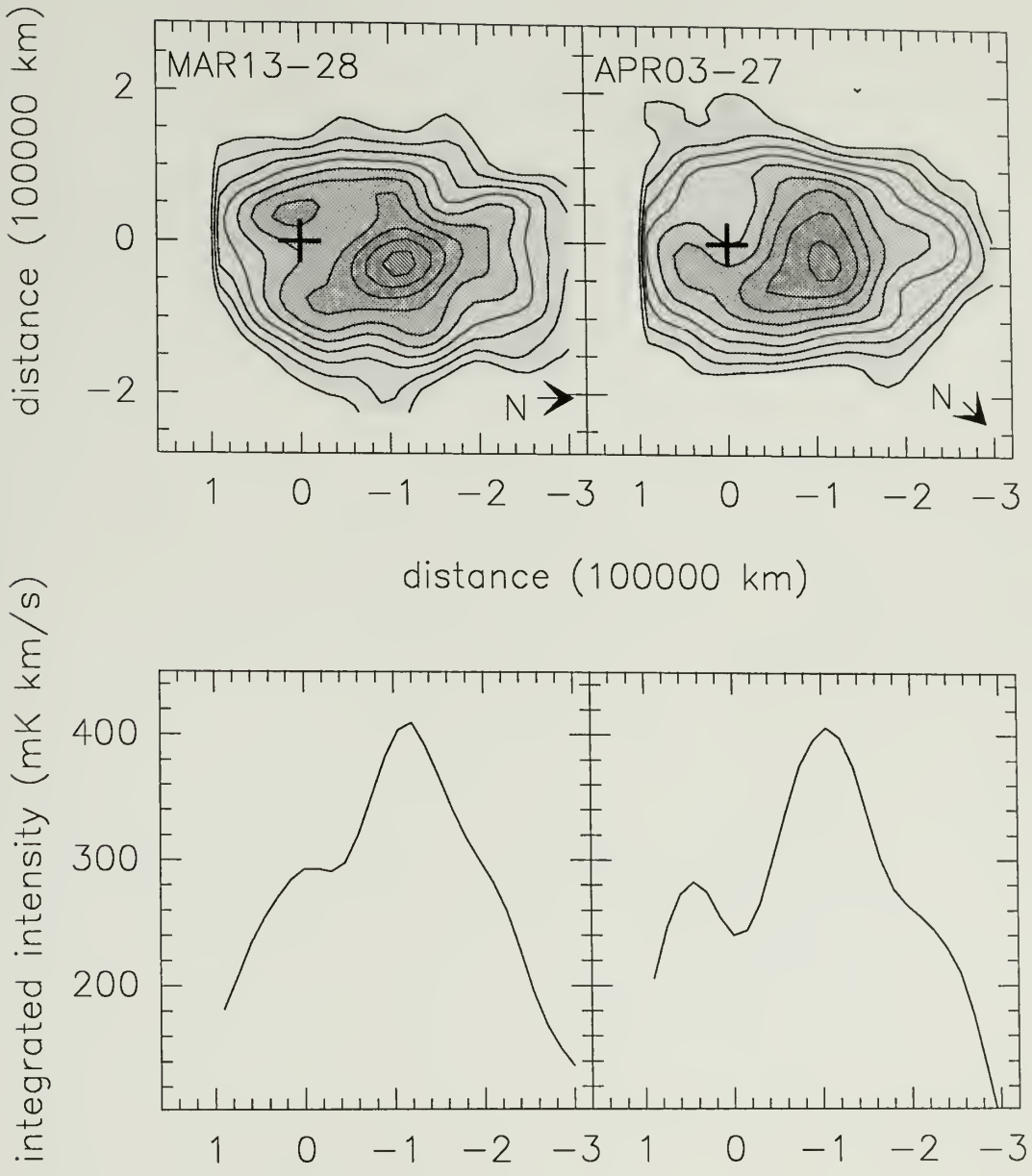

Figure 4.10. (Top) Averaged maps for all observations in March (left) and April (right). The positional coordinates are given as linear offsets from the nucleus, in units of 100,000 km. The Sun is to the left (the positive x direction), the average vector north is indicated by the pointer, and the nucleus ephemeris position is indicated by the cross. The lowest contour occurs at 80 mK km s^{-1}, which corresponds to the typical 4 standard deviation detection level. The contour interval above this level is 40 mK km s^{-1}, corresponding to approximately two standard deviations. (Bottom) Spatial integrated intensity profiles for points along the Sun-tail axis of the comet for the above maps.

4.4.1 Acceleration of ions

Once HCO^+ is formed in the coma, it should be accelerated in the antisolar direction through its interaction with the solar wind magnetic field streaming past the comet. Thus, the basic redshift of the HCO^+ lines and the asymmetric distribution of its emission are probably best accounted for by this process. A complete model of this phenomenon would involve a full MHD treatment of the interaction of the solar wind with the cometary plasma (such as that for H_2O^+ by Gombosi *et al.* 1998), which is beyond the scope of this work. For the purposes of a quantitative analysis of our maps, we adopt a simple approximation in which ions are formed and then accelerated tailward with a fixed acceleration.

4.4.2 Reaction pathway

HCO^+ ions could be formed in a cometary coma through a number of paths. The most likely scenario is the formation of HCO^+ via ion-molecule reactions. CO is first photoionized to give CO^+, which then reacts with water to produce HCO^+ (Huebner and Giguere, 1980):

$$CO^+ + H_2O \rightarrow HCO^+ + OH. \tag{4.1}$$

Given the results of Huebner and Giguere's models and our present understanding that H_2O and CO are the most abundant molecules in the comet's coma, this path is the most plausible and we have adopted it for our model simulation. Upon formation, HCO^+ may be photodestroyed, destroyed by reactions with neutrals, or lost through recombination with electrons.

For the purpose of our simple model, we adopt the above formation scheme and specify: (1) the lifetime of CO against photoionization; (2) the lifetime for CO^+ against reaction with water in the coma as a function of distance from the nucleus; and (3) a lifetime for HCO^+ against destruction by all processes. For CO

photoionization, we adopt a quiet-sun lifetime of 3×10^6 seconds at a heliocentric distance of 1 AU (Schmidt *et al.* 1988). The lifetime of a CO^+ ion due to reaction with H_2O (equation 4.1) is deduced from the rate constant k, which should be variable within the coma since the water density decreases in proportion to the inverse square of the distance from the nucleus. We adopt a gas production rate (Q) of 10^{31} s^{-1} for the comet and a water outflow velocity (v) of 1 km s^{-1} to derive the reaction time scale, τ, in seconds, at distance r in the coma (reaction constants from Schmidt et al 1988):

$$\tau(r) = \frac{1}{k}\frac{4\pi v r^2}{Q} = 1.4 \times 10^4 \left(\frac{r(km)}{10^5}\right)^2. \quad (4.2)$$

The destruction of HCO^+ ions is obviously critical to the interpretation of the HCO^+ maps. Our initial assumption for this work has been to adopt a single lifetime for HCO^+ destruction and examine the consequences for a range from long values, which would be appropriate to photodestruction, to very short values which might pertain for recombination in the inner coma.

We have computed the effects of both the HCO^+ formation and its acceleration using a Monte Carlo approach which is described in Appendix A. The left panel of Figure 4.11 shows the results of model computations, assuming a tailward acceleration of 10 cm s^{-2} and a relatively long lifetime of 10^5 seconds for HCO^+ after its formation. In this panel, HCO^+ ions are not preferentially destroyed in the inner coma. Qualitatively, the model shows the general features of a large, asymmetric brightness distribution for HCO^+, and model spectral lines show the redshifted behavior that is observed. Quantitatively, a simpler approach is to compare the mean velocity of spectra along different lines of sight in the coma. We show, in Figure 4.12, a comparison of the mean velocity of model spectra with the observed mean velocity derived from the pre-perihelion averaged map of Figure 4.10. Model predictions for an acceleration of 5, 10, and 20 cm s^{-2}

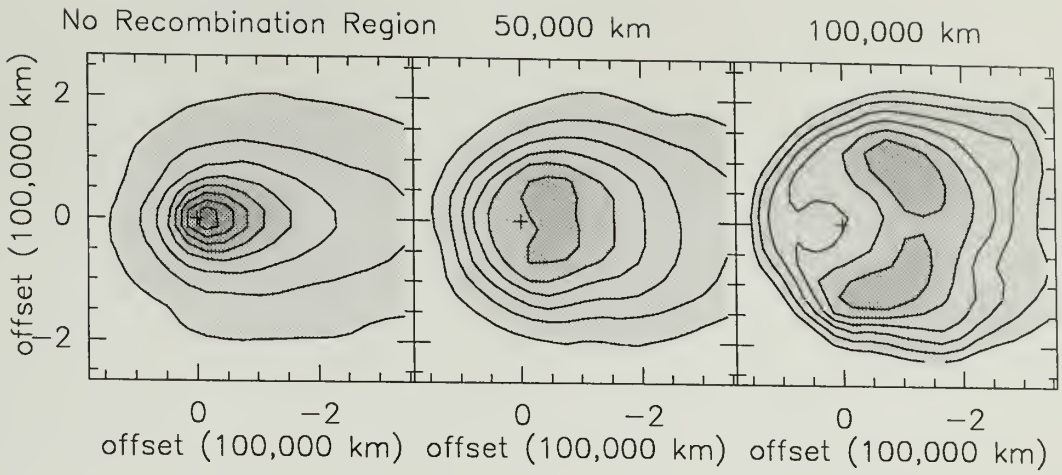

Figure 4.11. Model maps of HCO^+ integrated intensity in comet Hale-Bopp, using a value of 10 cm s^{-2} for acceleration, and 3 different recombination regions. These models allow for enhanced HCO^+ recombination within the given distance from the nucleus, as discussed in section 4.4.3. The left image has no recombination region, the center image includes recombination inside a radius of 50,000 km, and the right image inside 100,000 km.

are presented (solid lines) and the comparison to the actual measurements suggests that an acceleration on the order of 10 cm s^{-2} is sufficient to explain the magnitude of the redshift and its variation in the coma. This value is about a factor of 10 smaller than values derived from observations of the tail of comet Halley by Celnik and Schmidt-Kaler (1987) and Scherb *et al.* (1990), presumably due to the increase in mass loading of the solar wind in this high production rate comet. In addition, the velocity within the map appears to require greater values of acceleration as ions proceed along the tail (Figure 4.12).

4.4.3 Suppression of HCO^+in the inner coma

Although the left panel of Figure 4.11 shows the basic asymmetry seen in our maps, the peak emission in this model is not offset from the nucleus position by the amount that is typically observed. Moreover, this model cannot reproduce the local minimum towards the nucleus on the maps (as illustrated by the profiles of

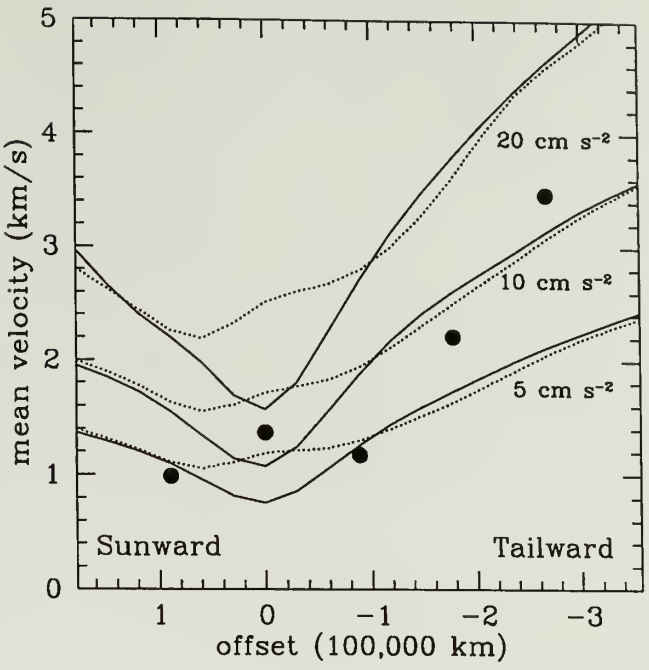

Figure 4.12. Mean velocity of spectral lines along the Sun-tail axis of the comet. The data (filled circles) are derived from the averaged map of Figure 3. Solid lines show the result of models which consider only acceleration of the ions. Dashed lines illustrate models which include a 50,000 km recombination region. Note that the models which include recombination better reproduce the observed behavior of the comet.

Figure 4.10), or the "ring" features that are observed on some days. Thus, we have attempted to refine the basic model in order to achieve better agreement with the maps. We consider a region within the inner coma where recombination of HCO^+ and CO^+ occurs at a high rate. Such a model is consistent with the observed behavior of comet Halley, where Eberhardt and Krankowsky (1995) found a large increase in the electron recombination rate for ions in the inner coma between about 5,000—10,000 km from the nucleus. The discontinuity in comet Halley occurs outside of the contact surface and corresponds to the point in the coma where cooling of electrons through collisions with neutrals becomes ineffective. Since the contact surface radius should scale with the comet's production rate (Ip

and Axford, 1990), we expect that the effect seen in comet Halley should occur approximately 10 times farther out in Hale-Bopp, or approximately 50,000—100,000 km from the nucleus.

Figure 4.11 shows the results of calculations which assume that HCO^+ cannot survive within 50,000 (center panel) and 100,000 km (right panel) of the nucleus. The maps which include a recombination region display not only the offset in the peak of the HCO^+ emission, but also the "ring" behavior that is observed. Thus, we conclude that the appearance of the observed HCO^+ maps requires the existence of such a region. Additional evidence in favor of a large recombination region is seen in the dashed curves of Figure 4.12, which show the predicted mean velocity of lines in the presence of a 50,000 km recombination region. The disappearance of HCO^+ molecules from the inner coma in these models primarily affects molecules at low velocities near the nucleus. The result is that the mean velocity towards the nucleus position is greater than that observed in models with no recombination region. The predicted variation of mean velocity with position in the coma is in good agreement with the observed behavior of the comet and appears to confirm our conclusion that the appearance of the maps is the result of missing HCO^+ ions in the inner coma.

4.4.4 Ion-molecule chemistry

To examine the ion-molecule and photo-chemistry of cometary comae we used the chemistry model of Bergin & Langer (1997), adapted for cometary conditions (Lovell *et al.* 1998a; Irvine *et al.* 1998). The network contains a total of 73 atomic and molecular species linked through 812 reactions. The rate coefficients for ion-molecule and neutral-neutral reactions are taken from (Millar, Farquhar, & Willacy 1997), supplemented by photo-reactions (assuming unattenuated solar radiation and a quiet sun) and electron impact dissociative reactions from (Huebner, Keady, & Lyon 1992) and (Schmidt *et al.* 1988). In this adaptation of

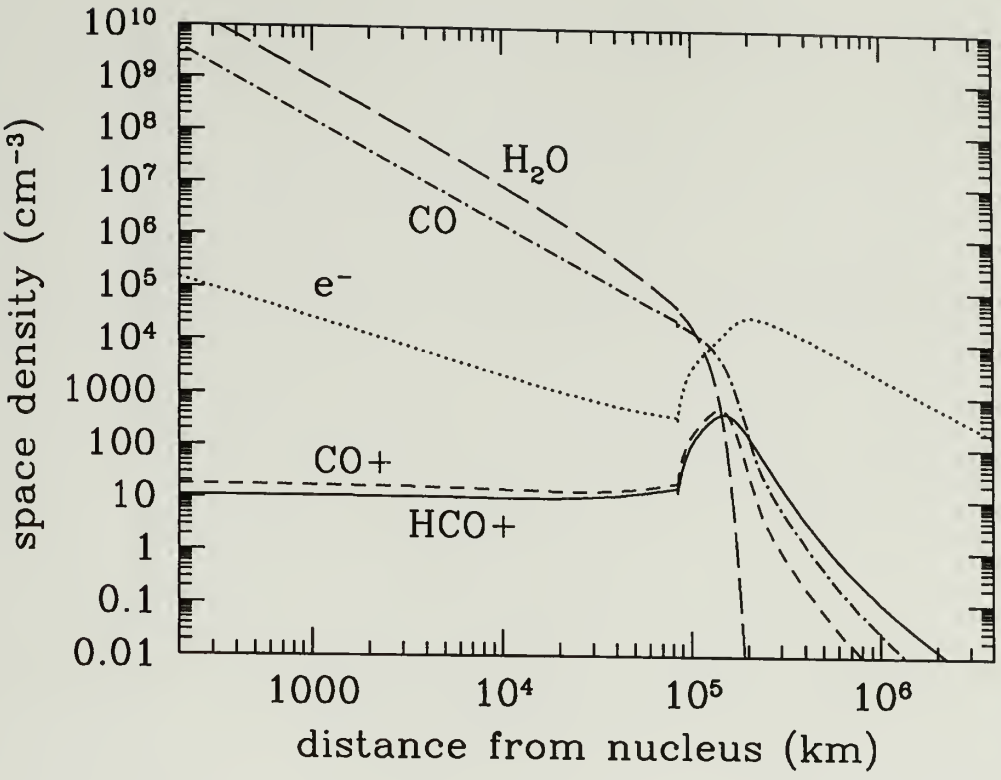

Figure 4.13. Space density profiles from the chemical model for HCO^+, CO^+, CO, H_2O and e^- versus distance from the nucleus, for a discontinuity in electron temperature occurring at 8×10^4 km from the nucleus.

the model, the water density decreases as the inverse square of the distance from the nucleus, and the time-dependence of the chemical abundances is related to the distance through the outflow velocity (assumed to be constant at 1 km s^{-1}).

The model allows for a two-component electron temperature (T_e) distribution, based on the results of the Giotto NMS experiment (Eberhardt & Krankowsky 1995). In the inner coma, the high density of H_2O collisionally cools hot photo-electrons and maintains T_e at the neutral gas kinetic temperature ($\sim$ 100 K). However, in the outer coma, beyond the thermal collisionopause, the lower water density cannot thermalize the photo-electrons and T_e rises rapidly to high values ($\approx 10^4$ K). The electron temperature has a strong effect on ion-neutral

reaction rates ($\propto T^{-0.5}$ or steeper (Eberhardt & Krankowsky 1995)). Thus, in the inner coma where the high H_2O density keeps T_e low, the recombination rate is very high. On the other hand, in the outer coma where collisions cannot cool the electrons, the reaction rates are depressed significantly, allowing HCO^+ and other ions to grow in abundance. This mechanism, as discussed by (Häberli, Balsiger, & Geiss 1995), is likely responsible for the low-abundance region proposed here and by Lovell *et al.* (1998b) to reproduce the minimum in HCO^+ abundance observed toward the nucleus. As both the transition region and T_e inside and outside the thermal collisionopause are input variables in the calculation, we use the model to examine the physical location of the transition and the approximate scale of the temperature variation. An example of calculated space density profiles of HCO^+ and related species is given in Figure 4.13. The density of the ions remains approximately constant out to the thermal collisionopause, outside of which it exhibits a sharp increase and then a rapid falloff.

A line-of-sight integration of the number of molecules in the model convolved with the telescope beam yields a column density for each position, which can be compared to the observed values in our maps. However, in order to interpret the observed integrated line intensities, the excitation of HCO^+ must be addressed. In the outer coma, we expect that radiative excitation of HCO^+ via its fundamental vibrational bands (Mauclaire *et al.* 1995) will dominate (Crovisier 1987b). We calculate, following (Bockelée-Morvan & Crovisier 1985), that this process (with a band excitation rate of 1.3×10^{-3} s^{-1}) will yield a J=1 fractional population of 33%. Collisional cross-sections of ions are uncertain; however, (Xie & Mumma 1992) suggest ion-water cross-sections are at least $10^{-12}cm^{-2}$. Assuming collisional cross-sections in the range $\sigma = 5 \times 10^{-14} - 10^{-12}cm^{-2}$, and a kinetic temperature law after Crovisier (Crovisier 1987b), collisions with water will cease to dominate over radiative excitation between 6×10^4 and 3×10^5 km from the nucleus in the

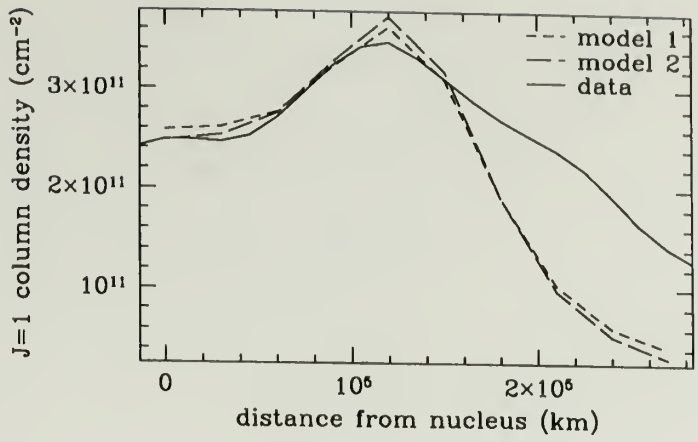

Figure 4.14. Model column density profile for HCO^+ J=1 state, versus distance from the nucleus. In the two excitation models, radiative excitation begins to dominate over collisions with water at a distance of 3×10^5 km (model 1, corresponding to $\sigma = 10^{-12}$), or 6×10^4 km (model 2, $\sigma = 5 \times 10^{-14}$). In both cases, for $T_e \approx 5 \times 10^4$ K outside the collisionopause, and a transition around 80,000 km, the behavior qualitatively reproduces the primary peak in the observed March profile (from Figure 4.10).

coma of comet Hale-Bopp. In Figure 4.14, we compare the predicted column density in the J=1 state with the observed March profile, under two assumptions of excitation.

Considering only the location of the primary peak in the observed profiles, there is good agreement between data and model with a total water production $Q_{H_2O} = 10^{31}$ s^{-1} at 1 AU, initial relative abundances detailed in Table 4.3, an inner coma value of T_e=100 K, and a transition at 80,000 km to a value of T_e= 5×10^4 K. This transition occurs further from the nucleus than in comet Halley (Häberli, Balsiger, & Geiss 1995), which is consistent with the higher gas production in comet Hale-Bopp (Cravens 1991), (Gombosi 1998). The spatial profile of the predicted HCO^+ column density (Figure 4.14) reproduces the strong offset peak seen in Figure 4.10 for March. However, the model column density

Table 4.3. Initial Abundances

Species	Abundance	Species	Abundance
CO	15.0	CH_4	0.7
CO_2	4.0	C_2H_2	0.6
CH_3OH	2.0	NH_3	0.5
H_2CO	1.0	HCN	0.2

Relative to water (=100).

Abundances after Biver *et al.*(1997), Irvine *et al.*(1998).

declines more rapidly with distance from the nucleus than does the observed profile. We attribute this to the fact that this model simulates chemistry only, neglecting solar wind interactions which accelerate the HCO^+ in the anti-solar direction (thus shallowing this curve).

4.5 Conclusions

We have mapped the HCO^+ emission from comet Hale-Bopp and identified several key aspects of its behavior. The HCO^+ emission is extended tailward and it is significantly redshifted compared to neutral species. Maps on many days illustrate that the HCO^+ emission is significantly time variable to the shortest time scales that we were able to probe (several hours).

The general features of the HCO^+ emission may be understood by a simple model in which its formation via ion-molecule reactions is followed by acceleration due to interaction with the solar wind magnetic field. The acceleration of the ions accounts for the basic asymmetry in the emission and for the observed redshifts of the lines. However, the maps also appear to require a region of enhanced HCO^+ destruction within approximately 50,000–100,000 km of the nucleus. The scale of this region corresponds quantitatively to a region of enhanced recombination in the inner coma of comet Halley, as observed by instruments on the Giotto spacecraft (*c.f.* Eberhardt and Krankowsky 1995). This region occurs at an important transition in the coma between gas that is dominated by cold cometary species and

gas in which solar wind and cometary ions are being mixed. Thus, given the time variability of both the solar wind and the gas production from the comet, it is not surprising to find significant time variability in the behavior of the HCO^+ emission.

Chapter 5

Conclusions

We have employed a millimeter-wave array receiver to obtain spectral line observations of comets Hyakutake and Hale-Bopp. The observations were conducted over extended periods of time surrounding the close approaches of these comets to Earth, providing rare opportunities to map cometary molecular emission over time. Monitoring these comets with spectral line mapping allowed probing of a variety of cometary structures, and provided an excellent basis for constraining coma physics and chemistry.

These two comets were contrasting in many ways. Comet Hyakutake was small in size, yet fairly active. Its orbit placed it very near to the Earth, allowing a close look at the inner coma during a time when anomalous activity was taking place. Comet Hale-Bopp, on the other hand, was quite large and extremely active. Its orbital parameters allowed early detection and more strategic observing plans; however, it remained fairly distant during the apparition.

Observations of comet Hyakutake revealed asymmetries in the spectral lines as well as in the mapped distribution of HCN in the coma. The proximity of the comet to the Earth allowed the scale of the telescope beam to resolve the comet: such resolved observations of the inner coma at millimeter wavelengths, particularly during the time when a unique outburst or splitting event occurred, are unprecedented. This close look at a cometary coma constrained the coma models in several ways. First, we found that some dispersion in velocity above the nominal thermal dispersion is required in order to account for the observed line shapes. The best explanation appears to be a variation in outflow velocity within

the coma with distance from the nucleus. Second, we found, in agreement with other observers, that the distribution of the emission from the inner coma suggests that collisions dominate over solar radiation in the excitation of HCN, over a large region. This can either be explained with a higher collision cross-section for HCN-H_2O reactions (significantly in excess of the values discussed in Appendix B), or by allowing additional excitation by another collisional partner, such as electrons (the role of which has been discussed by Xie & Mumma (1992) for H_2O excitation, and proposed by Lis *et al.* (1997) to account for HCN observations). Third, we found that our observations were strongly influenced by the unique events that occurred in the inner coma of comet Hyakutake just prior to perigee. We detected significant asymmetries in the coma morphology, noticeable velocity asymmetries in the spectral lines, and a decrease in the production rate, all associated with an outburst or nuclear splitting which occurred on or around March 21, 1996.

The comet Hale-Bopp HCN observations confirmed that our model must include a variation in outflow velocity within the coma. A power-law approximation to the outflow velocity was employed for models of both comets, with similar results for observations at the same heliocentric distance. Comet Hale-Bopp was considerably more productive than Hyakutake, resulting in a slightly higher best-fit initial velocity in the power-law (0.5 km s^{-1} for Hale-Bopp versus 0.4 km s^{-1} for Hyakutake). The exponent in the power-law is similar between both these comets ($\sim 0.1 - 0.15$), which is in good agreement with observations of comet Levy (Ge 1993).

Due to the difference in geocentric distance, comet Hale-Bopp was observed in a considerably larger field-of-view (a factor of ten higher than the observed scale in comet Hyakutake). At this scale, not surprisingly, many fewer spatial asymmetries were observed. In one case, where spatial asymmetries are apparent in the HCN map of comet Hale-Bopp, there is apparently a broader range of velocities present

in the coma than is seen when no spatial asymmetries are noted. This is true in both comets: the spatially asymmetric emission maps also display asymmetric spectral lines, and appear to require different coma kinematics in the symmetric models. Rather than using a symmetric model to characterize clearly asymmetric structures, the results are improved by allowing local emission enhancements in the model. Furthermore, in agreement with the Hyakutake observations, we find that the data are better characterized by models which assume a constant population in the J=1 state than by those which assume a two-component excitation model. For both comets, better agreement with results of other observers, as well as with relative HCN abundances in other comets, are obtained in the thermally-excited limit. This suggests that the collision-dominated region in the coma is much larger than expected from HCN - H_2O collisions (with cross-sections of order 5×10^{-15}) alone. Under the assumption of collision-dominated excitation, the relative abundance of HCN to H_2O in both comets is of order 0.2%.

Observations of the ion HCO^+ in comet Hale-Bopp provided a unique view of an ionized coma constituent. Millimeter-wave observations of an ion such as HCO^+ require more extended coverage than do observations of neutral species, and suggest that resolved single-pixel observations at the nucleus position may significantly underestimate the peak of emission. The morphology of the emission maps, as well as the broad, redshifted spectral lines, can yield insight into the physics and chemistry of ions in the coma. We suggest that HCO^+ is formed via ion-molecule reactions, but that it is immediately destroyed in the inner coma, where the density is high. Once the density becomes lower, approximately where the electron temperature undergoes a sharp temperature transition, the HCO^+ molecules can survive, and accelerate in the anti-sunward direction due to interactions with the solar wind and magnetic field. This picture is consistent with the current state of understanding of the plasma environment around comets

(Häberli *et al.* 1997; Eberhardt & Krankowsky 1995; Cravens 1991; Huebner *et al.* 1991; Gombosi 1998).

This work has illustrated the power of spatially-resolved millimeter-wave mapping of cometary comae as an effective multi-dimensional constraint for model simulations. The millimeter-wave array receiver provided both the efficiency and mapping speed necessary to detect these dynamic objects, which were close enough for observation only over short periods of time. Such observations provide a means of quantifying molecular emission over the entire coma: not only in line strength, but also in coma kinematics. As the sensitivity of this type of receiver improves, observations may be made of less productive or more distant comets, and allow comparison to be made with the extraordinary comets Hyakutake and Hale-Bopp. For example, the work of Combi (1996) suggests that lower gas production rates yield coma outflow velocities which much more closely approximate a constant. Mapping observations which include comets with total gas production $Q < 10^{29}$ mol s^{-1} could provide a basis for assessing the dependence of the outflow velocity variations on Q. Furthermore, the total gas production may influence the abundance or distribution of HCO^+, and sampling this ion in a lower-production comet, observing where we now know the peak in emission is likely to lie, can yield valuable insight into how ion processes vary from comet to comet. By providing the first series of fully sampled millimeter-wave maps of molecular species in cometary comae, this work will aid in planning new cometary observations and will provide a basis for comparison in future millimeter-wave studies of comets.

Appendix A

The Model

A.1 Introduction

We employ a Monte Carlo model (*cf.* Combi & Delsemme, 1980) to simulate the production, destruction, and motion of parent molecules in the cometary coma. To match a given grid of spectra, the model simulates a spherically expanding distribution of molecules, and tracks their evolution in time and space in order to produce spectra at each grid point. This appendix outlines the model assumptions, input parameters, and computation technique.

A.2 Physical Parameters

Model spectra are computed using the same grid points and spectral resolution as those output by the convolutions described in sections 2.3 and 3.1. The beam size θ in the model computations is equal to the effective post-convolution beam size, given in Table 2.3 for comet Hyakutake and Table 3.1 for comet Hale-Bopp. The resulting simulated spectra depend on three types of model parameters, as summarized in Table A.1. The observing geometry is specified in three parameters: phase angle ϕ, geocentric distance Δ, and heliocentric distance r_h. The observed grid is described by the number of points, the spacing, and the effective beam size. The number of spectrometer channels and spectral resolution are chosen to match those of the convolved data. Three physical parameters, which depend on r_h (but are otherwise constant) are the outflow velocity V_{exp}, the photodissociation rate β, and the coma temperature T. These physical parameters affect the major features of the predicted gas distribution: the shape of the spectral lines and the extent of

Table A.1. Model Parameters for comets Hyakutake and Hale-Bopp

Observational parameters	
Phase angle	ϕ
Geocentric distance	Δ
Heliocentric distance	r_h
Effective half-power beam width	θ
Grid spacing	$d\theta$
Number of grid points in x, y	N_x,N_y
Velocity channel width	dv
Number of velocity channels	N_v
Physical assumptions	
Outflow velocity[1]	$V_{exp} = V_0\ (r/r_{\rm nuc})^{\alpha}$
Photodissociation rate[2]	$\beta = 1.3 \times 10^{-5}\ r_h^{-2}$
Hale-Bopp Temperature[3]	$T = 103\ r_h^{-1.10}$
Hyakutake Temperature[4] (at r_h=1 AU)	$T = 75$
Excitation parameters	
Collisional population	$f_{\rm coll}$
Radiative population	$f_{\rm rad}$
Transition distance	$r_{\rm tran}$

[1]Ge, 1993. [2] Crovisier, 1994.
[3] Biver *et al.*, 1998. [4] Lis *et al.*, 1997.

molecular emission. The spectral line widths are strongly dependent on V_{exp}, with secondary thermal broadening according to T. The extent of emission in the map is determined by V_{exp} and β, both of which influence the amount of time a molecule is observable in the beam. V_{exp} and T also influence the density of molecules in the inner coma and the velocities at which they collide. As outlined in Appendix B, the excitation of the molecule in the coma is parameterized using two regions, with a smooth transition between them at cometocentric distance $r_{\rm tran}$. Close to the nucleus, a collision-dominated region exists where thermal excitation at temperature T determines the population of molecules $f_{\rm coll}$ in the upper state of the observed transition. In the outer coma, where low densities render collisions inefficient, the population $f_{\rm rad}$ is determined by solar radiative excitation alone.

A.3 Computation of the Model

Given the physical parameters outlined in Table A.1, a large statistical sample of molecules is created and tracked throughout the coma. Molecules which persist until the end of the simulation, the "observation time," are sampled onto the specified grid to create the model spectra and map. The weighted contribution of each molecule is determined with respect to the two spatial coordinates in the map, as well as each velocity channel in the spectra.

A.3.1 Time

The lifetime of the parent molecule, equal to the inverse of the photodissociation rate, $\tau = 1/\beta$, is used to determine the interval over which molecules are generated. This interval $t_{\rm obs}$ must be sufficiently long to sample the distribution of parent molecules which decay exponentially under photodissociation. Thus, we select $t_{\rm obs} = 10\tau$. A molecule is generated at a random time t_1 such that $0 < t_1 < t_{\rm obs}$. The destruction time is given by (Tacconi-Garman, 1989) $t_2 = t_1 + \tau \ln(\psi)$, where ψ is a random number between 0

and 1. If $t_2 > t_{\rm obs}$, then the molecule has not yet decayed at the time of observation, and the velocity and position are computed and weighted into the appropriate velocity channels and grid points.

A.3.2 Distribution of molecules

Each molecule leaves the nucleus in a random direction, specified by the angles θ and ϕ. Using a rectangular coordinate system $\{x, y, z\}$, the azimuthal angle ϕ (the angle about the z-axis) is randomly distributed such that $0 < \phi < 2\pi$. θ, measured towards the x-axis away from the z-axis, is randomly distributed such that $-1 < \cos(\theta) < 1$. From these angles, the components of the velocity along the axes $\{x, y, z\}$ are computed:

$$V_x = V_{\rm exp}\sin(\theta)\cos(\phi)\ ;\ V_y = V_{\rm exp}\sin(\theta)\sin(\phi)\ ;\ V_z = V_{\rm exp}\cos(\theta). \qquad \text{(A.1)}$$

In the constant-velocity case, the observed position along the ith axis is simply the product of the velocity V_i and the time t_1 since creation of the molecule: $x_i = V_i t_1$. These cometocentric positions and velocities must then be projected onto the observation plane in order to assemble the simulated map.

A.3.3 Spatial weighting

The position at which the molecule is observed in the map depends upon the observed phase angle:

$$x_{\rm obs} = x\cos(\phi_{\rm ph}) + z\sin(\phi_{\rm ph})\ ;\ y_{\rm obs} = y. \qquad \text{(A.2)}$$

For each grid point x_i, y_j, we determine the linear offset (in angular units in the map) of the molecule $\Delta x = x_{\rm obs} - x_i$, $\Delta y = y_{\rm obs} - y_j$, and apply a spatial weighting function of

$$b_{ij} = \exp\left(-4\ln 2\left(\frac{(\Delta x)^2 + (\Delta y)^2}{\theta^2}\right)\right), \qquad \text{(A.3)}$$

where θ is the effective post-convolution beam resolution.

The computed positions are also employed in determining the prevailing excitation mechanism, as described in Appendix B. In this simple excitation model, the cometocentric distance $R = \sqrt{(x^2 + y^2 + z^2)}$ determines the population in the upper state of the observed molecular line:

$$f_u = f_{\rm coll} + \frac{(f_{\rm rad} - f_{\rm coll})}{1 + (\frac{r_{\rm tran}}{R})^2}, \tag{A.4}$$

where $r_{\rm tran}$ is the cometocentric distance at which the transition occurs between the populations in the collision-dominated ($f_{\rm coll}$) and radiation-dominated ($f_{\rm rad}$) limits.

A.3.4 Spectral weighting

Once the location of the molecule with respect to each beam (i, j), is determined, the model spectra can be computed. The doppler shift with respect to the observer depends only on the velocity components along the line of sight, projected according to the phase angle $\phi_{\rm ph}$ of observation:

$$V_{\rm doppler} = V_x \sin(\phi_{\rm ph}) - V_z \cos(\phi_{\rm ph}), \tag{A.5}$$

where the observer lies in the x-z plane. This velocity, with a small amount of thermal broadening at temperature T, determines which velocity channels detect the molecule. We account for thermal broadening of the line with a half-width at half-maximum using (Townes & Schawlow, 1975)

$$\Delta v_{\rm th} = \sqrt{\frac{2kT \ln 2}{m}}, \tag{A.6}$$

where m is the mass of the molecule. This width is applied as a Gaussian weighting to the kth velocity channel in each spectrum:

$$g_k = \frac{\sqrt{\frac{4 \ln 2}{\pi}}\, dv}{\Delta v_{\rm th}} \exp\left(-4 \ln 2 \left(\frac{v_k}{\Delta v_{\rm th}}\right)^2\right). \tag{A.7}$$

The contribution of the molecule to each channel in the model spectrum is the product of this weight with the spatial weightings described above:

$$T_k^* = f_u \; g_k \; b_{ij}. \tag{A.8}$$

A.3.5 Final output

The spatial and spectral weightings are summed for N molecules in the simulation, yielding a single model spectrum (with N_v channels) for each grid point. The output spectrum is obtained by summing the contributions of each molecule, and dividing by the total number of molecules:

$$T_{ijk} = \frac{1}{N}\sum_{N} f_u \; g_k \; b_{ij}. \tag{A.9}$$

Integrated intensity values are computed as

$$dv \sum_{k} T_{ijk} = \frac{dv}{N} \sum_{N} f_u b_{ij}. \tag{A.10}$$

These quantities are unitless, as they are simply sums of weighting functions. In order to compare these model spectra and integrated intensities to the real data, they must be scaled to appropriate physical values.

A.4 Physical Interpretation of Results

Following the treatment of Schloerb *et al.* (1986), the integrated intensity of a transition can be expressed in terms of the upper-state column density $< N_u >$ averaged over the beam:

$$\int T_A^* dv = \eta_b \frac{c^3}{2k\nu^3} \frac{h\nu A_{ul}}{4\pi} < N_u >, \tag{A.11}$$

with the telescope beam efficiency η_b, frequency ν, Einstein spontaneous emission coefficient A_{ul}, and physical constants c, k, and h. In a Gaussian beam of half-power beam width θ, with a fraction f_b of molecules contained within the beam, this column density can be expressed as

$$< N_u >= N_u \frac{4 \ln 2}{\pi \Delta^2 \theta^2} f_b. \tag{A.12}$$

In this equation, Δ is the geocentric distance of the comet, and N_u is the total number of molecules in the upper state. This number is related to the production rate Q and the lifetime τ via the population f_u of the upper state:

$$N_u = f_u \tau Q. \tag{A.13}$$

Thus, the integrated intensity is

$$\int T_A^* dv = \frac{c^3}{2k\nu^3} \frac{h\nu A_{ul}}{4\pi\Delta^2} \frac{4\ln 2}{\pi\theta^2} \eta_b \tau Q f_b f_u. \tag{A.14}$$

In a single velocity channel k, the fraction of emission is

$$f_k = \frac{T_k dv}{\int T_A^* dv}, \tag{A.15}$$

with a velocity channel width of dv. Solving for the temperature of the individual channel and substituting in equation A.14 yields

$$T_k' = \frac{c^3}{2k\nu^3} \frac{h\nu A_{ul}}{4\pi\Delta^2} \frac{4\ln 2}{\pi\theta^2} \frac{\eta_b \tau Q}{dv} f_k f_b f_u. \tag{A.16}$$

The channels T_{ijk} in each model spectrum (i,j) contain the product $f_k f_b f_u$, which, integrated over all k yields $\sum_k T_{ijk} = f_b f_u$. Thus, the ratio between the observed integrated intensities and the model yield an estimate of the production rate Q. The data intensity is $\int T_A^* dv = \sum T_k' dv$, and the model intensity is obtained by summing equation A.10 over all k. Thus, the ratio of data to model is

$$\left(\frac{\sum T_k' dv}{\sum_k T_{ijk}} \right) = \frac{c^3}{2k\nu^3} \frac{h\nu A_{ul}}{4\pi\Delta^2} \frac{4\ln 2}{\pi\theta^2} \eta_b \tau Q. \tag{A.17}$$

Ideally, the ratio of the observed to the model intensity would be constant throughout the map; however, our signal-to-noise ratio is greatest at the nucleus position, so we select a portion of the coma for computing estimates of Q. We consider a rectangular region approximately three times the beam size, centered at the nucleus position. Over this range, we compute the value of the ratio in equation A.17 which minimizes the total χ^2. Recalling that the lifetime τ is the inverse of the photodissociation rate β:

$$Q = \left(\frac{\sum T_k' dv}{\sum_k T_{ijk}} \right) \frac{2k\nu^3}{c^3} \frac{4\pi\Delta^2}{h\nu A_{ul}} \frac{\pi\theta^2}{4\ln 2} \frac{\beta}{\eta_b}. \tag{A.18}$$

For HCN, we compute the integrated intensity only in the F=2-1 hyperfine component. Thus, to calculate Q from the HCN observations, we multiply the observed $\int T_A^* dv$ by a factor of 9/5, assuming the statistical weight ratio of 5:3:1 for the 3 components.

Appendix B

Excitation of Linear molecules in cometary comae

B.1 Introduction

In order to interpret spectroscopic observations of rotational lines, a model of molecular excitation must be employed. For linear molecules such as HCN and HCO^+, the main excitation mechanisms are thermal excitation via collisions, and solar excitation of the fundamental bands of vibration (Crovisier 1987b). Collisional excitation will dominate in the inner coma, where the density of gas is high. At 1 AU, H_2O is by far the most abundant species in the coma and is thus the most likely collisional partner for this study of comets Hale-Bopp and Hyakutake. Radiative excitation should dominate in the outer coma, where collisions become ineffective due to lower densities. In order to assess at what distance from the nucleus the transition from collisional to radiative excitation occurs, we first address both these types of excitation and common assumptions.

We employ several simplifying assumptions in order to model molecular excitation in the cometary coma. Excited vibrational states are assumed to be sparsely populated, such that their population is neglected. Similarly, we neglect fluorescence due to electronic excitation by solar UV radiation (Bockelée-Morvan *et al.* 1984). We also assume that in the radiatively excited region of the coma, fluorescence equilibrium has been reached, and that direct solar radiation is the dominant excitation mechanism (Crovisier & Encrenaz 1983). Finally, we assume that over the spatial scales observed in both comets, the observed rotational transitions are optically thin.

This appendix outlines the excitation mechanisms which affect the linear molecules observed in this study of comets Hyakutake and Hale-Bopp. Radiative excitation and collisional excitation are first considered separately. The two are then combined into a simple total excitation model.

B.2 Radiative excitation

The excitation due to solar blackbody radiation at a temperature $T_{\rm bb}$, subtending a solid angle $\Omega_{\rm bb}$, is characterized by the radiative excitation rate Crovisier & Encrenaz (1983)

$$g_{v'v''} = \frac{\Omega_{\rm bb}}{4\pi} A_{v'v''} [e^{hc\sigma_{v'v''}/kT_{\rm bb}} - 1]^{-1}, \tag{B.1}$$

where $\sigma_{v'v''}$ is the frequency of the transition from vibrational state v'' to v' in $\rm cm^{-1}$. Here, $T_{\rm bb} = 5770$ K and the solid angle subtended by the Sun from a distance of 1 AU is $\Omega_{\rm bb} = 6.8 \times 10^{-5}$, and $A_{v'v''}$ is the Einstein coefficient for spontaneous emission. In the literature, line strengths for the infrared bands are generally reported as intensities of absorption lines observed at 300 K (in km $\rm mol^{-1}$). When v' is the ground state, (Crovisier & Encrenaz 1983) define a "band spontaneous emission Einstein coefficient"

$$A_{v'v''} = 3.080 \times 10^{-8} \sigma^2_{v'v''} S, \tag{B.2}$$

where S is the total band strength in $\rm cm^{-2}$ $\rm atm^{-1}$.

Given the individual excitation rates $g_{v'v''}$, computed in equations B.1 and B.2, the effective band excitation rate g_e is the sum of the parallel (Σ–Σ stretching modes) and perpendicular (Π–Σ bending modes) excitation terms (Bockelée-Morvan & Crovisier 1985)

$$g_e = \Sigma g_{\parallel} + \frac{1}{2} \Sigma g_{\perp}. \tag{B.3}$$

For linear molecules, (Bockelée-Morvan & Crovisier 1985) present the population distribution of the rotational levels at fluorescence equilibrium, as a function of the

Table B.1. Parameters for fundamental vibrational bands of HCN

transition	σ cm^{-1}	g_e s^{-1}
ν_1	2097	1.3×10^{-7}
ν_2	712	8.8×10^{-5}
$2\nu_2$	1412	3.5×10^{-5}
ν_3	3311	3.3×10^{-4}

Transition frequencies σ are given by (Pugh & Rao 1976); excitation rates g_e are after (Bockelée-Morvan *et al.* 1984).

ratio of g_e to the Einstein coefficient A_{10} for spontaneous emission of the J=1-0 line.

At fluorescence equilibrium, the radiative excitation rate is a constant, leaving a constant population (in the upper state of the rotational transition) for all parts of the coma which are dominated by the solar excitation as discussed above. The only physical quantity which can affect the population of the upper state under these conditions is Ω_{BB}, which depends on r_h, the heliocentric distance. Thus, the ratio $\log(g_e/A_{10})$ can be expressed as

$$\log\left(\frac{1}{r_h^2}\frac{g_e}{A_{ul}}\right), \tag{B.4}$$

since all of the terms in equation B.3 have the same dependence on r_h.

B.2.1 HCN Fundamental Vibrational Bands

The prevailing excitation mechanism for HCN is solar radiative excitation of the ν_2, $2\nu_2$, and ν_3 infrared vibrational bands (Bockelée-Morvan *et al.* 1984), (Ge 1993), summarized in Table B.1. Following equation B.3, with the excitation rates given in this table, the effective band excitation rate is $g_e = 4.1 \times 10^{-4}$. With an Einstein A-coefficient of $A_{10} = 2.4 \times 10^{-5}$, the ratio $\log(g_e/A_{10}) = 1.23$. From table A1 of (Bockelée-Morvan & Crovisier 1985), we determine that approximately 43% of the HCN is in the J=1 state at 1 AU for that part of the coma in fluorescence equilibrium.

Table B.2. IR line parameters and excitation rates of HCO^+

ν_1 cm^{-1}	ν_2 cm^{-1}	ν_3 cm^{-1}	S_1 $\frac{km}{mol}$	S_2 $\frac{km}{mol}$	S_3 $\frac{km}{mol}$	A_1 s^{-1}	A_2 s^{-1}	A_3 s^{-1}	g_1 10^{-3}	g_2 10^{-5}	g_3 10^{-4}
[1]3124	887	2204	185	27	224	226	2.66	136	1.03	5.79	10.0
[1]3124	887	2204	208	48	228	254	4.72	138	1.16	10.3	10.2
[2]3231	845	2216	227	34	79	296	3.03	48.5	1.29	6.98	3.54
[3]3089	[4]830	[5]2184	244	30	80	291	2.58	47.7	1.35	6.06	3.55
[6]3089	830	2184	227	34	79	[7]272	2.99	47.4	1.26	7.02	3.53

[1] Frequencies and strengths computed in (Rogers & Hillman 1977)

[2] Frequencies and strengths computed in (Martin, Taylor, & Lee 1993)

[3] Experimental frequency (Amano 1983)

[4] Experimental frequency (Davies & Rothwell 1984)

[5] Experimental frequency (Foster, McKellar, & Sears 1984)

[6] Einstein coefficients from (Mauclaire *et al.* 1995)

[7] Strengths from (Martin, Taylor, & Lee 1993)

B.2.2 HCO^+ Fundamental Vibrational Bands

The frequencies of the fundamental vibrations of HCO^+ have been determined by both theory and experiment. Some frequencies, line strengths and A-coefficients from the literature are given in Table B.2, along with the excitation rates computed using equation B.1. We adopt the experimental fundamental frequencies of the three normal modes, as compiled by (Mauclaire *et al.* 1995): ν_1 = 3088.7 cm^{-1}, ν_2 = 829.7 cm^{-1}, ν_3 = 2183.95 cm^{-1}. The Einstein coefficients (computed using equations B.1 and B.2 with strengths from (Martin, Taylor, & Lee 1993)) of the first excited level of the three normal modes are taken to be A_1 = 272 s^{-1} A_2 = 2.99 s^{-1}, and A_3 = 47.4 s^{-1} (Mauclaire *et al.* 1995).

The excitation of the ν_1 and ν_3 modes dominate, and we compute a value of g_e = 1.7 $\times 10^{-3}$. Using a value of $A_{10} = 4.2 \times 10^{-5}$, the ratio $\log(g_e/A_{10}) = 1.61$. From table A1 of (Bockelée-Morvan & Crovisier 1985), we determine that approximately 27% of the radiatively excited HCO^+ is in the J=1 state at 1 AU.

B.3 Collisional excitation

Collisional excitation of cometary molecules depends on two parameters: the temperature in the coma and the collisional cross-sections between coma constituents. Of these, the temperature is reasonably well-understood (Crovisier 1987b), while the relevant collisional cross-sections between molecules in cometary comae are largely unknown. We employ a constant temperature to characterize the coma at our observation scale, and adopt what we consider to be conservative cross-sections, as discussed below.

Measurements of coma temperatures were made by *in situ* experiments aboard spacecraft missions to comet Halley (Lammerzahl *et al.* 1987). Bulk gas temperatures can also be estimated via radio astronomical observations of multiple rotational transitions of molecules (Bockelée-Morvan *et al.* 1994). Otherwise, estimates of the temperature of coma gas depend on thermodynamical models (Marconi & Mendis 1984; Marconi & Mendis 1986; Crovisier 1987a; Crovisier 1987b; Crovisier 1989). In general, such models include a near-nucleus temperature of $\approx$ 200 K, a decrease in temperature due to adiabatic expansion of the gas, a subsequent increase due to photolytic heating, and then a steady-state temperature. As shown in (Crovisier 1987a), this temperature profile varies with production rate as well as with heliocentric distance: as the latter decreases, the constant outer coma temperature increases. However, in all cases, the largest temperature variations occur within a 1000 km radius of the nucleus, well below the scale resolved by our telescope beam for either comet in the current study. Thus, we adopt a temperature value which is constant throughout the coma, but varies with the heliocentric distance of the comet. This variation has been observed for comet Hale-Bopp by Biver *et al.*(1998), who measured the rotational temperatures of transitions of CO and CH_3OH which closely approximate the kinetic temperature in the inner coma. Those authors report a power-law fit of

$T = 116\ r_h^{-1.24}$ pre-perihelion, $T = 93\ r_h^{-0.83}$ post-perihelion, and an average over all data of

$$T = 103\ r_h^{-1.10}. \tag{B.5}$$

The same technique was applied to comet Hyakutake by Lis *et al.* (1997) during the period March 20–30, 1996, yielding a temperature of 75 K. These temperatures are applied to compute the mean velocity of collisions between molecules.

In a comet at 1 AU heliocentric distance, H_2O is by far the most abundant molecular constituent of the coma. The collision rate can be expressed in terms of the collisional cross-section σ_c and the mean velocity V between the molecules:

$$C = \sigma_c n_{H_2O} V, \tag{B.6}$$

with

$$n_{H_2O} = \frac{Q_{H_2O}}{4\pi r^2 V_{exp}}. \tag{B.7}$$

Assuming H_2O is the primary collisional partner for an observed molecule X, the mean velocity between molecules at temperature T can be expressed as

$$V = \left(\frac{8kT}{\pi}\left(\frac{1}{m_{H_2O}} + \frac{1}{m_X}\right)\right)^{1/2}, \tag{B.8}$$

with $m_{H_2O} = 18$. $m_X = 27$ for HCN and 29 for HCO^+. Here Q_{H_2O} (molecules s^{-1}) is the H_2O gas production rate in (taken to be 10^{31} for comet Hale-Bopp at 1 AU, and 2×10^{29} for comet Hyakutake), r is the distance from the nucleus, and V_{exp} is the expansion velocity of the H_2O molecules.

The expansion velocity V_{exp} is known to vary with heliocentric distance (Delsemme 1982; Bockelée-Morvan, Crovisier, & Gérard 1990). Biver *et al.* (1998) analyzed spectral line shapes in comet Hale-Bopp in order to derive fits for the outflow velocity in pre- and post-perihelion observations, yielding fits of

$V_{exp} = 1.180\ r_h^{-0.44}$ pre-perihelion, $V_{exp} = 1.070\ r_h^{-0.37}$ post-perihelion, with an average over all data yielding

$$V_{exp} = 1.116\ r_h^{-0.40}. \tag{B.9}$$

In addition to this variation with r_h, the outflow velocity varies with distance from the nucleus. Presumably, the power law reported in equation B.9 applies to the near-nucleus outflow velocity. (Combi 1989) and (Xie & Mumma 1996) have modeled the velocity as a function of radial distance from the nucleus for comet Halley. These results suggest that the velocity remains less than 1 km s^{-1} within 10^4 km of the nucleus, and then increases approximately linearly to 1.4 km s^{-1} at 10^5 km. (Lammerzahl *et al.* 1987) report the results from the Giotto NMS, also in the coma of comet Halley, which measured velocities of 0.8 km s^{-1} out to $r = 4 \times 10^3$ km, increasing to 1.1 km s^{-1} at $r = 3 \times 10^4$ km from the nucleus. We adopt a constant outflow velocity for both comet Hale-Bopp and comet Hyakutake equal to that fit by (Biver *et al.* 1998) (equation B.9), acknowledging that this may underestimate the outflow velocity near the edges of our larger maps.

The gas production rate Q_{H_2O} varies with heliocentric distance as well. Nominally, this value is expected to depend upon the inverse-square of r_h. (Biver *et al.* 1998) and other observers of comet Hale-Bopp reported a "perihelion surge" where the production rates of many molecules increased more steeply than r_h^{-2}. However, for long-term observations of comet Hale-Bopp, we adopt the power law of Biver *et al.*(1997): $Q_{H_2O} \propto r_h^{-1.6}$. For comet Hyakutake, we adopt the power-law derived by Hicks & Fink (1997): $Q_{H_2O} \propto r_h^{-1.5}$.

B.3.1 neutral-neutral collisions

The collisional cross-section for HCN-H_2O collisions is unknown. Following Bockelée-Morvan *et al.*(1984), we adopt the value of $\sigma_c = 5 \times 10^{-15}$ cm^{-1}. This

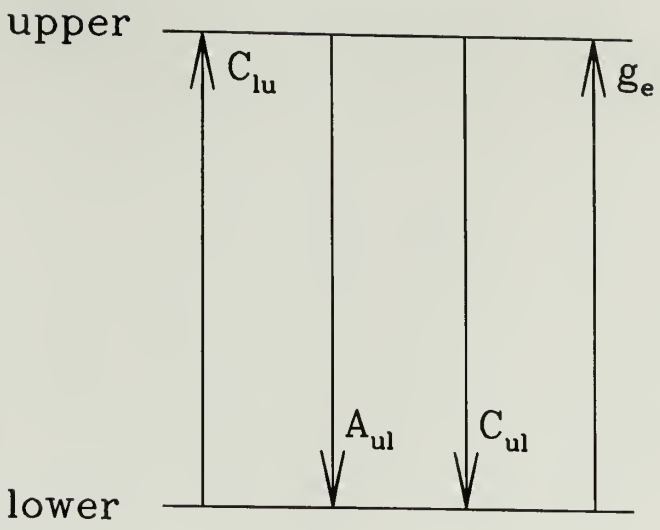

Figure B.1. The two-level approximation for excitation of the J=0 and J=1 states of HCO^+. The collisional excitation (C_{01}) and radiative excitation (g_e) rates are balanced by spontaneous emission (described by the Einstein coefficient A_{10}), and collisional de-excitation (C_{10}).

value lies between the geometric cross-section of $\sim 10^{-15}$ cm^{-1} and the HCN-HCN cross-section of 6×10^{-14} (Turfa *et al.*, 1977).

B.3.2 ion-neutral collisions

Cross-sections for H_2O–molecule collisions are largely unknown. The H_2O–H_2O cross section (Bockelée-Morvan 1987) itself is the subject of some debate, but we follow (Xie & Mumma 1992) in adopting $\sigma_c = 5 \times 10^{-14}$. The H_2O–HCO^+ cross-section should be large, owing to the fact that both molecules have large permanent dipole moments, even before the charge of HCO^+ is considered. Calculations performed by (Xie & Mumma 1992) suggest that ion-water cross sections are at least 10^{-12} cm^{-1}, and we adopt this value as a conservative estimate for H_2O–HCO^+ collisions.

B.3.3 neutral-electron collisions

Collisions with electrons are expected to dominate over collisions with H_2O in the portions of the coma where the ratio of their collisional cross-sections is greater than the inverse ratio of their densities:

$$\frac{\sigma_{e^- - \text{neutral}}}{\sigma_{H_2O - \text{neutral}}} > \frac{n_{H_2O}}{n_e} \tag{B.10}$$

For example, if the density of H_2O exceeds that of e by a factor of 1000, the cross section for e-neutral collisions must exceed that of H_2O -neutral collisions by greater than 1000. Xie & Mumma (1992) estimate that e-H_2O collisions will dominate over H_2O -H_2O collisions in the excitation of the $0_{00} \rightarrow 1_{11}$ rotational transition at distances exceeding 3000 km from the nucleus in comet Halley. Thus, electron collisions play an important role in the intermediate coma, although radiative excitation still dominates in the outer coma. The portion of the coma over which electron collisions are significant depends on the cometary activity level.

In our model, we allow for two regions: a collision-dominated region and a radiation-dominated region. The effect, if any, of electron collisions would be to increase the distance at which the transition between these two mechanisms occurs (Xie & Mumma, 1992). Mathematically, this is equivalent to a larger cross-section for collisions with H_2O, since the collision rate is proportional to the cross-section (equation B.6). As this cross-section is an estimated quantity, we investigate a range of cross-sections, from the value of 5×10^{-15} (Bockelée-Morvan *et al.*, 1984), up to 5×10^{-14}.

B.3.4 ion-electron collisions

Cross-sections for collisions between electrons and H_2O depend strongly on the energy of the electrons (Xie & Mumma 1992, and references therein), with larger cross-sections for lower-energy electrons. A typical cross section for e-H_2O

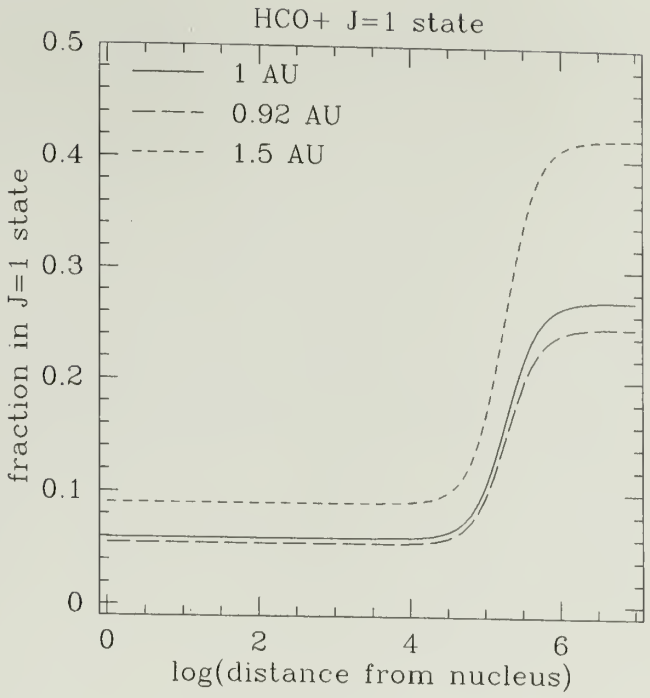

Figure B.2. The fraction of the total HCO^+ population which is in the J=1 state, versus distance from the nucleus in comet Hale-Bopp. Note that the transition from collisional to radiative excitation occurs around 10^5 km from the nucleus.

collisions is of the order 10^{-13} for an impact energy of 0.02 eV (230 K). The e–HCO^+ cross section will be even larger than this estimate due to the additional attraction of the electron to the ion. Thus, e–HCO^+ interactions might be important to consider in the coma of comet Hale-Bopp, where there is sufficient electron density to induce collisions. In the inner coma, the electron density ($n_e \sim 10^4$ cm^{-1}) is not sufficiently high with respect to the water density ($n_{H_2O} > 10^{10}$) to have an appreciable effect. Outside the contact surface, in the region where the electron temperature T_e increases rapidly, the number density of electrons also increases. However, cross-sections for collisions at these higher temperatures (10^4 K, 0.9 eV) are much lower: $\sigma_c < 10^{-14}$ cm^{-1} ((Xie & Mumma 1992) and references therein). Thus, we neglect the contribution of e–HCO^+ collisions in the excitation of HCO^+.

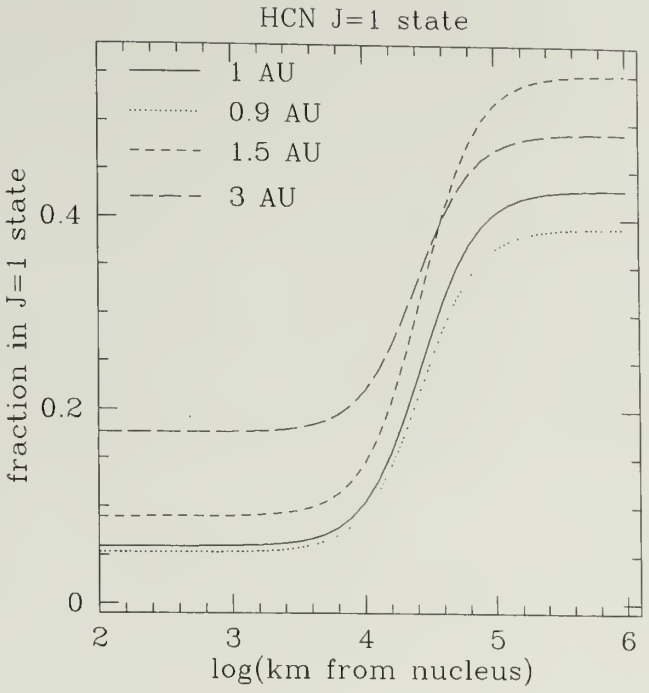

Figure B.3. The fraction of the total HCN population which is in the J=1 state, versus distance from the nucleus in comet Hale-Bopp. The assumed value of $\sigma_c = 5 \times 10^{-15}$, and the transition from collisional to radiative excitation occurs around 3×10^4 km from the nucleus.

B.4 Total excitation

With the dominant excitation mechanisms addressed, these two pieces must be assembled into a coherent picture of the total excitation throughout the coma. Collisions dominate in the dense inner coma, and radiative excitation dominates in the rare outer coma, but the location of the transition region varies for each molecule and for each comet. For analysis of the data, the quantity of interest is the population f_u of molecules in the upper state of the observed transition, and the cometocentric distance at which excitation by collisions ceases to dominate this population. In order to determine the approximate transition distance $r_{\rm tran}$, we adopt a two-level approximation for the population, as illustrated in Figure B.1. In this simple view, the collisional and radiative excitation and de-excitation

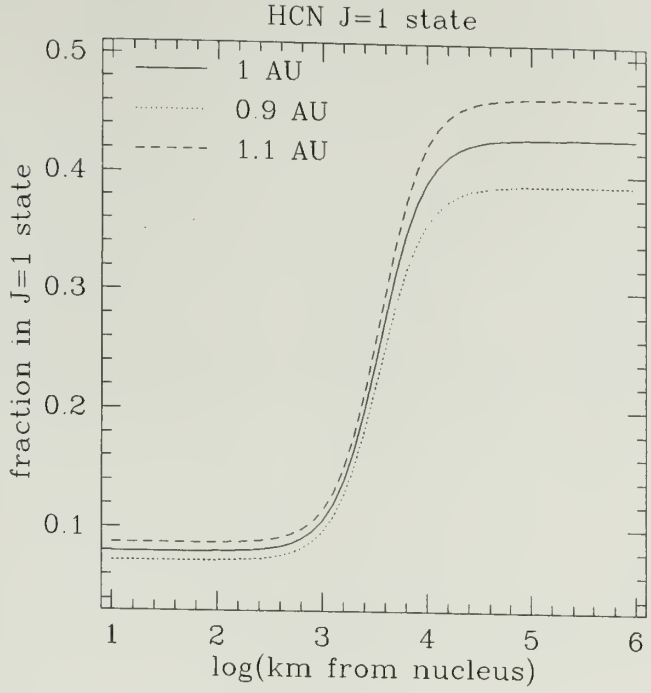

Figure B.4. The fraction of the total HCN population which is in the J=1 state, versus distance from the nucleus in comet Hyakutake. Here, the assumed value of $\sigma_c = 5 \times 10^{-15}$, and the transition from collisional to radiative excitation occurs around 3,500 km from the nucleus.

between the upper and lower states balance. The collisional excitation (after equation B.6) is expressed as C_{lu}, with the de-excitation $C_{ul} = C_{lu}\, e^{-E/k\mathrm{T}}$. Radiative excitation (after equation B.3) is g_e, with the Einstein spontaneous emission coefficient A_{ul}. Assuming that the two states are in equilibrium,

$$\frac{\mathrm{d}n_u}{\mathrm{d}t} = g_e n_l + C_{lu} n_l - \mathrm{A}_{ul} n_u - C_{ul} n_u = 0. \tag{B.11}$$

With the constraint that $n_l + n_u = 1$, we can express the number in the upper state as

$$n_u = \frac{g_e + C_{lu}}{\mathrm{A}_{ul} + C_{ul} + g_e + C_{lu}}. \tag{B.12}$$

In this equation, only the collision rates vary with cometocentric distance: for a given observation date, the radiative excitation rate is constant throughout the

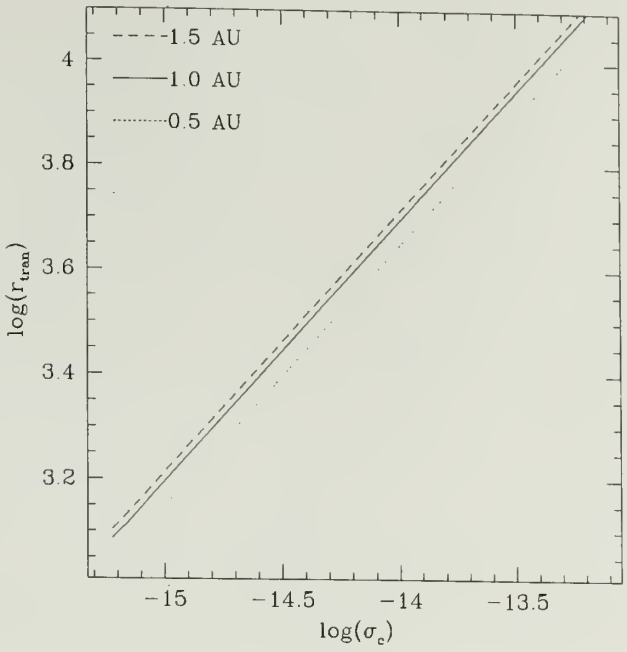

Figure B.5. The value of r_{tran} (in km) as it increases with σ_c for HCN in comet Hyakutake.

coma. When C_{lu} is large compared to g_e, the population is described by a Boltzmann distribution at temperature T (from section B.3). However, when C_{lu} is small compared to g_e, the population is as described in section B.2. Thus, we employ equation B.12 only to approximate the smooth transition from these two limiting values. Model curves are shown in Figures B.2, B.3, and B.4, for HCO^+ as well as HCN in both comets.

We define a transition distance (in cometocentric coordinates) of r_{tran}, at the point where the collisional excitation rate C and the radiative excitation rate g_e are equal. The upper-state population n_u is then parameterized in terms of the collision-dominated value n_{coll}, the radiation-dominated value n_{rad}, and this transition r_{tran}:

$$n_u = n_{\text{coll}} + \frac{(n_{\text{rad}} - n_{\text{coll}})}{1 + (\frac{r_{\text{tran}}}{R})^2}, \tag{B.13}$$

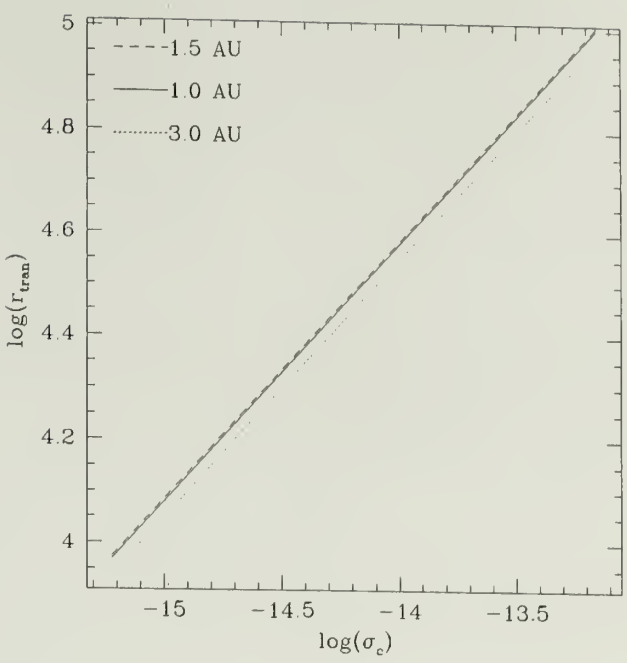

Figure B.6. The value of r_{tran} (in km) as it increases with σ_c for HCN in comet Hale-Bopp.

where R is the cometocentric distance. This transition distance is illustrated in Figures B.6 and B.5 for HCN, versus a range of collisional cross-sections.

References

Altwegg, K., *et al.* 1993, *Astron. Astrophys.*, 279, 260

Amano, T. 1983, *J. Chem. Phys.*, 79, 3595

Bergin, E. A., & Langer, W. D. 1997, *Astrophys. J.* , 486, 316

Biermann, L. 1951, *Zs. Ap.*, 29, 274

Biver, N., *et al.* 1997, *Science*, 275, 1915

Biver, N., *et al.* 1998, *Earth, Moon, and Planets*, in press

Bockelée-Morvan, D. 1987, *Astron. Astrophys.*, 181, 169

Bockelee-Morvan, D., Colom, P., Crovisier, J., Despois, D., & Paubert, G. 1991, *Nature*, 350, 318

Bockelée-Morvan, D., & Crovisier, J. 1985, *Astron. Astrophys.*, 151, 90

Bockelée-Morvan, D., Crovisier, J., Baudry, A., Despois, D., Perault, M., Irvine, W. M., Schloerb, F. P., & Swade, D. 1984, *Astron. Astrophys.*, 141, 411

Bockelée-Morvan, D., Crovisier, J., Colom, P., & Despois, D. 1994, *Astron. Astrophys.*, 287, 647

Bockelée-Morvan, D., Crovisier, J., & Gérard, E. 1990, *Astron. Astrophys.*, 238, 382

Combi, M. R. 1989, Icarus, 81, 41

Combi, M. R. 1996, Icarus, 123, 207

Cravens, T. E. 1991, in *Comets in the Post-Halley Era*, ed. e. Newburn, Vol. 2, 1211

Crovisier, J. 1987a, in *Cometary Radio Astronomy*, 45

Crovisier, J. 1987b, Astronomy and Astrophysics Supplement Series, 68, 223

Crovisier, J. 1989, *Astron. Astrophys.*, 213, 459

Crovisier, J. 1994a, in *Asteroids, Comets, Meteors 1993*, 313

Crovisier, J. 1994b, *J. Geophys. Res.*, 99, 3777

Crovisier, J. 1998, *Earth, Moon, and Planets*, in press

Crovisier, J., *et al.* 1990, *Astron. Astrophys.*, 234, 535

Crovisier, J., & Encrenaz, T. 1983, *Astron. Astrophys.*, 126, 170

Crovisier, J., & Schloerb, F. P. 1991, Comets in the Post-Halley Era, 1, 149

Davies, P., & Rothwell, W. 1984, *J. Chem. Phys*, 81, 5239

Delsemme, A. H. 1982, in *Comets*, 85

Despois, D. 1998, *Earth, Moon, and Planets*, in press

Eberhardt, P., & Krankowsky, D. 1995, *Astron. Astrophys.*, 295, 795

Erickson, N., Goldsmith, P., Novak, G., Grosslein, R., Viscuso, P., Erickson, R., & Predmore, C. 1992, *IEEE Trans. Microwave Theory Tech*, MTT-40, 1

Fernández, Y., *et al.* 1998, *Earth, Moon, and Planets*, in press

Fernández, Y. R., Kundu, A., Lisse, C. M., & A'Hearn, M. F. 1997, *Planet. Space Sci.*, 45, 735

Foster, S., McKellar, A., & Sears, T. 1984, *J. Chem. Phys*, 81, 578

Ge, W. 1993, Ph.D. thesis, Univ. Massachusetts, Amherst.

Gérard, E., Crovisier, J., Colom, P., Biver, N., Bockelée-Morvan, D., & Rauer, H. 1997, *Planet. Space Sci.*, in press

Gombosi, T. 1998, *Earth, Moon, and Planets*, in press

Greenberg, J. M. 1993, in The Chemistry of Life's Origins, 195

Greenberg, J. M., & Shalabiea, O. M. 1994, in Asteroids, Comets, and Meteors 1993, 327

Häberli, K., R.M. Altwegg, Balsiger, H., & Geiss, J. 1995, *Astron. Astrophys.*, 297, 881

Häberli, R. M., Combi, M. R., Gombosi, T. I., De Zeeuw, D. L., & Powell, K. G. 1997, Icarus, 130, 373

Harmon, J. K., *et al.* 1997, Science, 278, 1921

Harris, W. M., *et al.* 1996, IAUC, 6360, 1

Hicks, M. D., & Fink, U. 1997, *Icarus*, 127, 307

Huebner, W., Keady, J. J., & Lyon, S. 1992, *Astrophys. Space Sci.*, 195, 1

Huebner, W. F., Boice, D. C., Schmidt, H. U., & Wegmann, R. 1991, Comets in the Post-Halley Era. Vol. 2, 2, 907

Irvine, W., *et al.* 1984, Icarus, 60, 215

Irvine, W. M., Dickens, J. E., Lovell, A. J., Schloerb, F. P., Senay, M., Bergin, E. A., Jewitt, D., & Matthews, H. E. 1998, *Faraday Discuss.*, 109, 475

Jorda, L., Lecacheux, J., & Colas, F. 1996, IAUC, 6344

Lammerzahl, P., *et al.* 1987, *Astron. Astrophys.*, 187, 169

Lecacheux, J., Jorda, L., Enzian, A., Klinger, J., Colas, F., Frappa, E., & Laques, P. 1996, IAUC, 6354

Lis, D. C., *et al.* 1997, *Icarus*, 130, 355

Lis, D. C., *et al.* 1998, *Earth, Moon, and Planets*, in press

Lovell, A., Schloerb, P., Devries, C., Dickens, J., Irvine, W., & Senay, M. 1997, IAUC, 6590

Lovell, A. J., Schloerb, F. P., Bergin, E. A., Dickens, J. E., Devries, C. H., Senay, M. C., & Irvine, W. i. M. 1998a, *Earth, Moon, and Planets*, in press

Lovell, A. J., Schloerb, F. P., Dickens, J. E., Devries, C. H., Senay, M. C., & Irvine, W. i. M. 1998b, *Astrophys. J. Lett.*, 497, L117

Marconi, M. L., & Mendis, D. A. 1984, *Astrophys. J.* , 287, 445

Marconi, M. L., & Mendis, D. A. 1986, in *Asteroids, Comets, Meteors*, 369

Martin, J., Taylor, P. R., & Lee, T. J. 1993, *J. Chem. Phys*, 99, 286

Mauclaire, G., Lemaire, J., Heninger, M., Fenistein, S., Parent, D. C., & Marx, R. 1995, *Int. J. Mass Spec. Ion Proc*, 150, 487

Millar, R., Farquhar, P., & Willacy, K. 1997, *Astron. Astrophys. Suppl.*, 121, 139

Mumma, M. J., Weissman, P. R., & A., S. S. 1993, in *Protostars and Planets III*, 1177

Nakamura, T., Nakano, S., Hyakutake, Y., Kojima, T., Ikari, Y., & McNaught, R. H. 1996, IAUC, 6299, 1

Olofsson, H., Johansson, L. E. B., Hjalmarson, A., & Nguyen-Quang-Rieu, M. 1982, *Astron. Astrophys.*, 107, 128

Oort, J. H. 1950, *Bull. Astr. Inst. Neth.*, 11, 91

Predmore, C. R. 1995, in *Multi-Feed Systems for Radio Telescopes*, Vol. 75, 259, ed. Emerson and Payne

Pugh, L. A., & Rao, K. N. 1976, in *Molecular Spectroscopy: Modern Research, Volume II*, 165

Rogers, J. D., & Hillman, J. J. 1977, *J. Chem. Phys*, 77, 3615

Sarmecanic, J., Fomenkova, M., Jones, B., & Lavezzi, T. 1997, *Astrophys. J. Lett.*, 483, L69

Schleicher, D. G., Millis, R. L., Osip, D. J., & Lederer, S. M. 1998, *Icarus*, 131, 233

Schloerb, F., & Gérard, E. 1985, *Astron. J.* , 90, 1117

Schloerb, F. P. 1988, *Astrophys. J.* , 332, 524

Schloerb, F. P., & Ge, W. 1992, in Asteroids, Comets, Meteors, 533

Schmidt, H. U., Wegmann, R., Huebner, W. F., & Boice, D. C. 1988, *Comp. Phys. Comm.*, 49, 17

Tacconi-Garman, L. E. 1989, Ph.D. thesis, Univ. Massachusetts, Amherst.

Tozzi, G.-P., Lisi, F., Oliva, E., & Patriarchi, P. 1996, IAUC, 6357, 2

Veal, L., J.M. Snyder, *et al.* 1997, IAUC, 6575

Weaver, H. A., *et al.* 1997, *Science*, 275, 1900

Whipple, F. L. 1950, *Astrophys. J.* , 111, 375

Womack, M., Homich, A., Festou, M. C., Mangum, J., Uhl, W. T., & Stern, S. A. 1998, *Earth, Moon, and Planets*, in press

Womack, M., Stern, S. A., & Festou, M. C. 1997, *Planet. Space Sci.*, 45, 711

Xie, X., & Mumma, M. J. 1992, *Astrophys. J.* , 386, 720

Xie, X., & Mumma, M. J. 1996, *Astrophys. J.* , 464, 457